AFRICAN UNIVERSITY OF SCIENCE AND TECHNOLOGY
THEORETICAL PHYSICS STREAM

MODELLING OF CONTACT AND ADHESION AT INTERFACES IN BULK HETEROJUNCTION SOLAR CELLS

Edmond N. Y. DOUMON

A RESEARCH DISSERTATION PRESENTED TO THE DEPARTMENT OF PHYSICS, AFRICAN UNIVERSITY OF SCIENCE AND TECHNOLOGY (AUST), ABUJA, IN PARTIAL FULFILMENT OF THE REQUIREMENTS FOR THE AWARD OF A MASTER OF SCIENCE DEGREE IN THEORETICAL PHYSICS

Supervised by: Prof. Winston O. SOBOYEJO

December, 2011

DECLARATIONS

1. I hereby declare that except for the reference to the works of other researchers and to literature, which have been duly cited where appropriate, the data collection, its analysis and the entire research report were solely accomplished by me under the candid supervision of ***Prof. Winston O. Soboyejo*** of the Materials Science and Engineering Department – African University of Science and Technology (AUST).

   I am therefore wholly responsible for any flaws in the coming pages.

   Student:

   Name: **DOUMON, NUTIFAFA YAO**

   40184

   

   Date: 21 / 10 / 2011

2. The undersigned hereby declare that the work presented in this project was fully supervised in accordance with the guidelines of dissertation laid down by the University of Ghana.

   Supervisor:

   Name: **Prof. Winston O. Soboyejo**

   Date: / / 2011

DEDICATION

To

My sisters **Rejoyce** and **Modester** and brother **Marius Doumon**

I love you all

We shall surely sail through

And to all my **friends**

Contents in brief

Table of Contents

TABLE OF FIGURES

Figures ***Pages***

ACKNOWLEDGEMENTS

This final work is a cooperative effort of some individuals, each contributing in his or her small way. Their goal is to provide me with the appropriate and enjoyable learning materials and environment to be able to achieve what you are about to read.

My special gratitude goes to:

- ***Prof. Winston O. Soboyejo*** **of Princeton University (USA)/AUST (Abuja)** for his guidance and patience during the supervision of this research work
- ***Prof. Nima Rabhar*** **of University of Massachusetts-Darmouth (USA)** for taking time to listen to me and providing insight into this thesis
- ***Dr. Joseph Berry*** **of National Renewable Energy Laboratory (NREL-Colorado (Boulder), USA)** for his untimely assistance in providing papers and sharing thoughts with me
- ***Dr. François Tsobnang*** **of "Institut Supérieur Des Matériaux et Mécanique Avancés" (ISMANS-Le Mans, France)** for making himself available for me, and
- ***Madam Esther Hamilton and Rev. Fr. Ernest Dugah,*** May God bless you all

ABSTRACT

The study of the structures and properties of organic materials for organic photovoltaic (OPV) applications and their interrelationships is a rapidly growing field of research, involving interdisciplinary efforts at the frontiers of chemistry, solid state physics and materials science. These materials differ from the better-understood silicon solar cell based materials by the lack of long range three-dimensional translational periodicity in their atomic arrangements and also by their layered structures but are of important use in electronics, the medical fields, defense and aerospace etc… This study is concerned with bulk heterojunction (BHJ) solar cells, a class of organic photovoltaic (OPV) solar cells. We present a review of the state-of-the-art in the theoretical study of the structures of such solar cells. The topics covered include *theory of semiconductors*; the *physics of solar cells*; the *structure*, the *properties and the nature of the organic materials for use in solar cells* and the *modeling of effects of contacts and adhesion at the interfaces of the layers* of such devices. Our *results* showed that the presence of particles such as dust affect the performance of the devices. It creates voids at the interfaces of the device, resulting in reduction in contact length. It is also observed based on the modeling that the void's length increases with increasing Young's modulus of the layers while it decreases with increasing adhesion or increasing pressure due to lamination. This in turn, affects the contact length in the reverse way.

Chapter One:

Background and Introduction

1.1.The sun: Its availability

The sun according to the Penguin English Dictionary [1], is a star or celestial body that emits its own light. It forms part of the solar system. It is the star nearest to the Earth, round which the Earth and other planets revolve.

Located at the centre of the solar system, the sun is white in colour, although from the surface of the Earth it may appear yellow because of atmospheric scattering of blue light [2]. It has a spherical structure with a diameter of *1,392,000* km (*109* times that of the Earth). It has a mass of 2×10^3 kg (330,000 times that of the Earth), almost accounting for 99.86% of the total mass of the solar system. About three quarters (¾) of its mass is made up of Hydrogen (H) and the rest Helium (He).

The sun has a mean distance of 149.6×10^6 km from the Earth, and light travels from the sun to the Earth through this distance in about 8'19" giving us the celerity $c = 2.99 \times 10^8\ m.s^{-1}$. Despite all these realities, the availability of the sun to the Earth surface is not uniform. Depending on the particular location on Earth, one could experience the sun all season or partly or practically not all. The parts of the Earth lying in the tropics and the equatorial regions receive year long radiations from the sun.

1.2. Importance of the Sun

The sun emits its own light and keeps a surface temperature of 5,778 K. This energy is generated by a continuous nuclear fusion of Hydrogen (H) nuclei into Helium (He). This energy of sunlight supports almost all life on Earth, by photosynthesis. It drives the Earth's climate and weather. The amount of power that the sun deposits per unit area at a distance of one astronomical unit (AU), is known as its solar constant $s \cong 1{,}368\ W.m^{-2}$. After attenuation, close to $1{,}000\ W.m^{-2}$ is received in clear condition, when the sun is near the zenith. This energy can be harnessed by a variety of natural, synthetic and technological processes.

Solar energy has enormous potentialities for developing countries. It has a clean source of energy and it is inexhaustible. It is probably not surprising that nature has most of the developing countries (constituting over two thirds (2/3) of the world) fall within the tropical belt. This zone

receives on an average, 2 to 3 times the energy incident on regions outside it.

At the fourth (4^{th}) course on solar energy conversion [3], Prof. Williams of the Georgia Institute of Technology, who had done some preliminary studies on the feasibility of solar energy utilization in Tanzania identified the priority areas of application of solar energy in developing countries as: dependable source of pure water, lighting, food drying, heating/hot water in the case of northern climates, cooking, refrigeration, grinding and milling among others.

1.3. Energy situation in Africa

According to the Penguin English Dictionary [1], Energy is a fuel for other sources of power, especially electricity. The mixture of energy sources used by a country depends on its natural endowment of the different kinds of energy resources. Is this belief true with all countries?

While countries from the developed world have almost experienced most of their energy resources, countries in the developing world are yet to exploit most of their available energy resources. For example in the case of African countries, their potential to harness clean energy from solar, wind and hydro sources is far greater than their current needs. Nevertheless, electricity is still generated through thermal (58.8% of installed capacity) or hydroelectric (41.2%) resources [4]. Natural gas has the potential to make a more significant impact in the region's energy sector, as fields in Nigeria, Cote d'Ivoire and Senegal are developed. Due to the region's relatively small urban population (approximately 33.9%) and the limited infrastructure, access to commercial energy sources is limited. The energy challenges faced by Africa are illustrated by the following case studies:

1.3.1. Togolese experience

A small country of about 56,600 km^2, Togo, located in the southern part of West Africa, is wedged between Ghana to the west, Benin to the east, Burkina Faso to the north and the Atlantic Ocean in the south. It is located in the northern hemisphere between latitudes 6^o and 11^o north and longitudes 0^o and $1^o30'$ east. Hence, Togo has a tropical climate.

The eighteen years life experience there till 2003 is not the best to speak of in the field in energy. Recently the regional report from ***Wa*** stated that in Togo in 2006, up to 75% of the total

energy consumption was covered by biomass energy [4]. With no proven oil or natural gas reserves, Togo is forced to import all of its petroleum, which is the dominant fossil energy that is used in Togo. Electricity is generated mainly from hydro-power and petroleum. Combustibles like fuel-wood are used for residential energy consumption, which is the main cause of deforestation. Furthermore, Togo does not significantly utilize any type of new renewable energy source.

Hence, Togo depends on the hydroelectric power from the Akossombo dam in Ghana. It receives about four-fifths (4/5) of its electricity from Ghana. Apart from the transmission line inaugurated formally in July 1975, there is also a hydroelectric station at Kpime (Kpalime–Togo) and a 65 MW plant built on the Mono River near Atakpame. In 2001, Togo installed a 34,000 kW capacity with approximately 90% conventional thermal and 10% hydroelectric. Electrical output that year was 97 million kWh, of which 97.9% was from fossil fuels and 2.1% from hydro-power [4].

It is obvious the Togolese population is suffering greatly from energy crisis globally observed in Africa. Being dependent on another country in the same situation does not help at all. Furthermore, climate change and global warming further worsen the case, since rain fall is reduces with each passing year. There is, therefore, a need to explore the potential of solar energy to address the basic needs of Togolese people in rural/urban environments.

1.3.2. Ghanaian experience

From the previous section, it is clear that Ghana is also located in the tropics. At present, about two-thirds (2/3 = 233.1 PJ) of the total primary energy supply is from traditional fuels, specifically biomass. Burning of this biomass in traditional cook stoves also results in indoor or local air pollution that is damaging to the health of the users, who are mostly women [5].

The availability of modern energy in the country is very uneven. Rural areas in Ghana have especially poor access to commercial energy supplies. Less than 20% of the total rural population and only 5% in the rural population of the northern part of the country has access to electricity. Hence, access to electricity is a serious problem Ghana [5]. The reduction in hydro-availability created by a delayed and below average inflows into the Volta reservoir, has also been a problem to the Volta River Authority (VRA) and the Electricity Company of Ghana (ECG) [6].

There is therefore, a need to explore alternative energy sources in Ghana. These include nuclear, solar, hydro and wind energy [5]. However based on the recent experience in Fukishima Daiichi [7] and its implications on the world's view on nuclear energy it is not clear that Ghana will have the technical capability to safely manage nuclear energy by 2018, which is one of the goals of the Ghana Atomic Energy Commission (GAEC). However, there is sun all day in Ghana; measures can be taken to ensure that there is a strong long-term plan to produce electricity from environmentally friendly solar energy. This suggests a need for research and development of solar energy within an African context.

Name of Plant/sites	**River**	Capacity (MW)	**Generation (Gwh)***	Overnight investment cost (US /KW)	**Fixed O&M cost (US / KW-year)**	Levilized generation cost**
Bui	Black Volta	**200**	762	**1,660**	6.5	**41.5**
Hemang	Pra	**93**	237	**1,860**	11.5	**72.5**
Juale	Oti	**87**	237	**3,300**	12.0	**157.5**
Pwalugu	White Volta	**48**	61	**3,600**	16.0	**173.3**
Tanoso	Tano	**56**	N/A	**N/A**	N/A	
Micro-hydro				**1,500**	40.0	**38.7**

Table 1.1: *** Estimated annual firm generation** ****At 8% discount rate** **N/A: not available [6]**

1.3.3. Nigerian experience

With a country area of 923,768 km^2 and a population of over 150 million inhabitants, Nigeria is also located in the tropics in West Africa. It is the only significant oil producer in West Africa, and is a net energy exporting country (e.g. part of Benin republic depends on Nigeria). Nigeria's natural gas reserves are the 9th largest in the world, but due to a lack of infrastructure, Nigeria flares 75% of the natural gas that it produces.

Traditional biomass accounts for the largest share of the total energy consumption (51%) followed by petroleum products (41%), natural gas (5.2%) and electricity (3.1%) which is solely managed the Power Holding Company of Nigeria (PHCN), previously known as the National Electric Power Authority (NEPA). Total installed electricity capacity is estimated at 5.9 GW, with about 40% of the population having access to electricity (82% in urban areas and 10% in rural areas). According to the Nigerian Energy Policy report from 2003, it is estimated that the

population connected to the grid system is short of power supply over 60% of the time [8].

As in the case of Ghana, the potential solutions to the energy challenges in Nigeria include nuclear, solar, wind and hydro sources of energy. However, the limited capacity to manage nuclear energy is a major issue in Nigeria, just as it is in Ghana.

Furthermore, the ongoing research on alternative energy has not yet had a major impact on the lives of people in rural/urban Nigeria. This is due partly to the relatively high initial costs of solar energy, which still remains as a major barrier to the use of solar energy in Nigeria [8].

1.4. Problem definition

There is a need to develop affordable approaches to the harnessing of solar energy for the generation of electricity in rural/urban areas of Africa. This will be explored in this project using bulk heterojunction (BHJ) organic solar cells that have the potential to significantly reduce the cost of solar cells to levels that are affordable to people in rural/urban areas of Africa.

The potential of such systems has also been enhanced by the recent improvements in the efficiencies of BHJ solar cells to approximately 8% [9]. However, there are still some concerns about the long-term stability of the BHJ solar cells, especially in the presence of oxygen and water vapour in the atmosphere. There is also the potential to further improve the device efficiencies by promoting improved charge transport through increased adhesion and contact across the layers in BHJ solar cells.

1.5. Scope of work

The objective of this study is to explore the potential role of adhesion and contact in the design of interfaces that can promote improved charge transport across BHJ solar cells.

Pressure-assisted lamination will be explored as a method for improving the contacts between layers in BHJ solar cells. The contacts will be modeled by considering the deformation and adhesion around dust particles (or voids) that are present in the clean room environment. A lamination encapsulation technique will also be modelled to provide process design criteria for the fabrication of a poly-di-methyl-siloxane (PDMS) package that can limit the access of water

vapour and oxygen to BHJ solar cells. Initial efforts will be made to relate the contacts to the current-voltage behaviour and device lives.

This thesis is divided into chapters. Following the background and introduction in chapter one, the relevant literature on BHJ solar cells and device physics is reserved in chapter two. Models for the prediction of contact are then presented in chapter three. These include analytical and numerical models of contact between layers that are relevant to BHJ solar cells, and PDMS packages that can limit the access of water vapour and oxygen into the BHJ solar cells. The predictions from the models are correlated with previously reported experimental results in chapter four before presenting the salient conclusions from this work in chapter five, followed finally by suggestions for future work.

Chapter Two:

Literature review

2.1. What is a solar cell?

A solar cell is a solid state device that converts the energy of the sunlight directly into electricity by the photovoltaic effect. The photovoltaic effect is the creation of a voltage (corresponding electric current) in a material upon exposure to light. The generated electrons are transferred between different bands within the material, resulting in a build-up of a voltage between two electrodes.

The history of solar cells begun in the 19th century when it was observed that, the presence of sunlight is capable of generating usable electrical energy. Its development evolves from the work of the French physicist *Alexandre-Edmond Becquerel* with his father *Antoine-Cesar Becquerel* in 1839. The *Becquerels'* discovered the photovoltaic effect while experimenting with a solid electrode in an electrolyte solution. They observed that voltage developed when light fell upon the electrodes. About fifty (50) years later, the American inventor *Charles Fritts* constructed the first ever solar cells using junctions, formed by coating the semiconductor Selenium (Se) with an ultra-thin, nearly transparent layer of Gold (Au). These had a conversion efficiency of only about 1%. From 1888 to 1891, the Russian physicist *Aleksandr Grigorievich Stoletov* worked a lot on photoelectric effect. One of these is the building of the first solar cell based on the outer photoelectric effect and estimated the response time of the photoelectric current.

Solar cells are made from semiconductors, and have much in common with other solid-state devices, such as diodes, transistors and integrated circuits. They represent the fundamental power source (conversion unit) of PV system. The range of solar cells covers different materials and different structures in the quest to extract maximum power from the device while keeping the cost to a minimum [10].

2.2. Types of solar cells

Over the years, different materials have been used for the manufacture of solar cells. Different materials display different efficiencies and also have different costs. But materials for efficient solar cells must possess characteristics in conformity with the spectrum of the available light. In our case the sunlight is our source of energy.

Currently available solar cells are made from bulk materials that are cut into wafers between 180 to 240 microns thick and are then processed like other semiconductors. Based on the various materials, solar cells can be divided into three (3) groups: ***crystalline*** *solar cells,* ***amorphous*** *solar cells* and ***organic/polymer*** *solar cells.*

2.2.1. Crystalline solar cells

This class of solar cells is by far the most wide spread and efficient as at now. The main material used is Silicon (Si); and the most prevalent material for solar cells is crystalline Silicon (***c-Si***). This class is also subdivided into two groups:

- **Monocrystalline solar cells:**

They are made up of a single-crystal wafer. The orientations of the unit cells are the same throughout the crystal. Monocrystalline Silicon is often made using the *Czochraslski* crystal growth process. Fabricated using cells saw-cut from large single cylindrical crystal of Silicon; they are the most efficient of the photovoltaic (PV) technologies. The principal advantage of monocrystalline cells are their efficiencies, typically around 15%, although the manufacturing process required to produce mono-crystalline Silicon cell is complicated, resulting in slightly higher costs than other technologies. In appearance they have smooth texture but they are rigid. Recently "*Sunpower Si solar cell"* produced cells with 21.5% efficiency [10].

- **Polycrystalline solar cells:**

They are made from cells cut from an ingot of melted and recrystallized Silicon. In the manufacturing process, molten Silicon is cast into ingots of polycrystalline Silicon; these ingots are then saw-cut into very thin wafers and assembled into complete cells. Multicrystalline cells are cheaper to produce than monocrystalline ones, due to the simpler manufacturing process. However they tend to be slightly less efficient, with average efficiencies of around 12%. They have a speckled crystal reflective appearance and again need to be mounted in a rigid frame.

2.2.2. Thin-film solar cells

A thin-film solar cell (TFSC) also called a thin-film PV (TFPV) is made by depositing one or more thin layers (thin films) of PV material on a substrate (coated glass or stainless steel sheet...). The selected materials are all strong light absorbers and only need to be about 1 micron thick, so materials costs are significantly reduced [11]. The most common materials are:

- Amorphous Silicon (a-Si) or other thin-film Silicon
- Polycrystalline materials: - Cadmium Telluride (CdTe) -
  - Copper Indium (Gallium) Selenide (CIS or CIGS) -

The semiconductor junctions are formed in different ways, either as a ***p-i-n*** device in amorphous Silicon, or as a ***heterojunction*** (e.g. with thin Cadmium Sulphide layer) for CdTe and CIS. A transparent conducting oxide layer (such as Tin oxide) forms the front electrical contact of the cell, and a metal layer form the rear contact.

The amorphous Silicon (a-Si or a-Si:H) is the most widely developed of the Silicon thin-film technologies. Others are polycrystalline, monocrystalline (nc-Si or nc-Si:H) or black Silicon. It is to be noted that thin-film Silicon is opposed to wafer (or bulk) Silicon (monocrystalline or polycrystalline). Deposition techniques used are the chemical vapour deposition (CVD), sputtering and hot wire technologies.

2.2.3. New class of cells: Organic or Plastic solar cells

Photovoltaic (PV) devices are based on the concept of charge separation at an interface of two materials, which can be *n*-type and *p*-type semiconductors, heterojunctions between different semiconductors or semiconductor-metal junctions.

As stated earlier, most solar cells presently sold are based on Silicon wafers, the so-called ***"First generation"*** technology. The use of organic bilayers with photo-induced electron transfer is a subject of intensive research in the last decades [11]. In these bilayer donor-acceptor systems, the energy conversion is limited by the fact that charge separation only takes place very close (10–20 nm) of the interface as a result of the limited exciton diffusion and/or space-charge region. As a result, charge carriers generated far from the interface recombine before they reach the interface. Furthermore, since the charge separation is limited to a small region the PV efficiency

is limited by the amount of photons absorbed in this region.

An increase of the efficiency has recently been realized by mixing electron-donor type polymers with suitable electron acceptors. Progress has especially been made using conjugated polymer/fullerene solid composites. For these materials systems, the efficiency of the charge separation process is nearly 100% as a result of the fast electron transfer from the polymer towards the fullerene (< 100 fs). By mixing the two components to a single composite active layer, a "***bulk heterojunction***" is formed between the electron donors and acceptors. Through control of the morphology of phase separation into an interpenetrating network a high interfacial area is achieved within a bulk material. If the donor-acceptor networks are bicontinuous also, the collection efficiency can be optimized. In present devices, based on various polyphenylene vinylene derivatives, the limited power conversion efficiency of about 8.1 % is mainly due to the spectral mismatch of the absorbing polymer to the solar spectrum.

2.3. Why Bulk Heterojunction Solar Cells?

Bulk Heterojunction (BHJ) Solar Cells have attracted considerable attention over the past years due to their potential as a low cost PV technology [12]. The possibility of manufacturing modules via a standard printing/coating process in a roll-to-roll (R2R) fashion (Figure 2.1) in combination with the use of low cost materials will lead to a Watt-peak price of less than 1 US$ within the next few years [12].

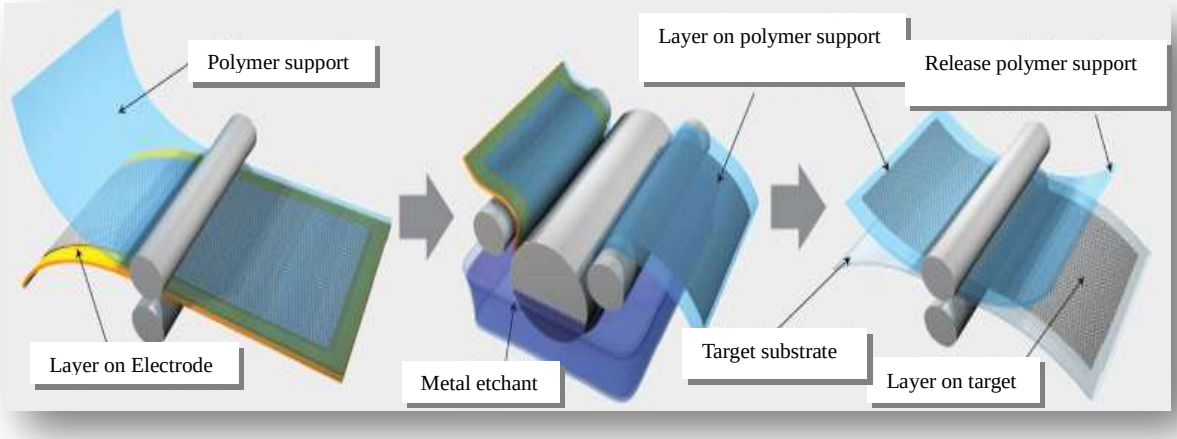

Figure 2.1: Roll to roll process

Despite the low cost potential, the power conversion efficiency of BHJ solar cell devices is low compared to inorganic solar cells. Efficiencies in the range of 7 to 8% have been certified at the *Advanced Industrial Science and Technology* (AIST) and the *National Renewable Energy Laboratory* (NREL) usually on devices with very small active area [13].

The current understanding of BHSC suggests that the maximum efficiency is in the range of 10–12 % [14]. Several reasons for the power conversion efficiency limitations have been identified [12]. Some of the prerequisites for achieving highest efficiencies are donor and acceptor materials with optimized energy levels (Highest Occupied Molecular Orbital – HOMO – and Lowest Unoccupied Molecular Orbital – LUMO –), efficient charge transport in the donor-acceptor blend, efficient charge generation and limited recombination losses. Power conversion efficiency is strongly dependent on charge generation and transport that is dominated by the phase behaviour of the donor and acceptor molecules. Often an unfavourable nanomorphology of this two component blend limits the power conversion efficiency of the BHJ solar cells. Precise control of the nanomorphology is very difficult and has been achieved only for a few systems [14]. The relation between the chemical structure of the donor and acceptor materials, the charge transport and the nanomorphology that they form when they are blended is not well understood. In this work we discuss the adhesion effect, the contact length between layers, the current status and the future potential of BHSC.

2.4. Solar energy technology

Current solar power technology has little chance to compete with fossil fuels or large electric grids. Today's solar cells are simply not efficient enough and are currently too expensive to manufacture for large-scale electricity generation. However, potential advancements in nanotechnology may open the door to the production of cheaper and slightly more efficient solar cells.

First, the current solar cell technologies are examined along with their drawbacks. The research on nano solar cells will then be explored with the science behind them. Finally, the implications of these technologies would be considered for

potential applications in rural/urban contexts.

Before introducing new solar products which use nanotechnology, it is necessary to explain the basic process that a normal solar cell uses. Conventional solar cells are called PV cells. These cells are made out of semiconducting material, usually Silicon. When light hits the cells, they absorb energy through photons. This absorbed energy knocks out electrons in the Silicon, allowing them to flow. By adding different impurities to the silicon such as phosphorus or boron, an electric field can be established. This system acts as a diode, because it only allows electrons to flow in one direction [15].

Consequently, the end result is a current of electrons, better known to us as electricity. Conventional solar cells have two main drawbacks: they can only achieve efficiencies around ten percent (10%) and they are expensive to manufacture. The first drawback, inefficiency, is almost unavoidable with silicon cells. This is because the incoming photons, or light, must have the right energy, called the bandgap energy, to knock out an electron. If the photon has less energy than the bandgap energy then it will pass through. If it has more energy than the band gap, then that extra energy will be wasted as heat. *Scott Aldous*, an engineer for the *North Carolina Solar Center* explains that, "These two effects alone account for the loss of around 70 percent of the radiation energy incident on the cell" [15]. Consequently, according to the *Lawrence Berkeley National Laboratory*, the maximum efficiency achieved today is only around 25 percent [16]. Mass-produced solar cells are much less efficient than this, and usually achieve only ten percent efficiency.

2.4.1. Solar energy and Nanotechnology

Nanotechnology might be able to increase the efficiency of solar cells, but the most promising application of nanotechnology is the reduction of manufacturing cost. Chemists at the *University of California (UC), Berkeley*, have discovered a way to make cheap plastic solar cells that could be painted on almost any surface. These new plastic solar cells achieve efficiencies of only 1.7%; however, *Paul Alivisatos*, a professor of chemistry at *UC Berkeley states*, "This technology has the potential to do a lot better. There is a pretty clear path for us to take to make this perform much

better" [17].

These new plastic solar cells utilize tiny nanorods dispersed (figure 2.2 below) **[14]** within in a polymer. The nanorods behave as wires because when they absorb light of a specific wavelength they generate electrons. These electrons flow through the nanorods until they reach the aluminium electrode where they are combined to form a current and are used as electricity. This type of cell is cheaper to manufacture than conventional ones for two main reasons. First, the manufacturing of these cells does not require expensive equipment such as clean rooms or vacuum chambers unlike conventional silicon based solar cells. Instead, these plastic cells can be manufactured in a beaker. *UC Berkeley* graduate student *Wendy Huynh* says, "We use a much dirtier process, and that makes it cheap" [17].

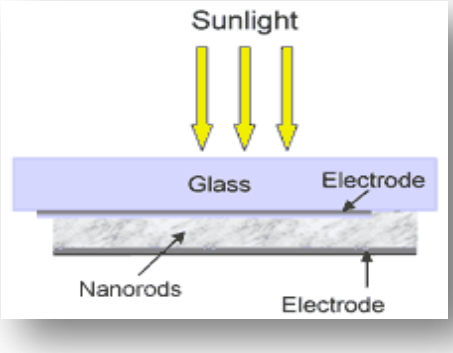

Figure 2.2: Diagram of a nano solar cell [17]

Another potential feature of these solar cells is that the nanorods could be 'tuned' to absorb various wavelengths of light. This could significantly increase the efficiency of the solar cell because more of the incident light could be utilized. According to a 2001 report, "*The Societal Implications of Nanoscience and Nanotechnology*", by the National Science Foundation, if the efficiency of PV cells was improved by a factor of two using nanotechnology, then the role of solar energy would grow substantially [18]. In addition to the *UC, Berkeley,* a well-known company named *Konarka Technologies* is also pursuing the use of nanotechnology to improve solar energy. In fact, they are already manufacturing a product called, "Power Plastic" which absorbs both sunlight and indoor light and converts it into electricity. For patent reasons, their technology is kept secret, but the basic concept is

that Power Plastic is made using nanoscale titanium dioxide particles coated in PV dyes, which generate electricity when they absorb light. According to Engineer Magazine, *Konarka* has already, "built fully functional solar cells that have achieved efficiencies of around 8%" [19]. Future designs are already underway, which includes tuning the nanorods to absorb certain wavelengths of light in order to exploit a greater range of the colour spectrum. Improvements, such as this, could make it possible to manufacture inexpensive solar cells with the same efficiency as current technology. Since the manufacturing cost of conventional solar cells is one of the biggest drawbacks, this new technology could have some impressive effects on our daily lives. Although this new technology is only capable of supplying low power devices with sufficient energy, its implications on society would still be tremendous. It would help preserve the environment, decrease soldiers carrying loads, provide electricity for rural areas, and have a wide array of commercial applications due to its wireless capabilities.

2.4.2. Applications

Inexpensive solar cells, which would utilize nanotechnology, would help preserve the environment. According to Engineer Magazine, *Konarka* Technologies is already proposing, "coating existing roofing materials with its plastic photovoltaic cells" [19]. If it were inexpensive enough to cover a home's entire roof with solar cells, then enough energy could be captured to power almost the entire house. If many houses did this then our dependence on the electric grid (fossil fuels) would decrease and help reduce pollution. Some people have even proposed covering cars with solar cells or making solar cell windows. Even though their efficiency is not very great, if solar cells were inexpensive, then enough of them could be used to generate sufficient electricity.

New technology in solar cells would also have military implications. The U.S. Army has already hired Konarka Technologies to help design a better way to power their soldiers' electrical devices. According to *Daniel McGahn*, *Konarka*'s executive vice president, "A regular field soldier carries 1.5 pounds of batteries now. A special operations soldier has a longer time out, has to carry 140 pounds of equipment, 60 to

70 pounds of which are batteries [20].” If nanotechnology could be used to create inexpensive and reasonably efficient solar cells, it would greatly improve the mobility of soldiers.

Inexpensive solar cells would also help provide electricity for rural areas and third world countries. Since the electricity demand in these areas is not high, and the areas are so distantly spaced out, it is not practical to connect them to an electrical grid. However, this is an ideal situation for solar energy. If it were inexpensive enough, it could be used for lighting, hot water, and even medical devices [20]. It would greatly improve the standard of living for millions, possibly even billions of people.

Finally, inexpensive solar cells could also revolutionize the electronics industry. Solar cells could be embedded into clothing and be programmed to work for both indoor light and sunlight. In fact, *Konarka Technologies* has already begun developing a photovoltaic fabric that could be woven into clothing **[16]**. For the first time, our electronics would be truly wireless and we would not have to plug them into an outlet at night to recharge them. Consequently, even though conventional solar cells are expensive and cannot yet achieve high efficiency, it may be possible to lower the manufacturing costs using nanotechnology. Institutions such as the *UC, Berkeley* and *Konarka Technologies* are actively pursuing ways to make this happen. Although solar cells are not efficient enough to replace large-scale electric grids, there are many opportunities for them to be used for low power devices. The effects that a low cost, reasonably efficient (low power) solar cell would have on society are tremendous. It would help preserve the environment, protect soldiers, provide rural areas with electricity, and transform the electronics industry. These dramatic effects, which would all be a result of nanotechnology, would greatly change and even improve society.

2.5. Concepts surrounding solar cells

2.5.1. Electrical conductivity: Materials classification

Based on the concept of electrical conductivity materials are classified into three main groups: *insulators*, *semiconductors* and *conductors* (Semi-metals and

metals).

An *insulator* is a material which contains no charge carriers free to move within its volume. Electrical insulators cannot carry electric current. So we use them to protect ourselves. This can be well explained with the idea of bandgap. In an insulating material the bandgap energy is very large compared with the typical thermal energy available per particle. As a result, none of the electrons in the valence band can get enough energy to reach the conduction band [21]. The valence band of an insulator is completely full. The conduction band is completely empty. So even if an electric field is applied, there are no electrons to move and so no conduction can take place; the valence electrons cannot move because the valance band is packed tight, so the insulator refuses to let any electrons move when we apply an electric field. The result is that there is no current. Thus, large band gap makes it difficult to excite electrons into conduction band.

An example of a *conductor* is a metal. A metal is a substance which, in the solid state, consists of a latticework of positive ions held in a stable condition by free electrons [21]. Metals which are considered to be good conductors of electricity are formed by the mutual bonding of the parent atoms into a regular, geometrical array or lattice by forces acting at the microscopic atomic scale. The bonding process is such that the outer or valence electrons from each parent atom are released and are free to move throughout the solid, in response to electric fields. In a metallic material, a conductor, the conduction band and the valence band overlap.

The most common *semiconductor* materials for electronic devices are germanium and silicon. In their intrinsic state at normal room temperature (300K), the number of free electrons and holes are 10^{13} carriers per cubic centimetre in germanium and 10^{10} in silicon [21]. Since the number of atoms per cubic centimetre is still about 10^{23}, the number of charge carriers is only a tiny fraction of the number that would be present if these materials behave like a metal. Due to their much smaller number of available charge carriers; their conduction properties are much poorer than those of metals. They do, however, conduct sufficient current, so that they cannot be classified as insulators; hence, the term semiconductor [21]. Meanwhile the conduction process in semiconductors differs from that in a metal in several respects.

The most important differences are that semiconductors conduct current through two

distinct and independent modes of electron motion, and that the relative importance of these two modes can be controlled over a wide range through the addition of minute quantities of appropriate elements to the basic semiconductor material. Although one mode of electron motion can be described in terms of a free electron gas, analogous to the situation in a metal, the other mode is described in terms of the flow of positive charge. While a metal's electrical resistivity is of the order of 10^{-8} W.m that of a semiconductor is about 10^{-1} W.m.

2.5.2. Semiconductors

A semiconductor is a material which is an insulator at absolute zero but which has valence electrons (outer electrons) loosely enough bound for a small proportion to be released by thermal motions at room temperature [22]. Such materials are called intrinsic semiconductors. Each electron freed in this way leaves a positive mobile "hole" in the lattice. Electrons and holes both carry current (though electrons have the higher mobility so they carry more current) and are present in equal numbers.

2.5.3. Types of semiconductors, Doping

The principles of semiconductor physics are best illustrated by the example of silicon or germanium, group IV elemental semiconductors. The silicon crystal forms the so-called *diamond lattice* where each atom has four nearest neighbours at the vertices of a tetrahedron [10]. The result of the bonding arrangement which uses the four outer (valence) electrons of each silicon atom is the four-fold tetrahedral coordination. Each bond contains two electrons, and you can easily see that all the valence electrons are taken up by the bonds. This crystal structure has a profound effect on the electronic and optical properties of the semiconductor. According to the quantum theory, the energy of an electron in the crystal must fall within well-defined *bands*. The energies of valence orbitals which form bonds between the atoms represent just such a band of states, the *valence band*. The next higher band is the *conduction band* which is separated from the valence band by the *energy gap*, or *bandgap*. The width of the bandgap $\boldsymbol{E_c - E_v}$ is a very important characteristic of the

semiconductor and is usually denoted by E_g. A pure semiconductor (which is called *intrinsic)* contains just the right number of electrons to fill the valence band, and the conduction band is therefore empty (Figure 2.3 below).

Electrons in the full valence band cannot move; just as, for example, marbles in a full box with a lid on top. For practical purposes, a pure semiconductor is, therefore, an insulator. Semiconductors can only conduct electricity if carriers are introduced into the conduction band or removed from the valence band.

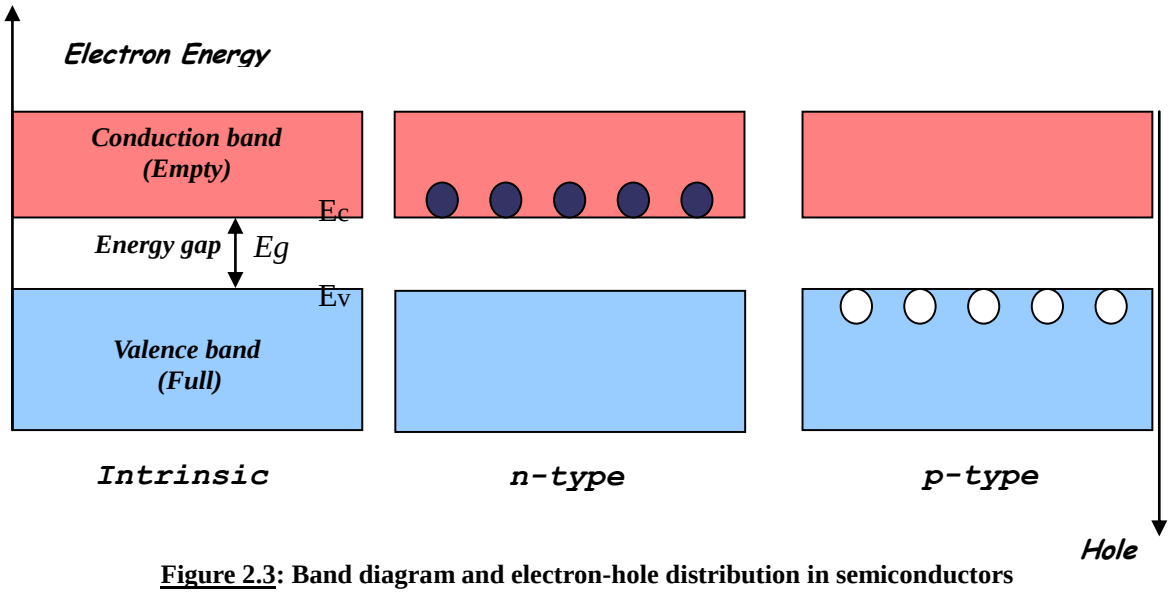

Figure 2.3: Band diagram and electron-hole distribution in semiconductors

One way of doing this is by alloying the semiconductor with an impurity. This process is called *doping*. Doping makes it possible to exert a great deal of control over the electronic properties of a semiconductor, and lies at the heart of the manufacturing process of all semiconductor devices. Suppose that some group V impurity atoms (for example, phosphorus) are added to the silicon melt from which the crystal is grown. Four of the five outer electrons are used to fill the valence band and the one extra electron from each impurity atom is therefore promoted to the conduction band (Figure above) [10]. For this reason, these impurity atoms are called *donors.* The electrons in the conduction band are mobile, and the crystal becomes a conductor. Since the current is carried by negatively charged electrons, this type of semiconductor is called *n-type.* A similar situation occurs when silicon is doped with group III impurity atoms (for example, boron) which are called *acceptors.* Since four electrons per atom are needed to fill the valence band completely, this doping creates

electron deficiency in this band. The missing electrons, called ***"holes"*** *behave* as positively charged particles which are mobile, and carry current. A semiconductor where the electric current is carried predominantly by holes is called *p-type.* The prevailing charge carriers in a given semiconductor are called *majority carriers.* Examples of majority carriers are electrons in an ***n***-type semiconductor and holes in the ***p***-type. The opposite type of carriers whose concentration is generally much lower are called *minority carriers* [10].

2.5.4. Movement of charge carriers: Mobility

Another important parameter of a semiconductor is the mobility $\boldsymbol{\mu}$ or charge carrier drift velocity $\boldsymbol{v}$ per unit field $\boldsymbol{E}$, given by the expression:

$$\boldsymbol{\mu} = {}^{|\boldsymbol{v}|}/_{\boldsymbol{E}} \qquad \textbf{[2.1]}$$

This parameter is positive for both holes and electrons. The electrical conductivity $\boldsymbol{\sigma}$ is the sum of contributions from the concentrations of electrons $\boldsymbol{n}$ and of holes $\boldsymbol{p}$ in accordance with the expression:

$$\boldsymbol{\sigma} = (\boldsymbol{ne\mu_e} + \boldsymbol{pe\mu_h}) \qquad \textbf{[2.2]}$$

where $\boldsymbol{e}$ is the electronic charge, $\boldsymbol{\mu_e}$ the mobility of electrons and $\boldsymbol{\mu_h}$ that of the holes. The power-law temperature dependence $\boldsymbol{T^n}$ for mobilities is weak, and the pronounced $\boldsymbol{T}$ dependence of the conductivity is due principally to the dependence of the electron and hole concentrations on the temperature [23].

In doped semiconductors, this generally arises mainly from Boltzmann factor $\boldsymbol{exp}\left({}^{-\boldsymbol{E_i}}/_{\boldsymbol{K_BT}}\right)$ associated with the ionization energies $\mathbf{E_i}$ of the donors or acceptors.

The thermal energy $\boldsymbol{K_BT} = \mathbf{0.026}\,\boldsymbol{eV}$ at room temperature (300 K) is often comparable to the ionization energies. In intrinsic semiconducting materials, the main contribution to the intrinsic concentrations of electrons $\boldsymbol{n_i}$ **,** is from the exponential factor $\boldsymbol{exp}\left({}^{-\boldsymbol{E_g}}/_{\mathbf{2}\boldsymbol{K_BT}}\right)$ in the following expression from the law of mass action:

$$n_i = p_i = 2\left(\frac{K_B T}{2\pi\hbar^2}\right)^{3/2} (m_e m_h)^{3/4} \, exp\left(-E_g / 2K_B T\right) \quad [2.3]$$

where the intrinsic concentrations of electrons n_i and of holes p_i are equal to each other because the thermal excitation of n_i electrons to the conduction band leaves behind the same number p_i of holes in the valence band, that is $n_i = p_i$.

We observe that the expression contains the product $m_e m_h$ of the effective masses m_e and m_h of the electrons and holes, respectively [23]. These effective masses strongly influence the properties of excitons.

2.5.5. Transport

2.5.5.1. Transport processes in bulk solids

Considering semiconductors as being composed of bulk regions and interfaces (e.g., contact and grain boundary) allows us to systematically address transport in these regions. The modelling of bulk-region conduction band and valence band transport using the concepts of drift and diffusion has been achieved [24]. In cases of multicrystalline and microcrystalline inorganic solids, the drift-diffusion model is strictly valid within crystals, so long as the scattering length is less than the characteristic dimension of the crystal. In polycrystalline materials, intragrain drift-diffusion transport may be in series with injection, recombination, or tunnelling processes at grain boundaries. For nanocrystalline materials, a drift-diffusion model can be achieved using an effective mobility, which depends on grain size. The drift-diffusion approach also works well for amorphous inorganic and amorphous and crystalline organic materials. In the case of amorphous materials, there can also be transport via the gap states in parallel with conduction band and valence band transport. For organic materials, transport between molecules controlled by tunnelling mechanisms can dominate in some cases. For nanoparticles, transport is expected to be interface dominated and also to depend on the matrix in which the particles are embedded. In the latter two situations, carriers may have to percolate through a solid as they search for optimum interface tunnelling paths [24].

The transport processes could be discussed more by considering the ***bulk region***

conduction band transport, the ***bulk region valence band transport*** and the ***transport processes at interfaces.*** Our interest lies in the last one.

2.5.5.2. Transport processes at interfaces

There are a number of processes unique to interfaces that can allow carriers to cross the boundary between two materials or between two grains [24]. These processes are in series with the bulk transport mechanisms just discussed. In this section we focus on these interfaces transport mechanisms.

A metal-semiconductor structure in forward bias is used in figure 2.4 below to illustrate them. From the figure it is seen that mechanisms ***a*** to ***e*** involve the semiconductor majority carriers, while mechanism ***f*** involves both majority and minority carriers. Mechanism ***g*** involves only minority carriers.

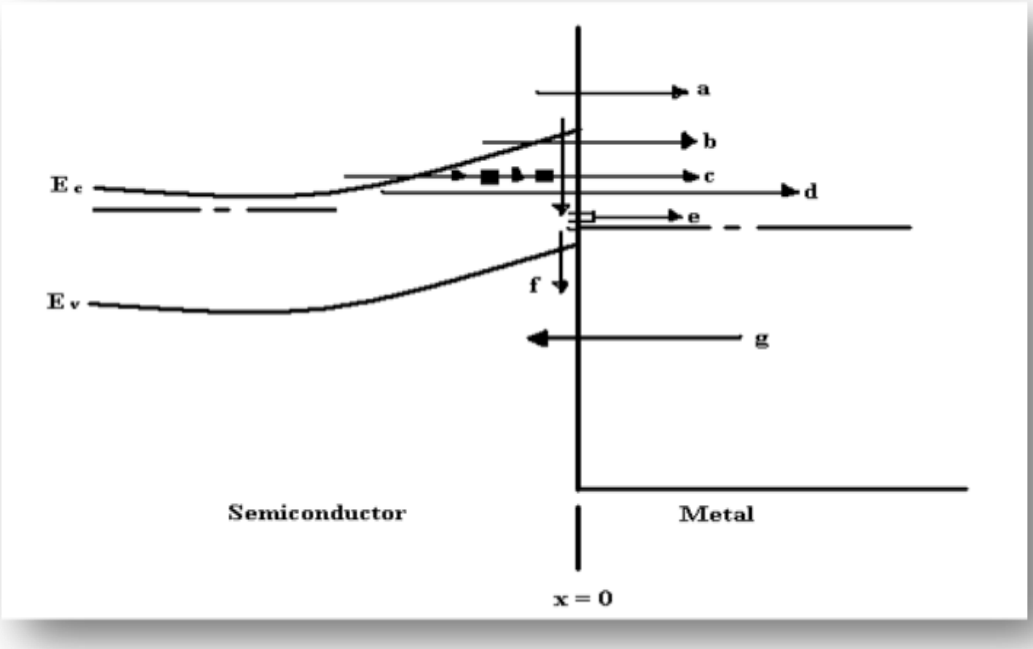

Figure 2.4: Interface transport mechanisms illustrated using a forward-biased, metal-semiconductor junction. Path (*a*) is thermionic emission, path (*b*) is thermally enhanced field emission, path (*c*) is multistep tunnelling, path (*d*) is field emission, path (*e*) involves trapping and subsequent emission, path (*f*) is interface recombination, and path (*g*) is minority-carrier injection [24].

Although here we discuss these mechanisms in the context of a metal semiconductor contact, the general features of these various interface transport mechanisms will also be found at other interfaces.

2.5.6. Recombination

Recombination processes can be classified in a number of ways. Some schools of thought say that recombination phenomena can be classified as direct and indirect processes. Direct recombination, also called band-to-band recombination, usually dominates in direct-gap semiconductors, such as gallium arsenide, whereas indirect recombination via bandgap recombination centers dominates in indirect bandgap semiconductors, such as silicon. But most texts distinguish between bulk and surface recombination, and between band-to-band recombination as opposed to transitions with the participation of defect levels within the band gap.

Recombination processes can also be classified according to the medium which absorbs the energy of the recombining electron-hole pair: radiative recombination (associated with photon emission), or the two principal non-radiative mechanisms by *Auger* and multi-phonon transitions, where the recombination energy is absorbed by a free charge carrier or by lattice vibrations, respectively. An opposite process to Auger recombination (where an electron hole pair is generated rather than consumed) is called impact ionisation [25].

2.5.6.1. Bulk Recombination Processes

In this section, we restrain ourselves to a brief overview of Auger, the defect-assisted and radiative recombination processes, the most frequently encountered in the practical operation of solar cells. These processes are depicted schematically in Figure 2.5 below which also presents the notation used to describe the relevant parameters [25].

The rate of band-to-band radiative recombination is given in the form of

$$\boldsymbol{U_{rad} = B(np - n_i^2)} \qquad \textbf{[2.4]}$$

where the coefficient B is sometimes written as R/n_i^2.

Radiative transitions between a free electron and a localised state within the band gap may also be important in certain situations, for example in novel concepts such as the impurity PV effect.

The rate of band-to-band Auger recombination can be written as

$$U_{Auger} = (C_{p0}p + C_{n0})(np - n_i^2) \quad [2.5]$$

where the two, usually most important Auger terms are given in the first bracket.

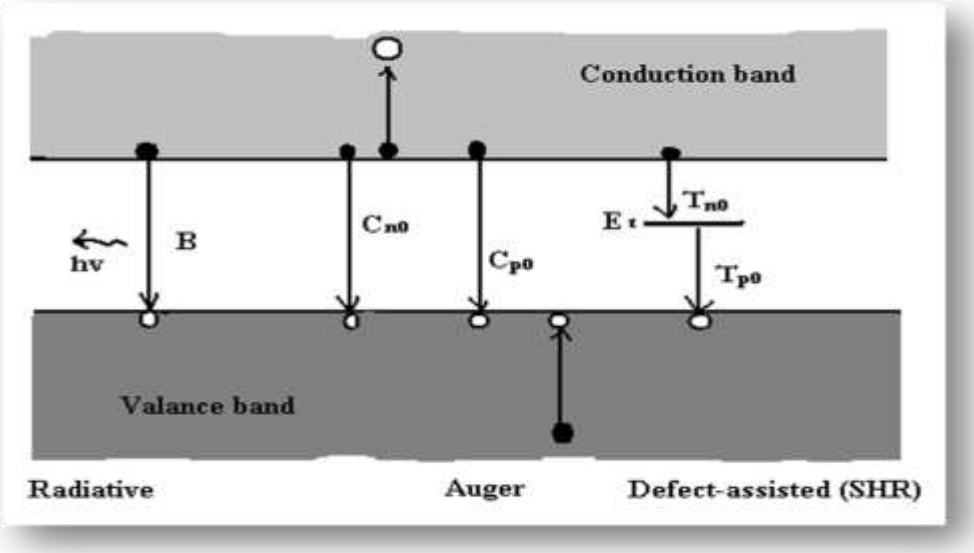

Figure 2.5: A schematic diagram of the principal recombination processes in semiconductors, and the notation for the rate constant adopted in this book. The direction of arrows indicates electron transitions [25]. C_{po} and C_{no} are the Auger terms

The recombination rate via defects of concentration N_t with a level at energy E_t within the band gap is described by the Shockley-Read-Hall formula:

$$U_{SHR} = \frac{np - n_i^2}{\tau_p(n+n_1)+\tau_n(p+p_1)} \quad [2.6]$$

where $n_1 = n_i \exp(\frac{E_t - E_i}{K_B T})$, $p_1 = p_i \exp(\frac{E_t - E_i}{K_B T})$ and τ_p, τ_n are parameters, proportional to the defect concentration N_t, which are characteristic for the particular

defect and energy level. At low injection, $\boldsymbol{\tau_p}$ and $\boldsymbol{\tau_n}$ assume the meaning of minority carrier lifetimes. With an appropriate dependence on the doping concentration and temperature, $\boldsymbol{\tau_n}$and $\boldsymbol{\tau_p}$ are also used extensively in material and device modelling.

2.5.6.2. Surface recombination

Surface recombination velocity is an important parameter which affects the dark saturation current and the quantum efficiency of solar cells. Similarly to dislocations and planar defects such as grain boundaries, surfaces (and interfaces in general) introduce band of electronic states in the band gap which can be traced to broken (or strained) bonds and impurities. A complete characterisation of surface recombination must also take into account the surface charge which may give rise to band bending. To achieve optimal operation, surface recombination is reduced by a window layer which prevents minority carriers from reaching the surface [25].

For an oxidised silicon surface, surface recombination velocity is strongly dependent on the surface roughness, contamination, ambient gases used during oxidation and the annealing conditions. Under identical process parameters, however, one can identify trends in the dependence of the surface recombination velocity on the surface doping concentration. *Cuevas et al.* [25] proposed the following analytical relationship between surface recombination velocity and doping concentration:

$$s = 70\ cm.s^{-1} \quad for\ \ N < 7 \times 10^{17} cm^{-3}$$
$$s = 70\left(\frac{N}{7\times10^{17}}\right)\ \ cm.s^{-1}\ \ forN > 7 \times 10^{17} cm^{-3} \qquad \textbf{[2.7]}$$

Equation (2.7) models several experimental results.

2.5.6.3. Minority-carrier lifetime

Under low injection (a regime of particular importance for solar cell operation), the majority carrier concentration can be assumed to be excitation independent, and the effect of recombination is discussed in terms of minority-carrier lifetime. In ***p***-type material, for example, the recombination rate can be written as [25]

$$U = \frac{1}{\tau_n}(n - n_0) \quad [2.8]$$

where τ_n is the minority-carrier (electron) lifetime.

An analogous equation can be written for the "hole" lifetime τ_p in ***n***-type material.

The inverse of the lifetime (the rate constant) is a sum of the different contributions to the lifetime:

$$\frac{1}{\tau} = \frac{1}{\tau_{rad}} + \frac{1}{\tau_{Auger}} + \frac{1}{\tau_{SRH}} \quad [2.9]$$

where τ stands for $\tau_p$or τ_n, as appropriate. This additive nature of the recombination rate constant is also useful when discussing the radiation damage.

The effect of lifetime on transport properties by carrier diffusion can be discussed in terms of the diffusion length which is defined by:

$$L = \sqrt{D_\tau} \quad [2.10]$$

where ***D*** is the diffusion constant for the minority carriers in question.

If, however, drift in electric field ***E*** is the dominant transport mechanism, it is appropriate to define the drift length as

$$l_n = E\tau_n\mu_n \qquad l_p = E\tau_p\mu_p \quad [2.11]$$

for electrons and holes as minority carriers. This parameter plays an important role in the analysis of ***p-i-n*** junction solar cells.

The contribution to lifetime due to defects, when combined with recombination in intrinsic material, has been empirically observed to follow the equations [25]

$$\frac{1}{\tau_{n,SRH}} = \left(\frac{1}{2.5\times10^{-3}} + 3\times10^{-13}N_D\right)\left(\frac{300}{T}\right)^{1.77}$$
$$\frac{1}{\tau_{p,SRH}} = \left(\frac{1}{2.5\times10^{-3}} + 11.76\times10^{-13}N_A\right)\left(\frac{300}{T}\right)^{0.57} \quad [2.12]$$

where the first term in the brackets applies for recombination in an intrinsic semiconductor. Similarly, the contribution to Equation (2.12) by Auger recombination

can be described by the expressions

$$\frac{1}{\tau_{n,Auger}} = (1.83 \times 10^{-31} p^2)\left(\frac{T}{300}\right)^{1.18}$$
$$\frac{1}{\tau_{p,Auger}} = (2.78 \times 10^{-31} n^2)\left(\frac{T}{300}\right)^{0.72} \quad \textbf{[2.13]}$$

Although the concept of minority carrier lifetime is most commonly applied to bulk recombination, a similar notion can be relevant for surface processes. For example, the effective lifetime observed of minority carriers with uniform concentration in a wafer can be written as

$$\frac{1}{\tau_{eff}} = \frac{1}{\tau_{RSH}} + \frac{2W}{A} S \quad \textbf{[2.14]}$$

where S is the value of the recombination velocity, W is the wafer thickness and A is the area of the sample.

2.5.7. Junctions

Solar cell's operation is dependent on the formation of a *junction.* Various types of junctions are shown in Figure (2.6) below.

Amongst them the ***p-n*** *junction* is the simplest, it consists of an interface between ***n*** and ***p*** regions of one semiconductor. Sometimes a layer of intrinsic material is incorporated between the ***n-*** and ***p***-type regions, forming a wider transition zone. In contrast with these *homojunctions,* two different semiconductors formed a *heterojunction* [10].

An interface between a metal and a semiconductor also forms a junction, called the *Schottky barrier.* The actual materials in question in general dictate the properties of metal contacts with a semiconductor.

For each semiconductor, some metals form a Schottky barrier but some form an *ohmic contact* where the barrier is absent. These contacts serve as media for the extraction of electrical current from the device.

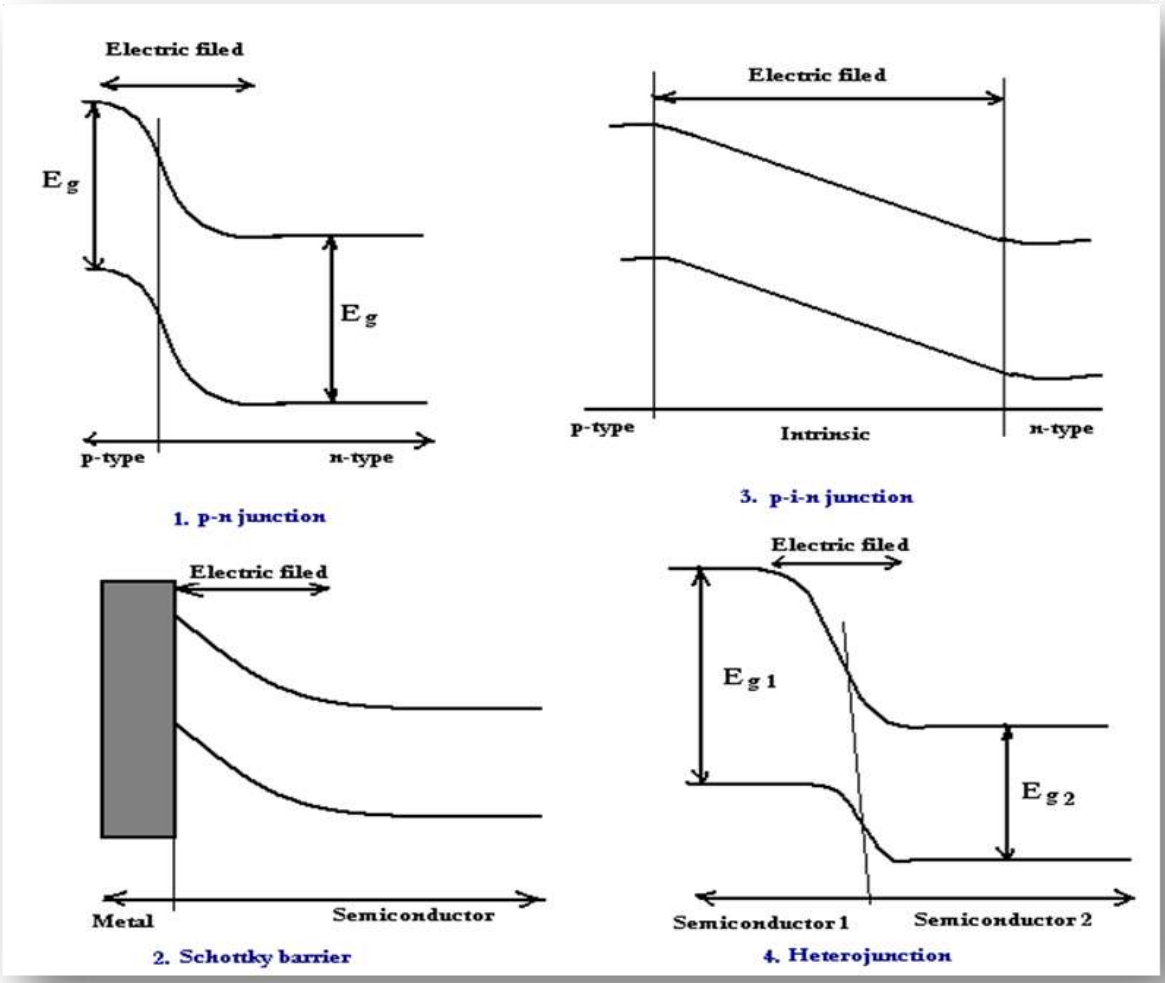

Figure 2.6: Band diagram of semiconductor junctions [10]

The important feature of all junctions is that they contain a strong electric field. To illustrate how this field arises, let us consider a hypothetical situation where the ***p-n*** junction is formed by bringing together into contact two pieces of semiconductor, one ***p***-type and the other ***n***-type. Although this manner of junction formation is not normally used in practice, it is a convenient medium to showcase the relevant principles.

In separation, there is excess of electron in the ***n***-type material and excess of hole in the ***p***-type. When the two pieces are joined, electrons from the ***n*** side near the interface diffuse into the ***p*** side, leaving behind a layer which is positively charged by the donors.

Similarly, holes diffuse in the opposite direction, leaving behind a negatively charged layer deprived of holes. The resulting junction region then contains practically no mobile charge carriers, and the fixed charges of the dopant atoms create a potential barrier acting against a further flow of electrons and holes. Note that the electric field in the junction pulls the electrons and holes in opposite directions.

Figure 2.7 shows the band diagram of a ***p-n*** junction diode in equilibrium, and when external voltage is connected to the diode. Without bias, of course, there is no current through the junction.

We may imagine this zero net current as consisting of two very small opposite currents I_0 and $-I_0$ which remain from the current flow prior to the junction formation.

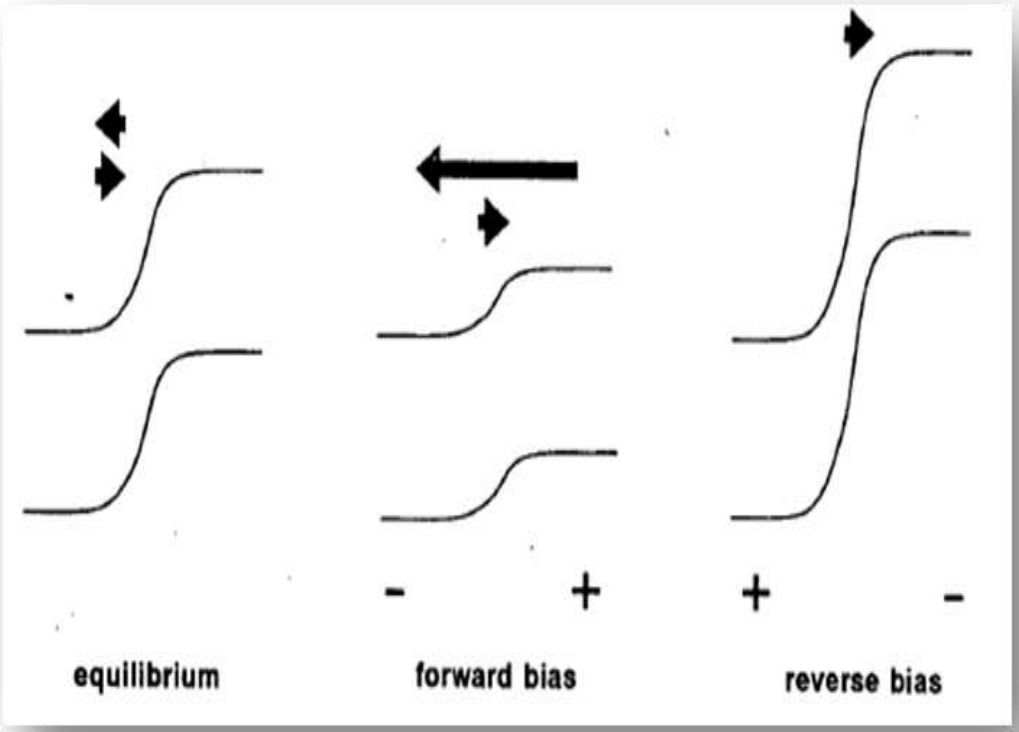

Figure 2.7: p-n junction band diagram in equilibrium and reverse/forward bias mode [10]

These currents are very small indeed, corresponding to a current density of the order of $10^{-14}\, A.cm^{-2}$ in a good silicon diode.

This current balance is changed considerably when voltage is applied to the junction. A forward bias, i.e. positive voltage applied to the *p* side, reduces the height of the potential barrier. This, in turn, dramatically increases the current through the diode. Under reverse bias, on the other hand, the barrier is increased. This has a much smaller effect on the device, and produces only the tiny current I_0 (the *dark saturation current),* which is much smaller than the current under forward bias. The junction therefore acts as a rectifier, or diode. In mathematical terms, the ***I-V*** characteristic of a diode is given by the Shockley equation:

$$\boldsymbol{I = I_0[\exp\left(\frac{qV}{K_BT}\right) - 1]} \qquad \textbf{[2.15]}$$

where I is the current, q is the magnitude of the electron charge, V is the voltage, k_B is the Boltzmann constant, and T is the absolute temperature. The *I-V* characteristic in equation (2.15) is shown in Figure (2.8) below.

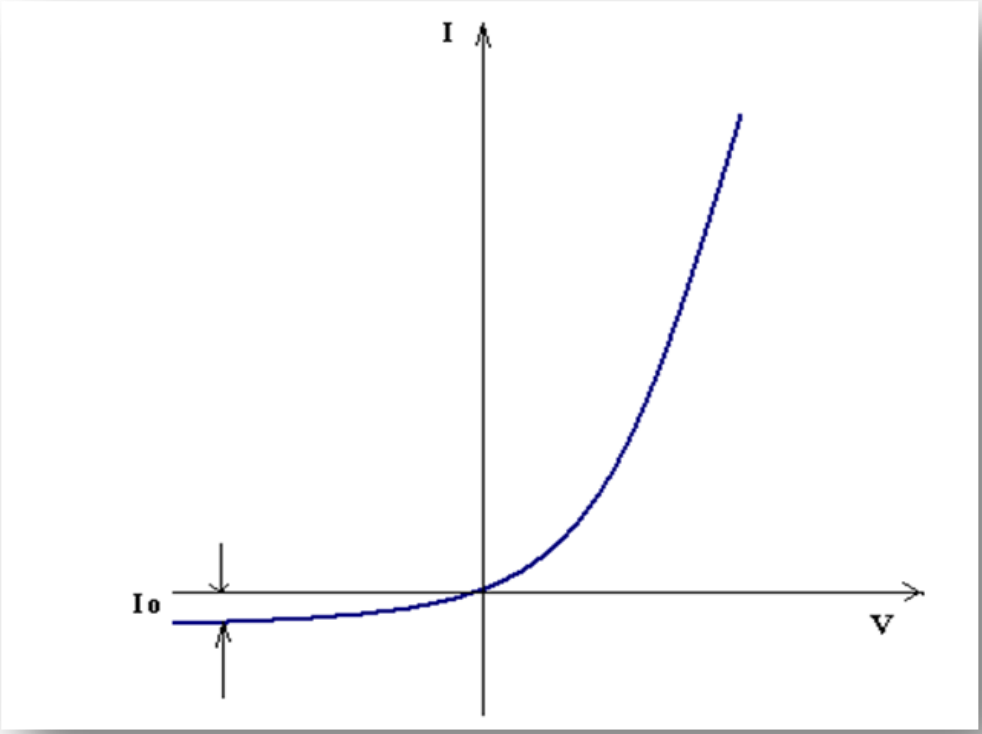

Figure 2.8: The diode I-V characteristic [7]

2.5.8. Barriers

A barrier, also known as *barricade* is a physical structure which blocks or impedes something or anything that restrains or obstructs progress and/ or access.

However, a single semiconductor crystal manufactured with ***p***-type material at one end and ***n***-type material at the other in Figure 2.9 below has some unique properties.

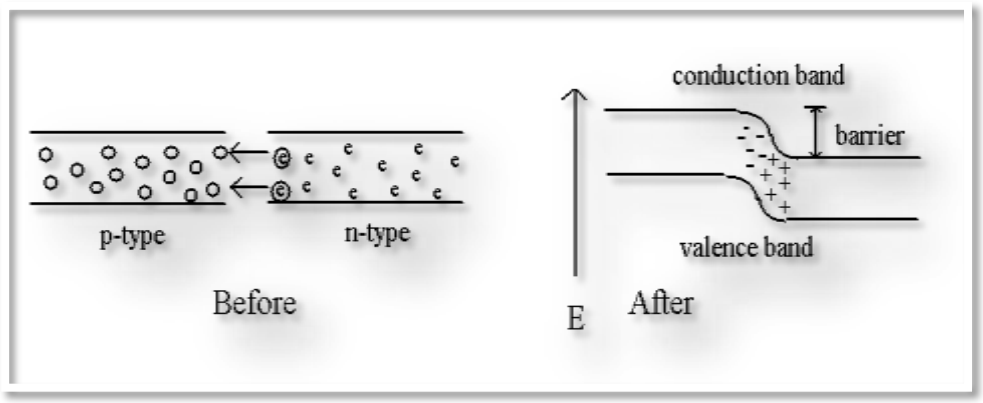

Figure 2.9: Barrier

The ***p***-type material has positive majority charge carriers, holes, which are free to move about the crystal lattice. The ***n***-type material has mobile negative majority carriers, electrons.

Near the junction, the ***n***-type material electrons diffuse across the junction, combining with holes in ***p***-type material. The region of the ***p***-type material near the junction takes on a net negative charge because of the electrons attracted. Since electrons departed the ***n***-type region, it takes on a localized positive charge.

The thin layer of the crystal lattice between these charges has been depleted of majority carriers, thus, is known as the *depletion region*. It becomes nonconductive intrinsic semiconductor material. In effect, we have nearly an insulator separating the conductive ***p*** and ***n*** doped regions.

This separation of charges at the ***p-n*** junction constitutes a potential barrier shown in Figure 2.10 below. This potential barrier must be overcome by an external voltage source to make the junction conduct. The formation of the junction and potential barrier happens during the manufacturing process.

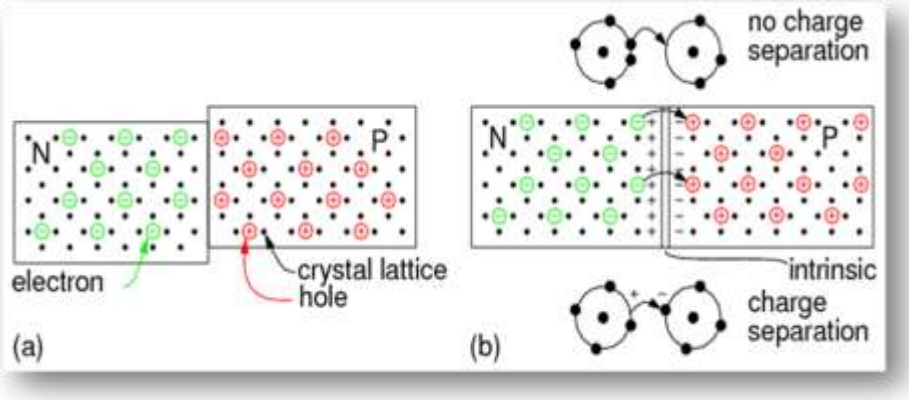

Figure 2.10: (a) Blocks of P and N semiconductor in contact have no exploitable properties (b) Single crystal doped with P and N type impurities develops a potential barrier

The magnitude of the potential barrier is a function of the materials used in manufacturing. Silicon ***p-n*** junctions have a higher potential barrier than germanium junctions. It is characteristic of the semiconductor device; it is the voltage in a semiconductor device on either side of a ***p-n*** junction. Free electrons from the ***n***-material migrate across the junction to fill some of the holes in the ***p***-material. This migration causes a positive potential at the edge of the ***n***-material, and a negative potential at the edge of the ***p***-material. The potential barrier, sometimes called the potential hill, blocks any forward current flow across the junction until the forward voltage is higher than that of the potential barrier. The potential barrier in a silicon device is approximately 0.7 Volts and approximately 0.3 Volts in a germanium device.

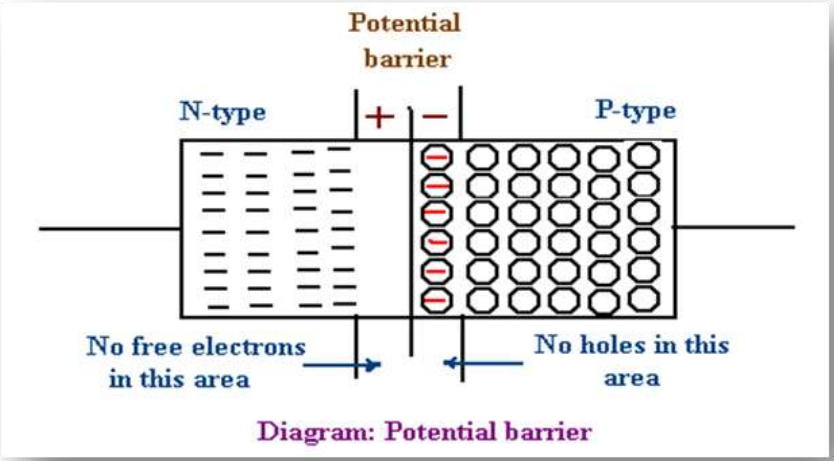

Figure 2.11: Diagram showing potential barrier

2.5.9. Two-terminal devices

There are four types of two-terminal semiconductor devices: ***p-n*** junctions, Schottky barriers, heterojunctions, and metal-insulator-semiconductor (MIS) capacitors. These devices are fundamental; since all more complicated three-terminal and multi-terminal semiconductor electronic devices consist of combinations of these basic two-terminal devices.

2.5.9.1. *p-n* junctions

A strong argument can be made that the ***p-n*** junction is the most fundamental semiconductor device [26], in terms of semiconductor device explication and functionality.

Bipolar device operation depends on the availability of both carrier types - electrons and holes - and is, to a large extent, dominated by minority carrier action [27]. Although a ***p-n*** junction is the simplest possible bipolar device, it has a wide range of applications, including its use as a rectifier, temperature sensor, solar cell, photodiode, light-emitting diode (LED), and laser. A ***p-n*** junction is also a critical constituent of many types of more complicated bipolar devices, including a bipolar junction transistor, an insulated-gate bipolar transistor etc...

In contrast to a bipolar device, the operation of a *unipolar* device depends, to a large extent, on only one carrier type. Examples of unipolar devices include Schottky barriers, thin film transistors (TFTs), transparent thin film transistors (TTFTs), and field-effect transistors (FETs).

Unipolar devices are better suited to transparent electronics applications. First, visible transparency mandates the use of wide band gap semiconductors. It is difficult, and often impossible, to obtain bipolar doping in many of these materials, which have a strong tendency to remain either strongly insulating or unipolar, probably as a consequence of their tendency towards vacancy self-compensation [28]. Second, efficient bipolar operation requires long minority carrier lifetimes. In turn, this minority carrier lifetime requirement usually mandates the use of single crystals. We think that the use of single crystal materials will be cost-prohibitive in most

transparent electronics applications, in which polycrystalline or amorphous materials will predominate. There are many transparent electronics applications which would greatly benefit from the availability of a ***p-n*** junction. In particular, a low-cost, large-area inorganic-LED (ILED) would be immensely useful for transparent displays and for other important and elusive applications.

Although we do not expect to see ILEDs or other transparent bipolar device types commercially available in the near future, given their obvious utility, it is possible that they may emerge sooner than we expect. To encourage this type of development, we offer the following thoughts regarding their realization.

First, we believe that anisotype (i.e., ***p-n***) heterojunctions offer a better route to the realization of an ILED than a conventional ***p-n*** homojunction, given the tendency for a wide band gap semiconductor to undergo selfcompensation [28].

Second, if layers approaching single crystal quality can be grown at low-cost and over large areas, this is probably the best way to proceed since these materials will have better performance than poorer crystalline devices.

This will require perfecting novel growth strategies similar to those under development for silicon-based applications, such as metal-induced crystallization or continuous-grain silicon growth [29].

Fourth, polycrystalline bipolar devices may also be feasible if minority carrier reflecting grain boundaries, such as those observed in Cu-$InSe_2$ solar cells, can be designed using wider band gap transparent materials [30].

Fifth, bipolar amorphous semiconductors would be ideal for transparent electronics, in terms of cost and manufacturability, if their minority carrier lifetime properties were good enough; this appears to be a difficult challenge.

2.5.9.2. Schottky barrier

A Schottky barrier, named after *Walter H. Schottky*, is a potential barrier formed at a metal-semiconductor junction which has rectifying characteristics, suitable for use as a diode. The largest differences between a Schottky barrier and a ***p-n*** junction are its typically lower junction voltage, and decreased (almost nonexistent) depletion width in the metal. To appreciate Schottky barriers at a fundamental level, our first task is to

elucidate Schottky barrier formation from an energy band diagram perspective [31].

To do this, begin with a metal-semiconductor junction according to **ideal** Schottky barrier theory, as illustrated by the energy band diagrams shown in Figure 2.12. Figure 2.12 a. depicts an energy band diagram for an isolated metal and an isolated ***n***-type semiconductor (valence band not shown) in terms of the metal and semiconductor work functions, Φ_M and Φ_S, and the semiconductor electron affinity, χ_S.

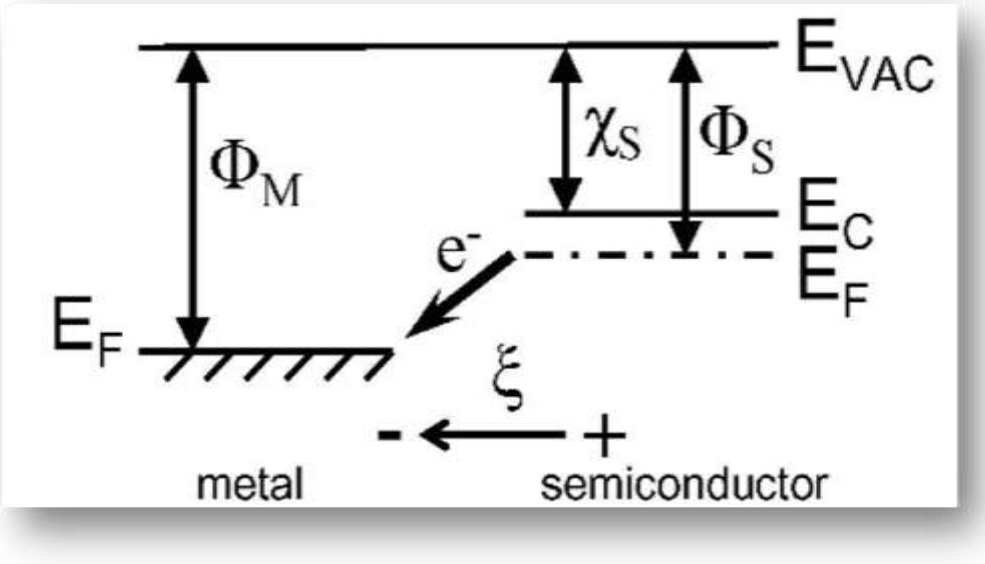

Figure 2.12: Energy band diagrams for (a) an isolated metal and an isolated n-type semiconductor (valence band not shown) with $\Phi_M > \Phi_S$ [31]

When the metal and semiconductor of Figure 2.12a. are brought together into intimate contact, electron transfer occurs from the semiconductor to the metal, giving rise to the formation of a *macroscopic* negative *dipole*, as indicated by the lower left-pointing arrow in Figure 2.11a. This *dipole* consists of a negative interfacial charge sheet, which is balanced by an equal density of positive charge in an extended space charge region within the semiconductor. Such a dipole is denoted *macroscopic* since the sheet of negative interfacial charge and the charge centroid of the space charge region define a dipole with a spatial dimension on the order of the space charge region dimension. The direction of charge transfer, and hence the polarity of the dipole, is determined by the relative Fermi level positions of the metal and semiconductor.

Figure 2.12.b. shows an energy band diagram of the Schottky barrier formed after the metal and semiconductor come into contact for this ideal model case. The effect of charge transfer is evident from the positive curvature of the semiconductor conduction band near the interface. Two electronic barriers are established as a consequence of this interfacial charge transfer; the ***n***-type semiconductor Schottky barrier height, φ_{Bn}, and the built-in potential, V_{BI}.

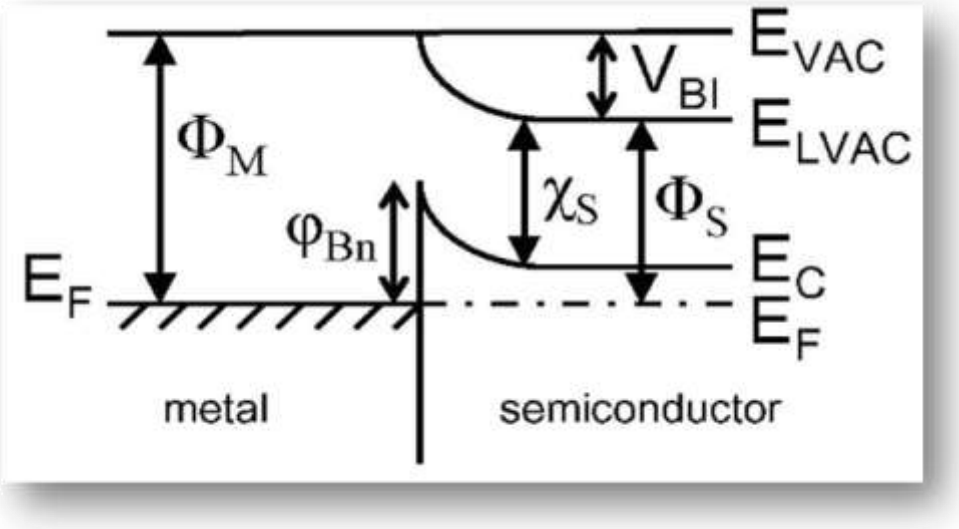

(b) The corresponding Schottky barrier band structure for an ideal interface (i.e., charge exchange is exclusively Fermi-level mediated, as indicated by the upper arrow shown in (a))

Figure 2.12: Ideal charge exchange results in the formation of a *macroscopic* negative *dipole*, as indicated by the bottom arrow in (a) [31]. Φ_M and Φ_S are semiconductor work functions and χ_S is the semiconductor electron affinity.

Each of these barriers acts to prevent electron transfer in opposing directions across the interface. The presence of a majority carrier barrier in the semiconductor means that this metal semiconductor junction will function as a Schottky barrier, which in turn means that it will be characterized by rectifying, i.e., diode-like, current-voltage curves. An important feature of this ideal model interface is the fact that the local vacuum level is continuous across the interface [31].

In summary, **ideal** Schottky barrier formation is a consequence of Fermi-level-mediated charge transfer, giving rise to a *macroscopic* interfacial *dipole*.

Schottky barriers, with their lower junction voltage, find application where a device

better approximating an ideal diode is desired. They are also used in conjunction with normal diodes and transistors, where their lower junction voltage is used for circuit protection (among other things). In addition, because of their majority carrier conduction mechanism, Schottky diodes can achieve greater switching speeds than ***p-n*** junction diodes, making them appropriate to rectify high frequency signals.

2.5.9.3. Heterojunctions

Most of the developments that have improved performance of organic photovoltaic devices are based on donor-acceptor heterojunctions. At the interface between two different materials, electrostatic forces result from the differences in electron affinity and ionisation potential. If both electron affinity and ionisation potential are greater in one material (the electron acceptor) than the other (the electron donor) then the interfacial electric field drives charge separation (Figure 2.13 below).

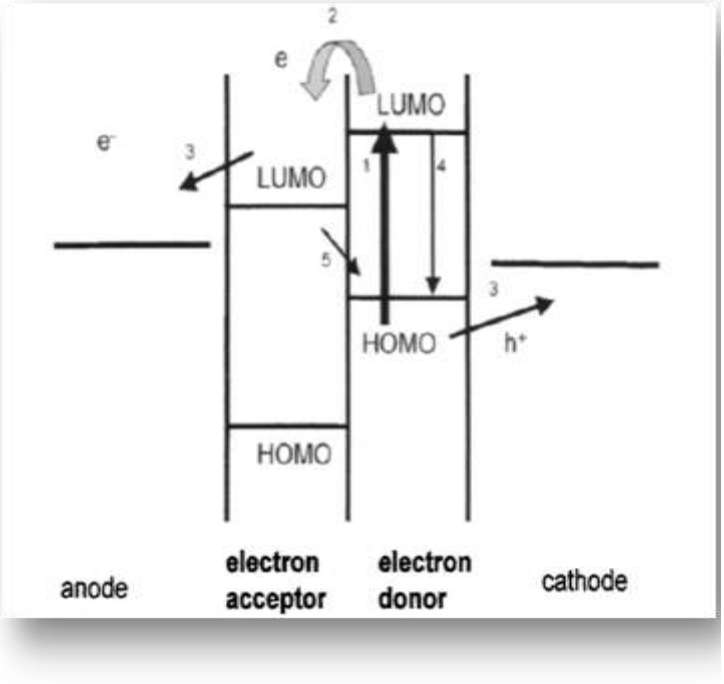

Figure 2.13: Schematic energy-band diagram of a donor-acceptor heterojunction. If both the excited state (LUMO) and ground state (HOMO) of the donor material lie at energies sufficiently higher than those of the acceptor material, then it is energetically favourable for an exciton reaching the interface to dissociate, leaving a positive polaron on the acceptor and a negative polaron on the donor. For efficient photocurrent generation, charge separation (2) should compete successfully with geminate recombination (4) after a photon absorption event (1), and transfer to contacts (3) should compete with interracial recombination (5) [25].

These local electric fields are strong and may break up photo-generated excitons provided that the differences in potential energies are larger than the exciton binding energy. In a planar heterojunction, or "bilayer" device, the organic donor-acceptor interface separates excitons much more efficiently than the organic-metal interfaces

in a single layer device and with very high purity materials, PV devices with high quantum efficiency (QE) may be made.

A revolutionary development in organic PVs (and photo-detectors) came in the mid 1990s with the introduction of a dispersed heterojunction, where an electron accepting and an electron donating material are blended together [25]. If the domain size in either material is similar to the exciton diffusion length, then wherever an exciton is photo-generated in that material, it is likely to diffuse to an interface and break up. If continuous paths exist in each material from the interface to the respective electrodes, then the separated charge carriers may travel to the contacts and deliver current to the external circuit as shown in Figure 2.14a. below.

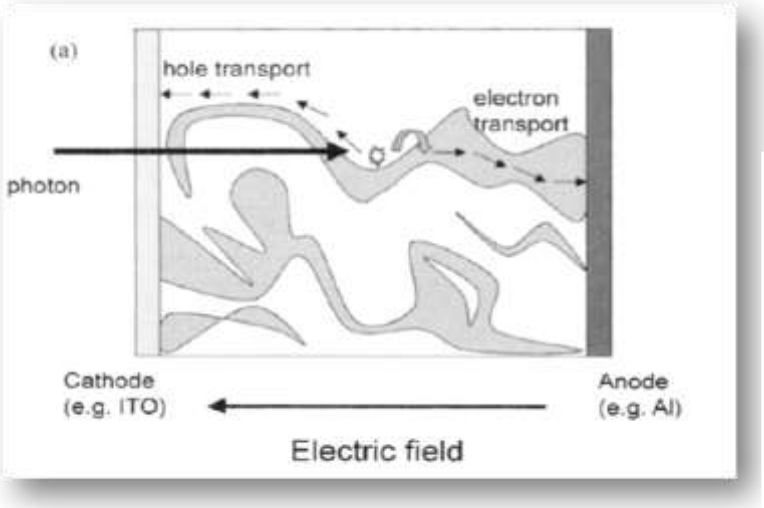

(a) A blend of two polymers

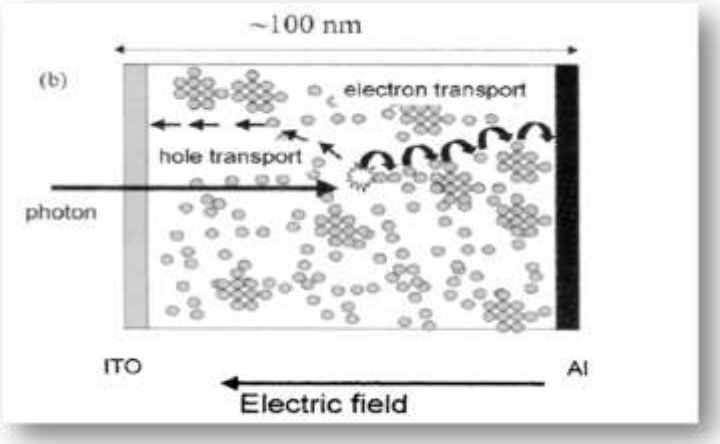

(b) **A blend of one polymer with electron accepting nanoparticles or fullerenes**

Figure 2.14: Domain size in the blend is similar to the exciton diffusion length, then the probability that an exciton will reach the interface and dissociate is high. For efficient photocurrent collection, each material must provide a continuous path for the transport of separated charge to the contacts. Isolated domains can trap charges, causing recombination. The concentration of nanoparticles should be sufficient to allow percolation [25].

This effect was reported independently by several groups [32] for a blend of two conjugated polymers. The blend improved QE to around 6-8% from less than 1% for either polymer alone. Around the same time, *Yu and co-workers* reported a QE of 29% for a blend of the hole transporter, poly-phenylene vinylene (PPV), with a derivative of C_{60} [33], where the C_{60} acts as the electron transporting component (Figure 2.14b above).

This was followed by observations of enhanced QE in heterojunctions made from conjugated polymers with inorganic nano-crystals [34] and organic dye crystals [35]. The demonstration of improved QE with dispersed heterojunctions represents a departure from the device physics of conventional solar cells and has led to new device and materials designs. The principles of operation are shared by dye sensitised solar cells which are discussed in reference [36].

2.5.10. Band theory

2.5.10.1. Valence band/Conduction band

Due to the very large number of atoms that interact in a solid material, the energy levels are so closely spaced that they form bands. The highest energy filled band, which is analogous to the highest occupied molecular orbital in a molecule (HOMO), is called the ***valence band***. The next higher band, which is analogous to the lowest unoccupied molecular orbital (LUMO) in a molecule, is called the ***conduction band***. The energy separation between these bands is called the ***energy gap***, $\boldsymbol{E_g}$.

The filling of these bands and the size of the energy gap determine if a material is a conductor (a metal), a semiconductor, or an insulator. In metals there is no energy gap between filled and unfilled energy levels. In semiconductors $\boldsymbol{E_g}$ is small, while in insulators $\boldsymbol{E_g}$ is large.

2.5.10.2. Bandgap

It is with uneasiness that most authors approach the section on band theory in most solid state physics books. The Schrödinger equation with a periodic potential is

needed, and then all that is necessary is for a suitable wave function to be substituted in the equation and this will bring forth energy bands and energy gaps. Unfortunately, a satisfactory treatment is not so simple, and a useful guess at the solution requires more intuition than is possessed by most people. Yet, the whole idea of band gaps is so vital to our understanding of semiconductors and their applications that it seems essential that some kind of reasonable justification for their existence should be given. There is no doubt that the simplest qualitative explanation for the existence of bands and gaps is given by the tight binding theory which is a subject of great debate in physics.

2.5.10.3. Energy band structure

How the periodic crystalline structure of the semiconductor establishes its electronic properties is of more consequence to the physics of solar cells. An electron moving in a semiconductor material is analogous to a particle confined to a three-dimensional box that has a complex interior structure due primarily to the potential fields surrounding the component atom's nucleus and tightly bound core electrons. The dynamic behaviour of the electron can be established from the electron wave function, ψ, which is obtained by solving the time-independent Schrödinger equation [37]:

$$\nabla^2\psi + \frac{2m}{\hbar^2}[E - U(\vec{r})]\psi = 0 \qquad [2.16]$$

where m is electron mass, $\hbar$ is the reduced Planck constant, E is the energy of the electron, and $U(r)$ is the periodic potential energy inside the semiconductor. Solving this quantum-mechanical equation is beyond the scope of this work, but suffice it to say that the solution defines the band structure (the allowed electron energies and the relationship between the electron's energy and momentum) of the semiconductor. Amazingly, this tells us that the quantum mechanically computed motion of the electron in the crystal is, to a good approximation, like that of an electron in free space if its mass, m, is replaced by an effective mass, m_e, in Newton's law of motion from classical mechanics:

$$F = m \times a \qquad [2.17]$$

where $\boldsymbol{F}$ is the applied force and $\boldsymbol{a}$ is the acceleration of the electron. A simplified energy band structure is illustrated in Figure 2.15. The allowed electron energies are plotted against the crystal momentum, $\boldsymbol{p} = \hbar \boldsymbol{k}$, where k is the wave vector (represented here as a scalar for simplicity) corresponding to the wave function solutions of the Schrödinger equation.

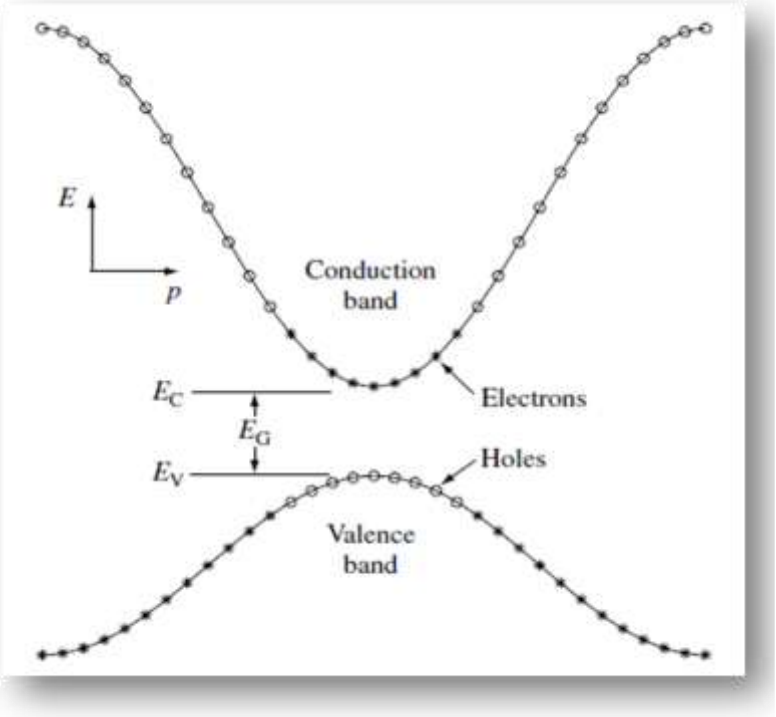

Figure 2.15: A simplified energy band diagram at $T > 0\ K$ for a direct band gap (E_G) semiconductor. Electrons near the maxima in valence band have been thermally excited to the empty states near the conduction-band minima, leaving behind holes. The excited electrons and remaining holes are the negative and positive mobile charges that give semiconductors their unique transport properties [37].

Only the energy bands of immediate interest are shown (energy bands below the valence band are presumed to be fully occupied by electrons and those above the conduction band are presumed to be empty). The electron effective mass is thus defined as:

$$\boldsymbol{m}^* \equiv \left[\frac{\boldsymbol{d^2E}}{\boldsymbol{dp^2}}\right]^{-1} = \left[\frac{\boldsymbol{1}}{\hbar^2}\frac{\boldsymbol{d^2E}}{\boldsymbol{dk^2}}\right]^{-1} \qquad \textbf{[2.18]}$$

Notice that the effective mass is not constant within each band. In addition, near the top of the valence band, the effective mass is actually negative. Electrons fill the states from bottom to top and the states near the top of the valence band are empty

due to some electrons being thermally excited into the conduction band. These empty states can conveniently be regarded as positively charged carriers of current called holes with a positive effective mass.

2.5.10.4. Fermi level and Fermi energy

The energetic position of the Fermi-level in semiconductors is important for two reasons:

- Together with the work function of the metal the Fermi level determines whether a blocking or ohmic contact is formed at the semiconductor/metal interface
- The relative position of the Fermi levels is a measure for the type of conductivity – whether the semiconductor conducts preferably holes in the VB (p-type) or electrons in the CB (n-type)

The energetic position of the Fermi level in a semiconductor represents the balance between the concentration of holes and electrons that occupy allowed energy levels under equilibrium condition (dark, no applied voltage). If the Fermi-level is closer to the CB, the material is called n-type conductor, since more electrons are available for conduction than holes - otherwise it is called p-type conducting [38].

Thus, the position of the Fermi level can be written as a function of both the effective density of states in the conduction band N_c and valence band N_v as well as the concentration of donors N_d and acceptors N_a :

For n-type semiconductors this gives [39]:

$$\boldsymbol{E_f = E_c - K_B T ln\left(\frac{N_c}{N_d}\right)} \qquad \textbf{[2.19]}$$

whereas for p-type semiconductors the relation is:

$$\boldsymbol{E_f = E_V - K_B T ln\left(\frac{N_v}{N_a}\right)} \qquad \textbf{[2.20]}$$

E_V and E_c stand for the top edge of the VB and the bottom edge of the conduction band respectively.

When voltage is applied and/or the semiconductor is illuminated, the concept of a Fermi level can no longer be applied. Upon illumination the increased concentration of electrons in the CB would shift E_f up while the higher concentration of holes in the VB would require shifting E_f down at the same time. As a consequence, two separate Fermi levels (the so called quasi Fermi-levels) are then introduced to describe the situation under this non equilibrium condition [40]:

$$E_{FN} = E_c + K_B T ln\left(\frac{n}{N_c}\right) \quad \textbf{[2.21]}$$

and

$$E_{FP} = E_V + K_B T ln\left(\frac{N_c}{p}\right) \quad \textbf{[2.22]}$$

with n and p denoting the concentration of electrons in the CB and holes in the VB. E_{FP} and E_{FN} are the quasi Fermi-levels that are associated with the balance of electrons and holes - both exist at the same time in one semiconductor.

2.5.10.5. The Fermi level and intrinsic semiconductors

Electrons are fermions, and thus follow Fermi-Dirac distribution function [41]:

$$f(E) = \frac{1}{exp\left(\frac{E-\mu}{K_B T}\right)+1} \quad \textbf{[2.23]}$$

where μ is the *Fermi energy* often denoted E_f or chemical potential. A chemical potential in semiconductor physics is the energy at which there would be a 50% chance of finding an electron, if all energy levels were allowed. In order to apply the statistics, we need the density of states in the conduction and valence bands.

These are derived from the basic principle that the density of states is constant in k-space. In the conduction band the density of states is given by [41]:

$$g(E) = \frac{V}{2\pi^2\hbar^3}(2m_e)^{3/2}(E - E_g)^{1/2} \quad \textbf{[2.24]}$$

and the valence band,

$$g(E) = \frac{V}{2\pi^2\hbar^3}(2m_h)^{3/2}(-E)^{1/2} \quad \textbf{[2.25]}$$

where *E* is calculated from the top of the valence band.

$$F_{1/2}(E) = e^{\left[\frac{-(E-\mu)}{K_BT}\right]} \quad \textbf{[2.26]}$$

The density of electrons in the conduction band is

$n = \frac{N}{V} = \frac{1}{V}\int_{E_g}^{\infty} f(E)g(E)dE$ and carrying out the integration we arrive at:

$$n = 2\left(\frac{2\pi m_e K_B T}{\hbar^2}\right)^{3/2} e^{\left[\frac{-(\mu - E_g)}{K_B T}\right]} \quad \textbf{[2.27]}$$

In the valence band, the probability of a hole is

$$F_h = 1 - F(E) \cong e^{\left[\frac{(E-\mu)}{K_BT}\right]} \quad \textbf{[2.28]}$$

A similar calculation yields the hole density

$$p = 2\left(\frac{2\pi m_h K_B T}{\hbar^2}\right)^{3/2} e^{\left(\frac{-\mu}{K_B T}\right)} \quad \textbf{[2.29]}$$

However numerous approximations have been formulated to calculate the Fermi level.

The value of μ depends on N_a and N_d. However μ can be eliminated between (2.27) and (2.29) to give the important relation [41]:

$$np = n_i^2 = N_c N_v \, exp\left(\frac{-E_g}{K_B T}\right) \quad \textbf{[2.30]}$$

where N_v and N_c are the prefactors in (2.27) and (2.29).

$$N_c = 2\left(\frac{2\pi m_e K_B T}{\hbar^2}\right)^{3/2}$$

$$N_v = 2\left(\frac{2\pi m_h K_B T}{\hbar^2}\right)^{3/2} \quad \textbf{[2.31]}$$

As stated, equation (2.30) holds for all T and independent of the values of N_a and N_d. In the intrinsic region, the extrinsic density is negligible, and then $n = p$ since each electron excited to the conduction band leaves a hole behind it. In the intrinsic region, therefore

$$n_i = p_i = (N_c N_v)^{1/2}\, exp\left(\frac{-E_g}{2K_B T}\right) \quad \textbf{[2.32]}$$

If we substitute into (2.32) the values of n and p from (2.27) and (2.29)

$$(m_e)^{3/2}\, e^{\left[\frac{-(\mu - E_g)}{K_B T}\right]} = (m_h)^{3/2}\, e^{\left(\frac{-\mu}{K_B T}\right)} \quad \textbf{[2.33]}$$

This gives the value of μ in the intrinsic region, simple manipulation leads to

$$\mu = \frac{1}{2}E_g + \frac{3}{4}K_B T\, ln\left(\frac{m_h}{m_e}\right) \quad \textbf{[2.34]}$$

That is, μ is displaced from the middle of the band gap by a temperature dependent term that depends on the ratio of the effective masses.

2.5.10.6. The Fermi level and extrinsic Semiconductors

What happens to μ with temperature when donors and acceptors are present? The charge neutrality condition governs the numbers of carriers [41].

$$n + N_a^- = p + N_d^+ \quad \textbf{[2.35]}$$

where N_d^+ and N_a^- are the number of ionised acceptor and donor sites. The number of sites that are ionised is:

$$N_d^+ = N_d\left[1 - F(E_g - E_d)\right] \quad \textbf{[2.36]}$$

A similar argument shows that

$$N_a^- = N_a\, f(E_a) \quad \textbf{[2.37]}$$

The four terms in equation (2.35) are given in terms of μ in equations (2.27), (2.37), (2.29) and (2.36) respectively, so μ can in fact be determined from (2.28). The general case has to be dealt with numerically.

We take the case of n-type doping but with some counter-doping:

$N_d > N_a$ and $N_a > 0$

At $T = 0$, N_a electrons move off donor sites to occupy the acceptor sites. Thus

$$N_d^+ = N_a \quad \textbf{[2.38]}$$

The donor sites are partially occupied. This is only possible at $T = 0$ if the Fermi-level is at the donor-site energy: $\mu = E_g - E_d$ **[2.39]**

This will not change for very low temperatures, $K_B T \ll E_d$, so substitution of the value of μ into (2.27) gives

$$n = N_c\, exp\left(\frac{E_a}{K_B T}\right) \quad \text{for} \quad K_B T \ll E_d \quad \textbf{[2.40]}$$

The important technical region in the n-type material is the temperature range in which all the donors are ionised and the extrinsic electron density is higher than the intrinsic density. Full ionisation means: $n = N_d - N_a$ **[2.41]**

Since N_a electrons are required for occupation of the acceptor sites. Comparing equation (2.32) to the change in energy of a wave packet with a time derivative approach gives [41]:

$$\mu = E_g - K_B T \ ln\left(\frac{N_c}{N_d - N_a}\right) \quad [2.42]$$

The corresponding results for p-type doping are $p = N_a - N_d$ [2.43]

$$\mu = E_g - K_B T \ ln\left(\frac{N_v}{N_a - N_d}\right) \quad [2.44]$$

Note that in this technical region if the counter doping is negligible, $N_a \ll N_d$ or $N_d \ll N_a$, equations 2.41 and 2.43 simplify to $n = N_d$ and $p = N_a$ [2.45] respectively, which is what is known to the engineers.

2.5.10.7. Fermi-Dirac Statistical Distribution Function

The Fermi-Dirac statistic describes the probability that an electronic state for a given energy E is occupied by an electron. The Fermi-Dirac statistic is symmetric around the Fermi energy E_F. The Fermi energy can be defined as the energy at which the Fermi-Dirac distribution is equal to ½. In general, the Fermi-Dirac statistic is strongly temperature dependent (Figure 2.16). With decreasing temperature the transition gets "sharper". It means that in practical terms an electronic state is very likely to be occupied by an electron if the energy of the electron is a few kT (or $K_B T$) higher than the Fermi energy. Consequently it is very unlikely that an electronic state is occupied by an electron if the energy is a few kT (or $K_B T$) below the Fermi energy.

With increasing donor concentration the Fermi level will shift closer to the bottom of the conduction band. Therefore, the energy difference between the Fermi level and the conduction band (E_C-E_F) gets smaller with increasing donor concentration.

An analogous behaviour is observed for increasing acceptor concentration. The higher the acceptor concentration the closer the Fermi level will move to the valence band. Figure 2.17 gives more illustration about these phenomena.

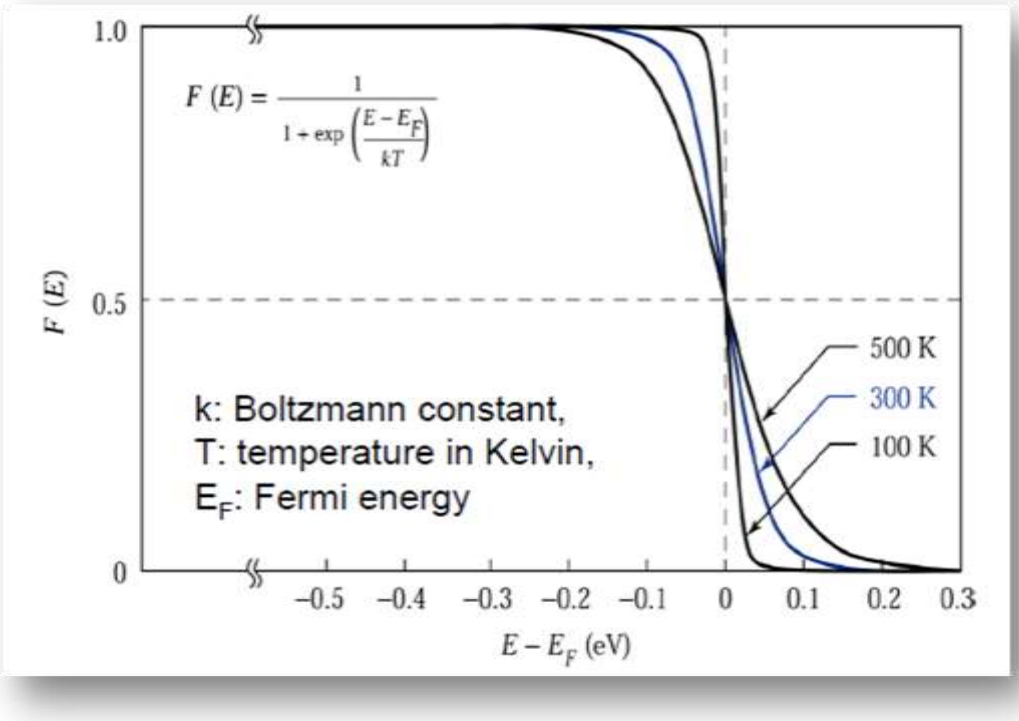

Figure 2.16: Schematic diagrams of the distribution function [42]

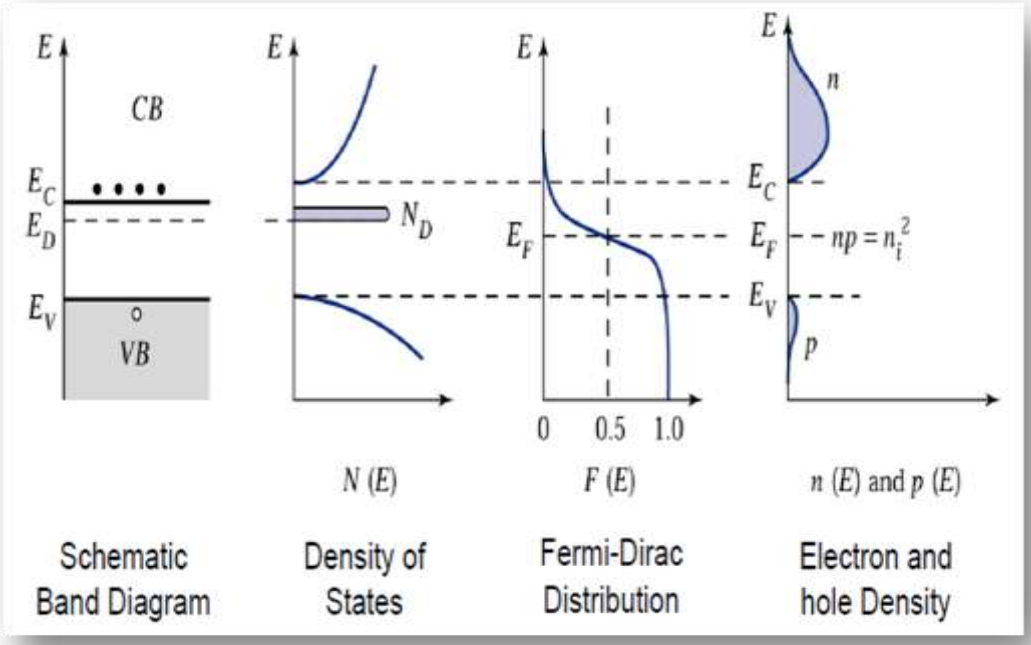

Figure 2.17: Schematic diagrams of semiconductor energy bands [42]

2.5.11. Solar cells characterisation

Solar cells are characterized by many factors including among others efficiencies, I-V characterisation, light absorption and predominantly the semiconductor equations.

2.5.11.1. Semiconductors equations

The operation of most semiconductor devices, including solar cells, can be described by the so-called semiconductor device equations, first derived by *Van Roosbroeck* in 1950 [43]. A generalized form of these equations is given here:

$$\nabla . \varepsilon \vec{E} = q(p - n + N) \quad \textbf{[2.46]}$$

This is a form of Poisson's equation, where N is the net charge due to dopants and other trapped charges. The hole and electron continuity equations are:

$$\nabla . \vec{J}_p = q\left(G - R_p - \frac{\partial p}{\partial t}\right) \quad \text{and} \quad \nabla . \vec{J}_n = q(R_n - G - \frac{\partial n}{\partial t}) \quad \textbf{[2.47]}$$

where G is the optical generation rate of electron–hole pairs. Thermal generation is included in R_p and R_n. The hole and electron current densities are given by

$$\vec{J}_p = -q\mu_p p \nabla(\emptyset - \emptyset_p) - K_B T \mu_p \nabla p \quad \text{and}$$
$$\vec{J}_n = -q\mu_n n \nabla(\emptyset + \emptyset_n) + K_B T \mu_n \nabla n \quad \textbf{[2.48]}$$

Two new terms, $\emptyset_p$ and $\emptyset_n$, have been introduced here. These are the so-called band parameters that account for degeneracy and a spatially varying band gap and electron affinity [44]. These terms were ignored in the preceding discussion and can usually be ignored in nondegenerate homostructure solar cells.

The intent here is to derive an analytic expression for the current-voltage characteristic of a simple solar cell, and so some simplifications are in order. It should be noted, however, that a complete description of the operation of solar cells can be obtained by solving the complete set of coupled partial differential equations, equations (2.47) through (2.48).

2.5.11.2. Light absorption

PV power conversion is strongly dependent on the quantum nature of light. Light in this regard is perceived as a flux of particles-photons which carry energy [10]. And this is given by the relation:

$$E_{ph}(\lambda) = \frac{hc}{\lambda} \quad \textbf{[2.49]}$$

where h is the Planck constant, c is the celerity (speed of light), and λ is the wavelength of light.

It is observed that on a clear day, every second, almost 4.4×10^{17} photons strike a square centimetre of the Earth's surface. Only some of these photons (those with energy in excess of the band gap) can be converted into electricity by the solar cell. When such a photon strikes and enters the semiconductor, it may be absorbed and excites an electron from the valence to the conduction band (Figure 2.18). A hole is left behind in the valence band, thus, the absorption process creates electron-hole pairs.

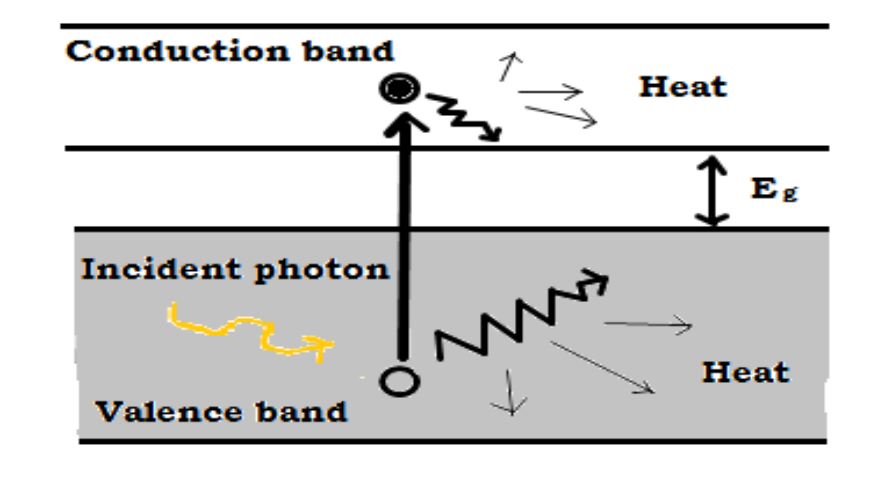

Figure 2.18: The generation of electron-hole pairs by light [10]

Each semiconductor is, therefore, restricted to converting only a part of the solar spectrum (Figure 2.19). Using equation (2.49), the spectrum has been plotted here in terms of the incident photon flux as a function of photon energy. The shaded area is

the photon flux that can be converted by silicon cell and that is about two thirds of the total flux.

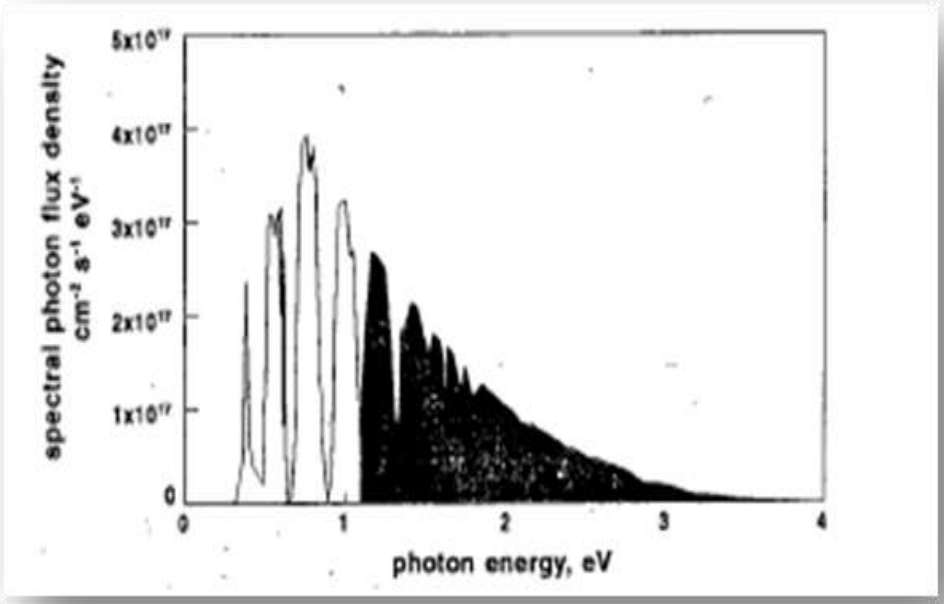

Figure 2.19: Photon flux utilised by a silicon solar cell [10]

The understanding of the nature of the absorption process also reveals how a part of the incident photon energy is lost. Indeed, it is observed that almost all the generated electron-hole pairs have energy in excess of the bandgap.

Just after their creation, the electron and hole decay with the excess energy lost as heat and cannot be converted into useful power. This represents one of the fundamental loss mechanisms in a solar cell.

2.5.11.3. Other Characteristics of Solar Cells

As in indicated section 2.5.7., the operation of a solar cell is analogous to a semiconductor ***p-n*** junction, normally without an external bias. This bias provides an electrical power to a load when illuminated.

PV cells can be modelled as a current source in parallel with a diode (this is discussed in detail in section 2.12). With no light, PV cells behave like a diode. As the incident

light intensity increases, current is generated by the cell as shown in Figure 2.20 below. In an ideal cell, the sum of the photoelectric effect generated current I_L and the negative of the diode current I_D gives the total current I. This is mathematically represented by [38]:

$$I = I_L - I_D \qquad [2.50]$$

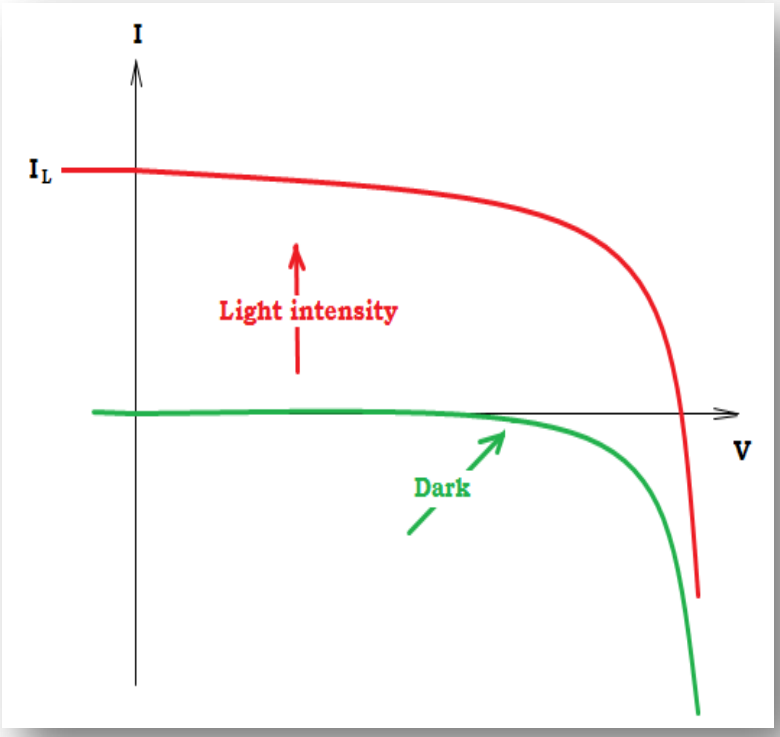

Figure 2.20: I-V characteristics of a PV solar cell under no light and with light

But recalling equation (2.15) and substituting it into equation (2.50) yields:

$$I = I_L - I_0[\exp\left(\frac{qV}{K_BT}\right) - 1] \qquad [2.51]$$

where I_0 is the saturation current.

Since a high load resistor reduces the current flux, the charges need more time to get out of the semiconductor. This would mean that recombination could take place increasingly and the extracted external current decreases. This can be observed in the fourth quadrant of the next I-V curve below.

It is clear from the plot (Figure 2.21) that the voltage is dependent on the I-V curve. The maximum power is the maximum product of I and V that can be found the fourth

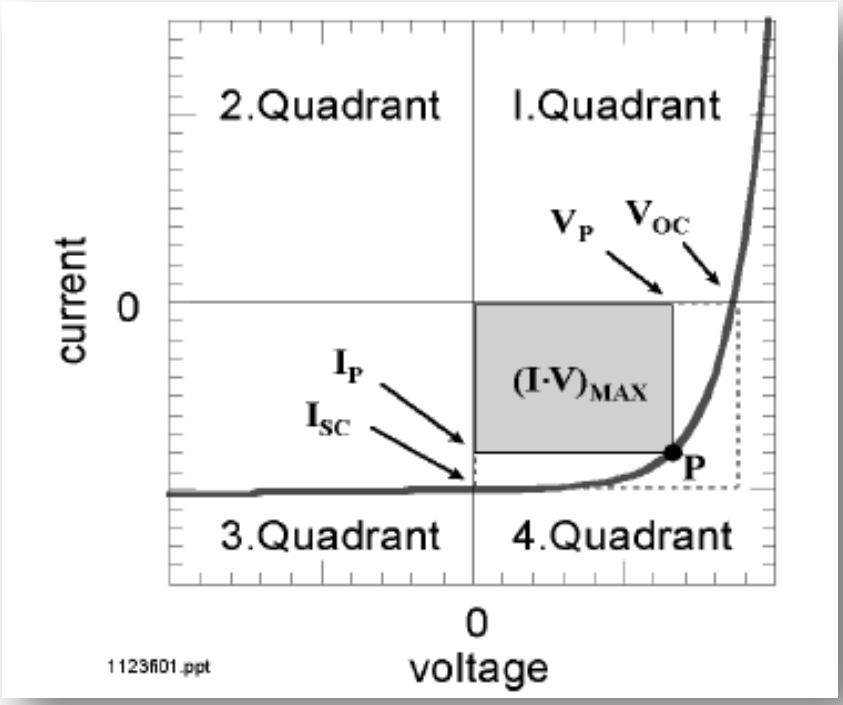

Figure 2.21: I-V characteristics of a PV solar showing all four quadrants [38]

quadrant of figure 2.20. The more the I-V curve resembles the rectangle with area $I_{SC} \times V_{OC}$, the larger the maximum area [38].

The measure of the quality of the shape of the I-V characteristics is known as the field factor (FF) and is the ratio between these above mentioned two areas:

$$\boldsymbol{FF = \frac{(IV)_{max}}{I_{SC}V_{OC}}} \qquad \textbf{[2.52]}$$

Thus the maximum power P_{max} is given by:

$$\boldsymbol{P_{max} = (IV)_{max} = FF \times I_{SC}V_{OC}} \qquad \textbf{[2.53]}$$

Another important parameter is the conversion efficiency (η). In order to express the power conversion efficiency (η) of a solar cell, the maximum output power P_{max} must

be related to the power of the incident light P_{in}:

$$\eta = \frac{P_{max}}{P_{in}} \quad \textbf{[2.54]}$$

But knowing the value of P_{max} from equation (2.53), equation (2.54) can now be written as:

$$\eta = \frac{FF \times I_{SC} V_{OC}}{P_{in}} \quad \textbf{[2.55]}$$

In order to compare efficiencies of solar cells, solar radiation standards have been defined in the past. The most common standard at present days is the AM1.5 spectrum which can be achieved by commercial solar simulators [38].

2.6. Need for organic photovoltaic solar cell

In recent years, there has been increasing interest in the use of photovoltaics as alternative energy source to replace environmentally-polluting fossil energy sources [45]. There has also been an interest in developing lower cost alternatives to existing silicon-based solar cells [45], especially in the parts of the world where people earn less than $ 1-2 per day.

Organic photovoltaic materials represent one of the possible solutions to low cost solar cells and light emitting devices [45]. Since they have lower melting points than silicon, they can be processed at much lower costs, and integrated into PV devices for energy and lighting.

However their low energy conversion still remains a shortcoming of organic photovoltaic solar cells. Figure 2.22 and 2.23 present efficiency data for thin film solar cells for durations between 2033 and 2010. It is also clear that the efficiencies of OPVs have increased continually during this period.

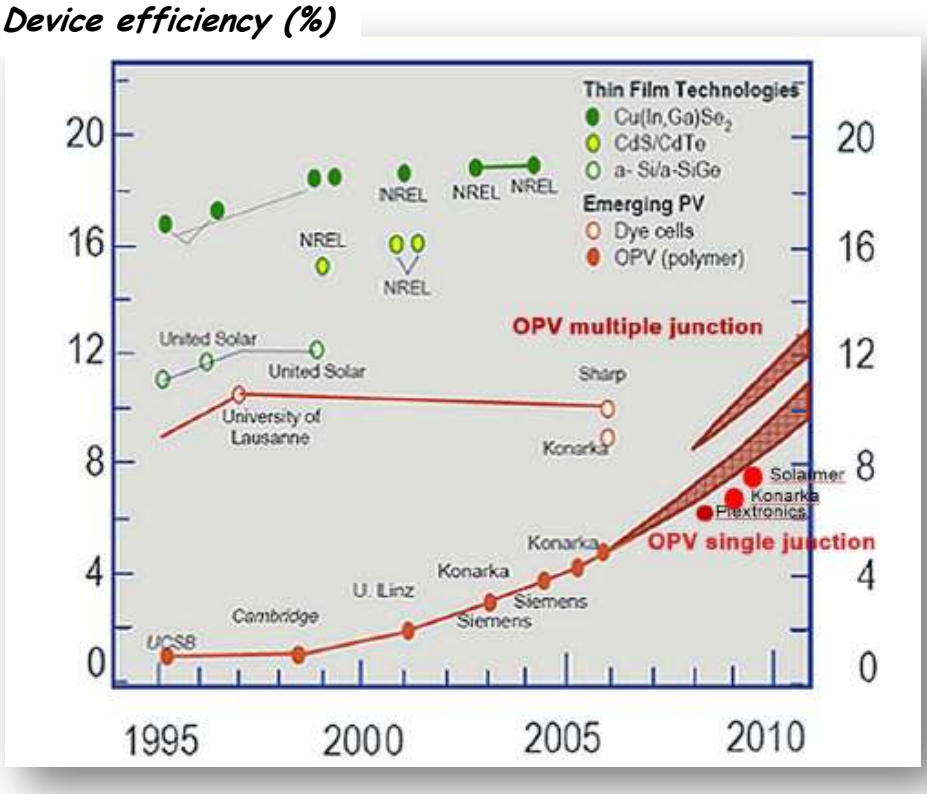

Figure 2.22: Best Cell Efficiency of Thin Film Solar Cell over the years [45]

- 2003 – P3HT:PCBM(1:4), η=0.2%, not annealing
  J.C. Hummelen *et al*, *Synthetic Metal*, **2003**, *138*, 299
- 2003 – P3HT:PCBM (1:1), η=3.5%, 75°C for 4min annealing
  F. Padingger *et al*, *Adv. Funct. Mater.*, **2003**, *13*, 85
- 2004 – P3HT:PCBM (1:1), η=5%, Christoph J. Brabec (SIEMENS)
- 2005 – P3HT:PCBM (1:0.6), h=5.2%, 155°C for 3min annealing
  Marisol Reyes-Reyes *et al*, *Org. Lett.*, **2005**, *7*, 5749
- 2005 – P3HT:PCBM (1:0.8), η=4.9%, 155°C for 5min annealing
  K. Kim *et al*, *App. Phys. Lett.*, **2005**, *87*, *083506*
- 2006 – P3HT:PCBM (1:1), η=4.4%, 140°C for 120min annealing
  Y. Kim *et al*, *Nature Mater.*, **2006**, *5*, 197
- 2006 – P3HT:PCBM (1:1), η=5%, Ca-Ag electrode/xylene solution casting
  P. Schilinsky *et al*, *Adv. Funct. Mater.*, **2006**, *16*, 1669
- 2006 – P3HT:PCBM (1:0.8), η=5%, TiOx optical spacer
  K. Lee *et al*, *Adv. Mater.*, **2006**, *18*, 572
- 2007 – PCPDTBT:$PC_{71}BM$ (1:2), η=5.5%, dithiol treatment
  G.C. Bazan *et al*, *Nature Mater.*, **2007**, *6*, 1
- 2007 – P3HT:PCBM (1:0.8)/PCPDTBT:PC71BM, η>6%, TiOx optical spacer, Tandem
  K. Lee *et al*, *Science*, **2007**, *317*, 222
- 2008 – P3HT:New Acceptor, η>5.98%, Plextronics
- 2008 – New Low bandgap donors, η>6.23%, Konarka
- 2009 – New Low bandgap donor, η>6%, K.Lee, Y.Yang, Y. Lian etc.
- 2009 – New Low bandgap donor, η~7.9%, Solarmer

Table 2.23: Efficiency Improvement Status of Organic solar cell Unit Device (KRICT, 2009)

The organic photovoltaic solar cells are very promising. Despite their modest efficiencies as shown in Figure 2.23, their efficiencies have improved steadily over the past decade. They are also relatively inexpensive compared to silicon-based solar cells, and they have the potential for applications in flexible electronic structures. Figure 2.24 shows the details.

The objective of this research is to develop a fundamental understanding of the performance of BHJ solar cells. First the structure of organic BHJ solar cell is presented in this chapter before describing the analytical modeling and simulation of adhesion and contact.

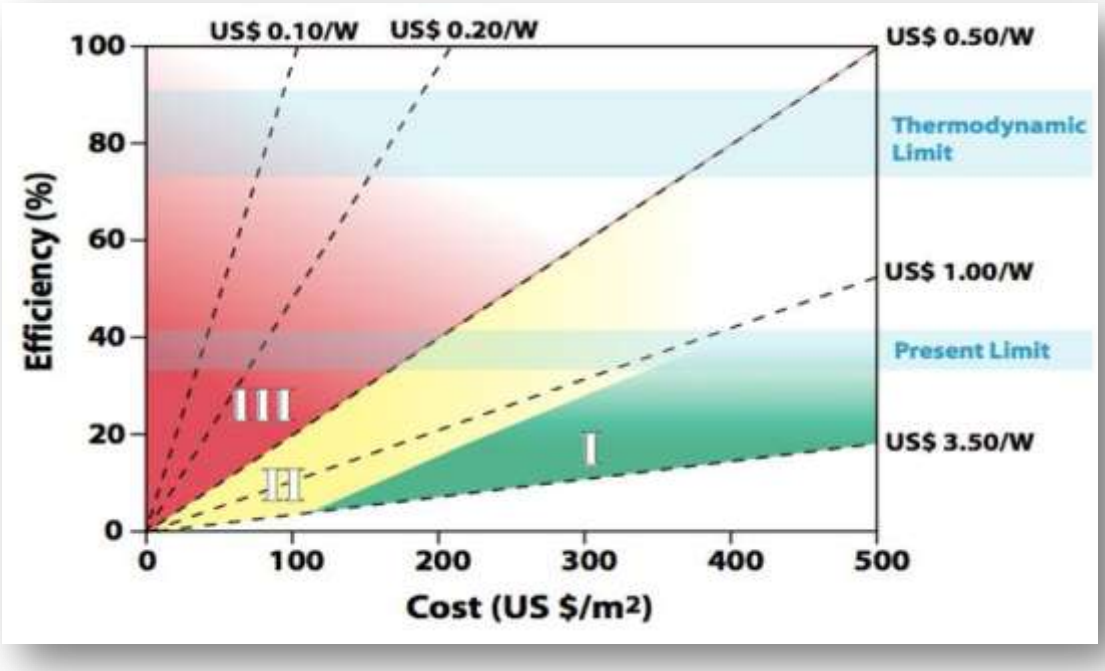

Figure 2.24: **Cost – efficiencies – limit of organic solar cells.** **[Adapted from NREL]**

2.7. Bulk Heterojunctions

The structure of bulk heterojunction (BHJ) solar cell is illustrated schematically in Figures 2.25a and 2.25b. These show the typical layered structure of the BHJ cell, consisting of donor and acceptor layers that are wedged between aluminum (Al) cathode and an indium tin oxide (ITO) anode.

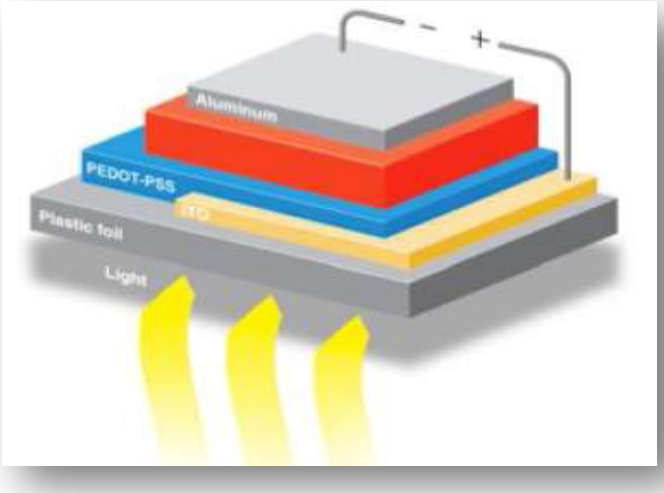

Figure 2.25: **(a) Schematic of an organic photovoltaic solar cell: Bulk Heterojunction solar cell.** **[Adapted from NREL]**

In Figure 2.25b, the n-type layer is an electron enriched material (could be through doping) while the p-type layer is a hole enriched material. These two layers form the active layer which is also known as the donor-acceptor layer.

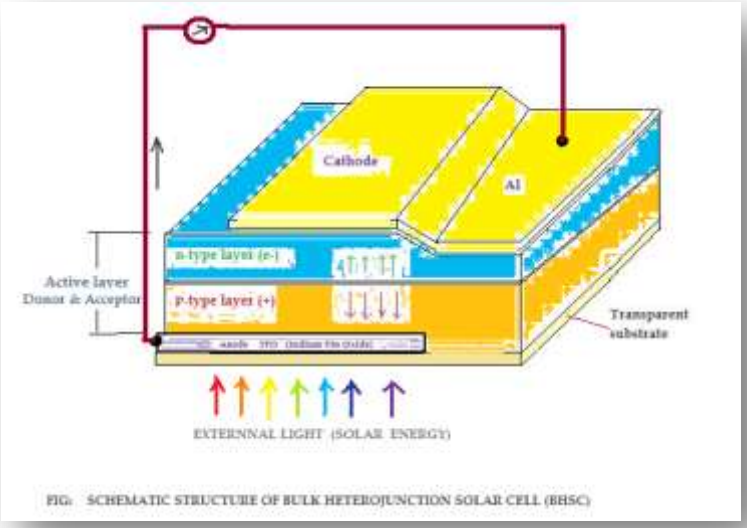

Figure 2.25: (b) Sketch like diagram of an organic photovoltaic solar cell showing details: Bulk Heterojunction solar cell

2.8. Description of the structure of the organic photovoltaic system

A typical organic photovoltaic (OPV) solar cell is shown schematically in Figure 2.26. The electron transmission layer (ETL) and the hole transmission layer (HTL) enclose the active layer which is typically fabricated from a conducting polymer such as P3HT (Poly (3-Hexylthiophene)) and a fullerene structure such as PCBM (Phenyl C61 Butyric Acid Methyl Ester).

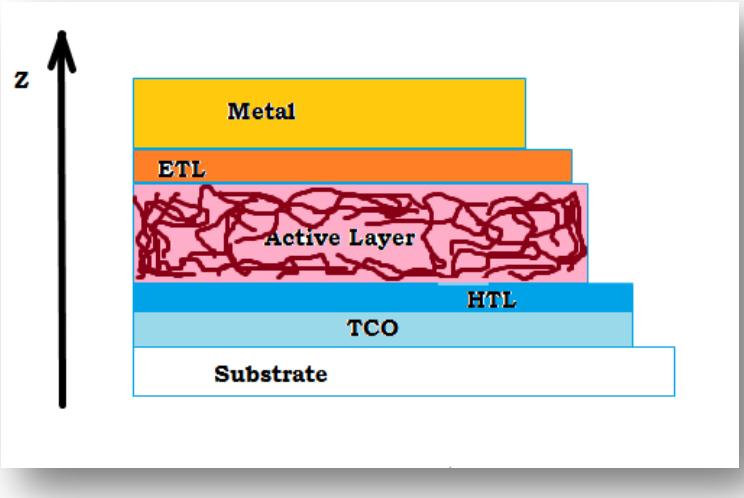

Figure 2.26: 1-D OPV structure showing various layers of the system. [Adapted from NREL]

The OPV device architecture can be classified into two: the standard devices and the inverted polarity devices.

The standard devices as shown in the energy-layer diagram below must be fabricated under an inert atmosphere condition. They employ low work function back contacts and are susceptible to oxidation.

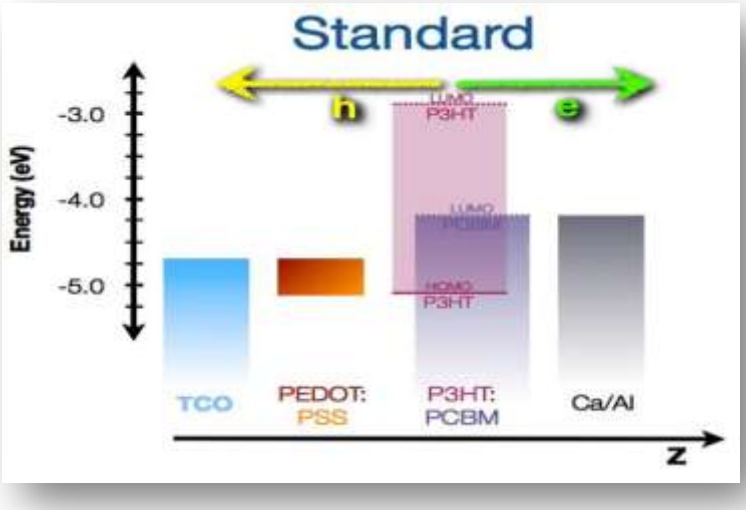

Figure 2.27: Standard OPV structure showing electron (e) and hole (h) directions within layers. [Adapted from NREL]

The inverted polarity device also shown in an energy-layer diagram in Figure 2.28 can be fabricated in air. It also makes use of high work function back contacts. It consists of a transparent conducting oxide layer (TCO) followed by the active blend layer of P3HT and PCBM, sandwiched between a hole injection layer (PEDOT:PSS) and the cathode (often Aluminum).

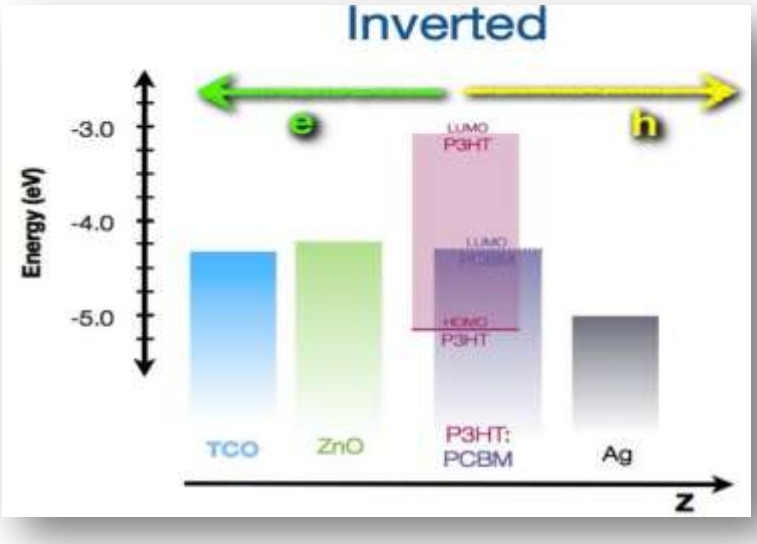

Figure 2.28: Inverted polarity OPV structure showing electron (e) and hole (h) directions within layers. [Adapted from NREL]

For the particular case of BHJ solar cell, the structure is presented in Figure 2.29. This consists of:

- Transparent substrate (mostly Glass) coated with
- ITO or other TCO's
- On which the Hole Transport Layer (HTL) is deposited
- Then the active layer mostly a blend of electron donors (D) and electrons acceptors (A) polymers
- Followed by Electron Transport Layer (ETL)

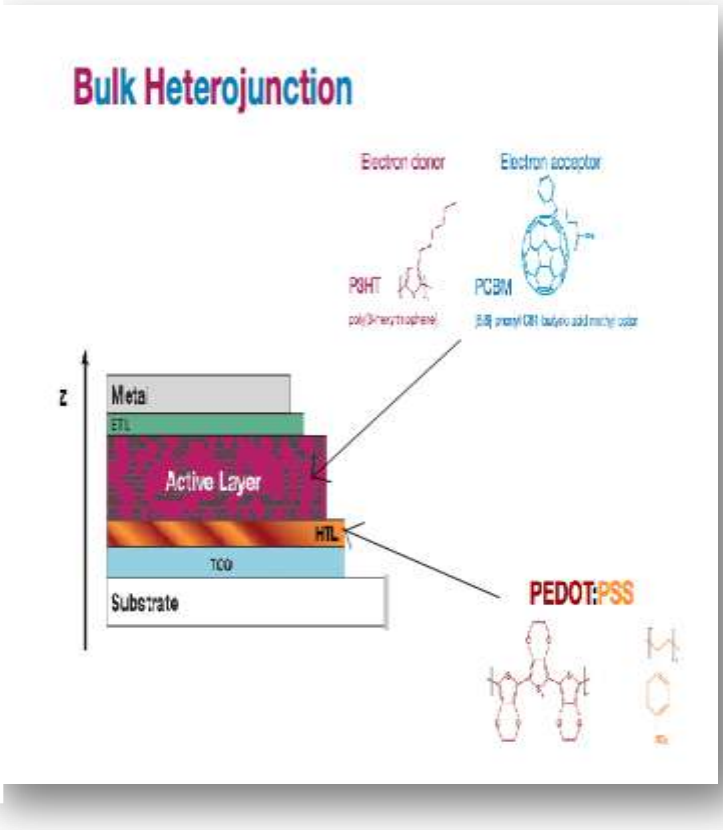

Figure 2.29: Bulk Heterojunction solar cell structure. **[Adapted from NREL]**

Different blends can be used in the active layer, two of the most commonly used are the P3HT: PCBM blend and the P3HT: ZnO blend shown in Figure 2.30.

Figure 2.30: Active layer polymer blends in Bulk Heterojunction solar cell structure. **[Adapted from NREL]**

2.9. Types of junctions in organic cells (BHJ solar cells)

2.9.1. Single layer OPV

In its simplest form, an organic solar cell is made up of a single layer sandwiched between two (2). The single layer sandwich was made, defining the first generation of organic photovoltaic solar cells. Their first power conversion efficiencies were reported were up to 0.7 % [46, 47]. They have organic layers sandwiched between a metal-metal oxide and a metal electrode, thus enabling a Schottky-barrier effect (Metal-Insulator-Semiconductor **(MIS)** devices [48]). Their structure is illustrated in Figure 2.31 a:

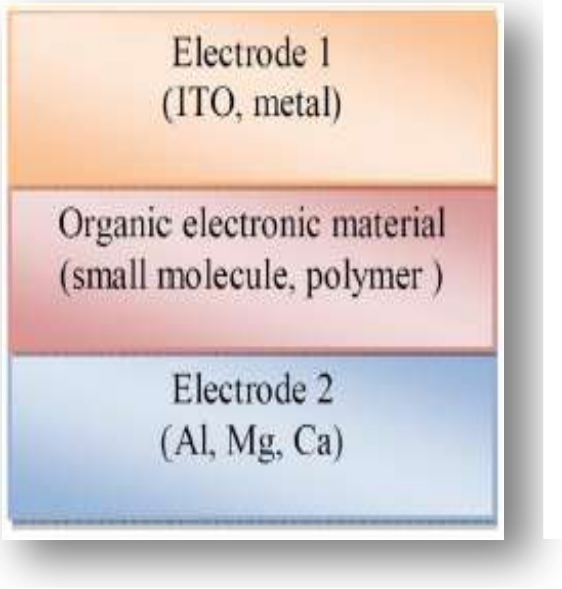

Figure 2.31: (a) Single layer OPV structure showing different main layers [50]

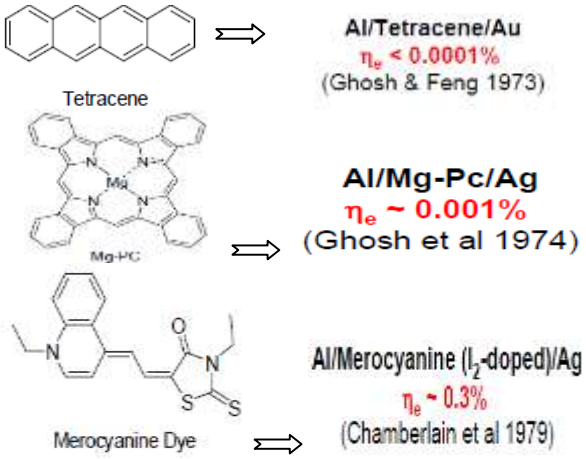

Figure 2.31: (b) Single layer OPV organic materials

Some of the small polymeric molecules, used include: Tetracene ($C_{18}H_{12}$), Magnesium phthalocyanine (Mg-PC) and Merocyanine dye. Indeed in 1973 Gosch and Feng had an efficiency of less than 0.0001 % for an arrangement of ***Al/Tetracene/Au*** for a single layer OPV. A year later Gosch et al. [49] obtained an efficiency of almost 0.001 % for ***Al/ Mg-PC /Ag***, but in 1979 Chamberlain et al. had an efficiency of almost 0.3 % for this arrangement: ***Al/ Merocyanine (I_2-doped)/Ag*** shown in Figure 2.31b. Most of the advances were made in the Shell Research Labs in late 1970s and early 1980s [49].

2.9.2. Double layer (Bilayer) OPV

From the work done on single layer OPV and the desire to improve upon efficiencies, Tang reported about 1 % power conversion efficiency in 1986. This was done for a stacked double layer consisting of two organic materials (a phthalocyanine derivative as p-type semiconductor and as a perylene derivative as n-type semiconductor) sandwiched between a transparent conducting oxide anode and a metal cathode **[50]**. The structure consisted of a donor layer and a subsequent acceptor layer, all organic materials. This was sandwiched between two (2) electrodes linking the donor HOMO and the acceptor LUMO, respectively. This enabled the efficient extracting of charge carriers, as shown schematically in Figures 2.32a and 2.32b.

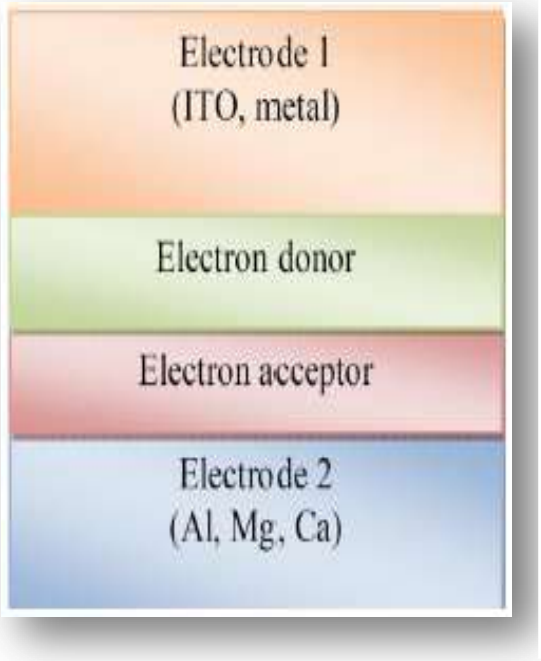

Figure 2.32: (a) Bilayer OPV structure showing different main layers [50]

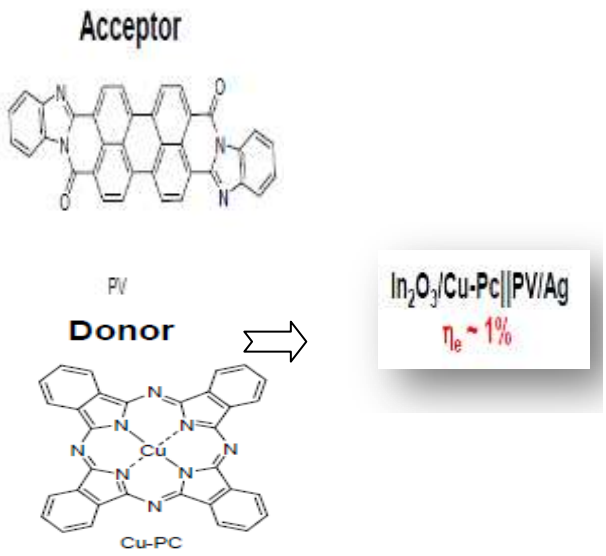

Figure 2.32: (b) Bilayer OPV organic materials [50]

This structure has an improved exciton dissociation at the donor/acceptor layers interface: electrons are transferred into acceptor layer (n-semiconductor), while holes are transferred into donor layer (p-semiconductor).

2.9.3. Bulk (Dispersed) Heterojunction OPV

We have seen from the previous section that in the D and A double layer structure, the dissociation takes place at the D/A interface. Also, the external quantum efficiency (EQE) can be increased with respect to the single layer architecture. In this section, we discuss another D/A device structure: blends i.e. mixtures of donor and acceptor materials.

The bulk heterojunction device is similar to the bilayer device with respect to the donor-acceptor concept (Figure 2.33). However, it results in a large increase in the interfacial area dispersed throughout the bulk [51].

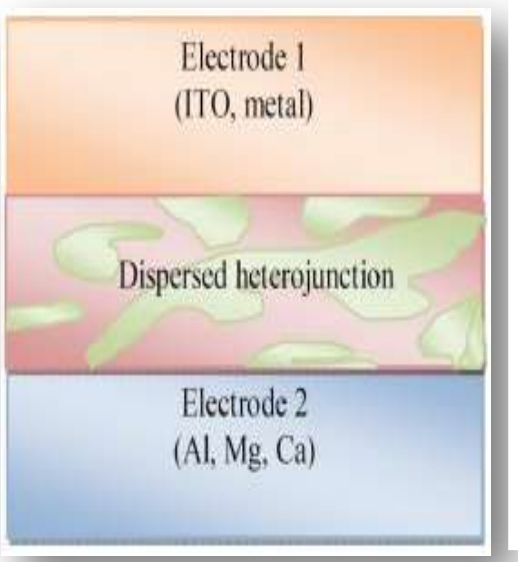

Figure 2.33: (a) Bulk heterojunction OPV structure showing different main layers [51]

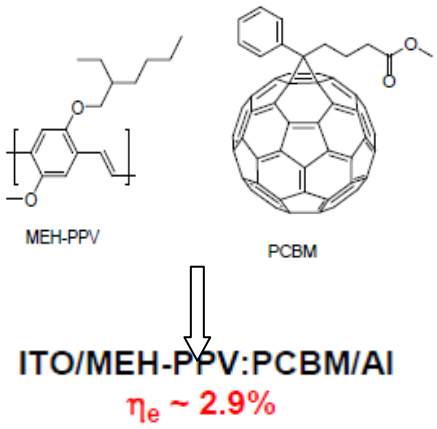

Figure 2.33: (b) Bulk heterojunction OPV organic materials [51]

The main advantage of the blend device is that the active layer is (can be) considerably thicker than the sum of the exciton diffusion lengths in the donor and acceptor material. This is true for blends that consist of a bicontinuous and interpenetrating network, with domains that are not larger than twice the exciton diffusion length. Therefore, the bulk heterojunction devices are much more sensitive to the complicated nanoscale morphology in the blend. An example of a more comprehensive diagram is shown below in Figure 2.34. This shows clearly a 3-D layer by layer schematics of the BHJ solar cell structure.

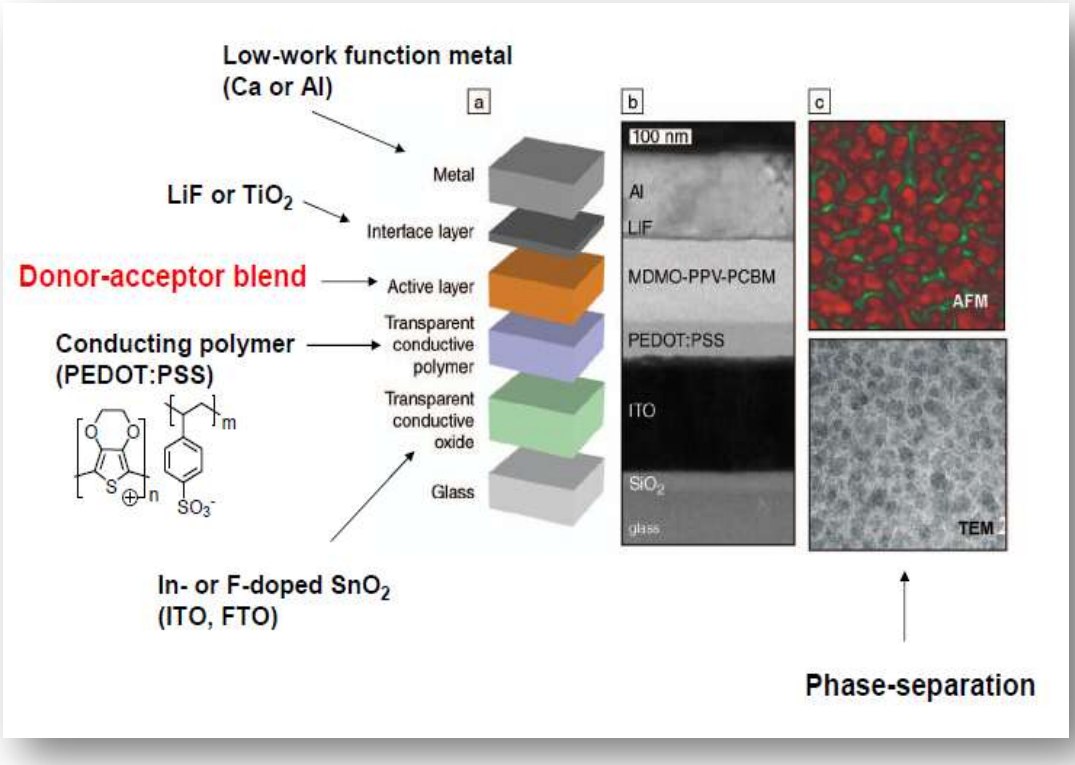

Figure 2.34: Bulk heterojunction OPV detailed structure showing the different layers [49]

In section 2.8, a structure like the figure above and two structures of the blends were shown. Here we show various materials employed to form the blends, first the donor materials then the acceptor materials.

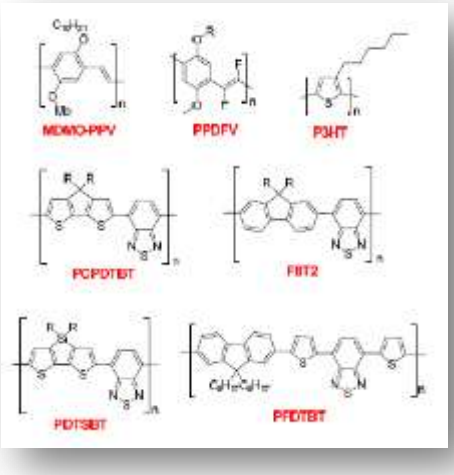

Figure 2.35: (a) Donor: p-type materials [45]

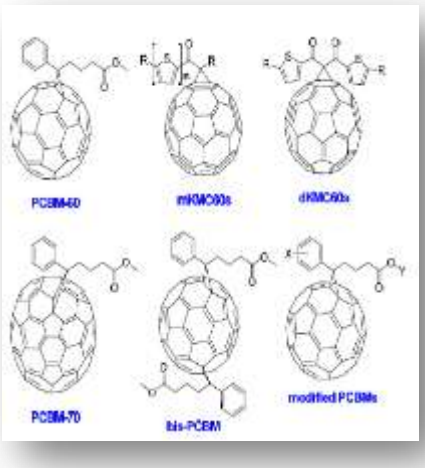

Figure 2.35: (b) Acceptor: n-type materials [45]

The steps involved in the creation and migration of excitons are described below in Figure 2.36.

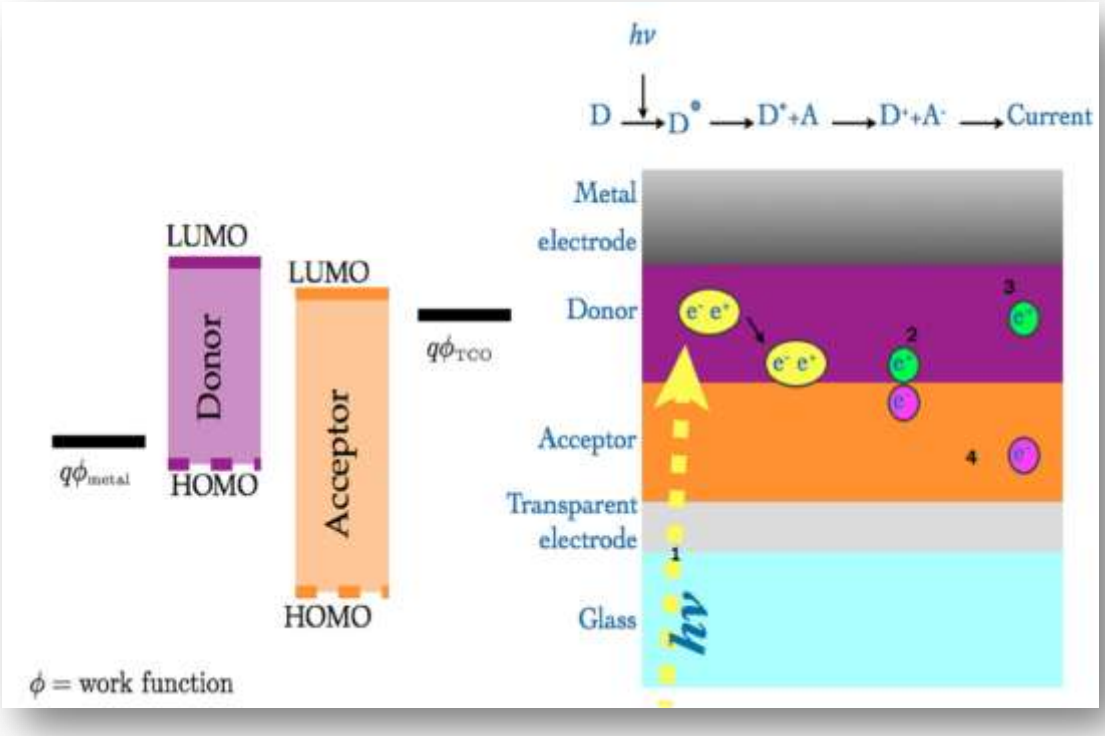

Figure 2.36: Mechanism in BHJ solar cell device's dispersive active layer. [Adapted from NREL]

LEGEND:

Exciton

Hole

Electron

Incident light

Steps of mechanism

1. The incident light creates excitons which begin to migrate in the system.
2. The holes move to the electrode above that is the metal electrode.
3. Electrons are trapped in isolated island of organic materials
4. Electrons move towards bottom electrode that is the transparent electrode.

It is important to note that exciton recombination can occur before the electron-hole pairs reach the electrodes. Hence, there is a need to enhance charge transport prior to recombination. This can be achieved through improved charge transport within the individual

layers, and improved contacts at interfaces. Improved contacts can be achieved through the use of lamination techniques [45], while improved charge transport within layers can be achieved through the selection and mixing of composite materials.

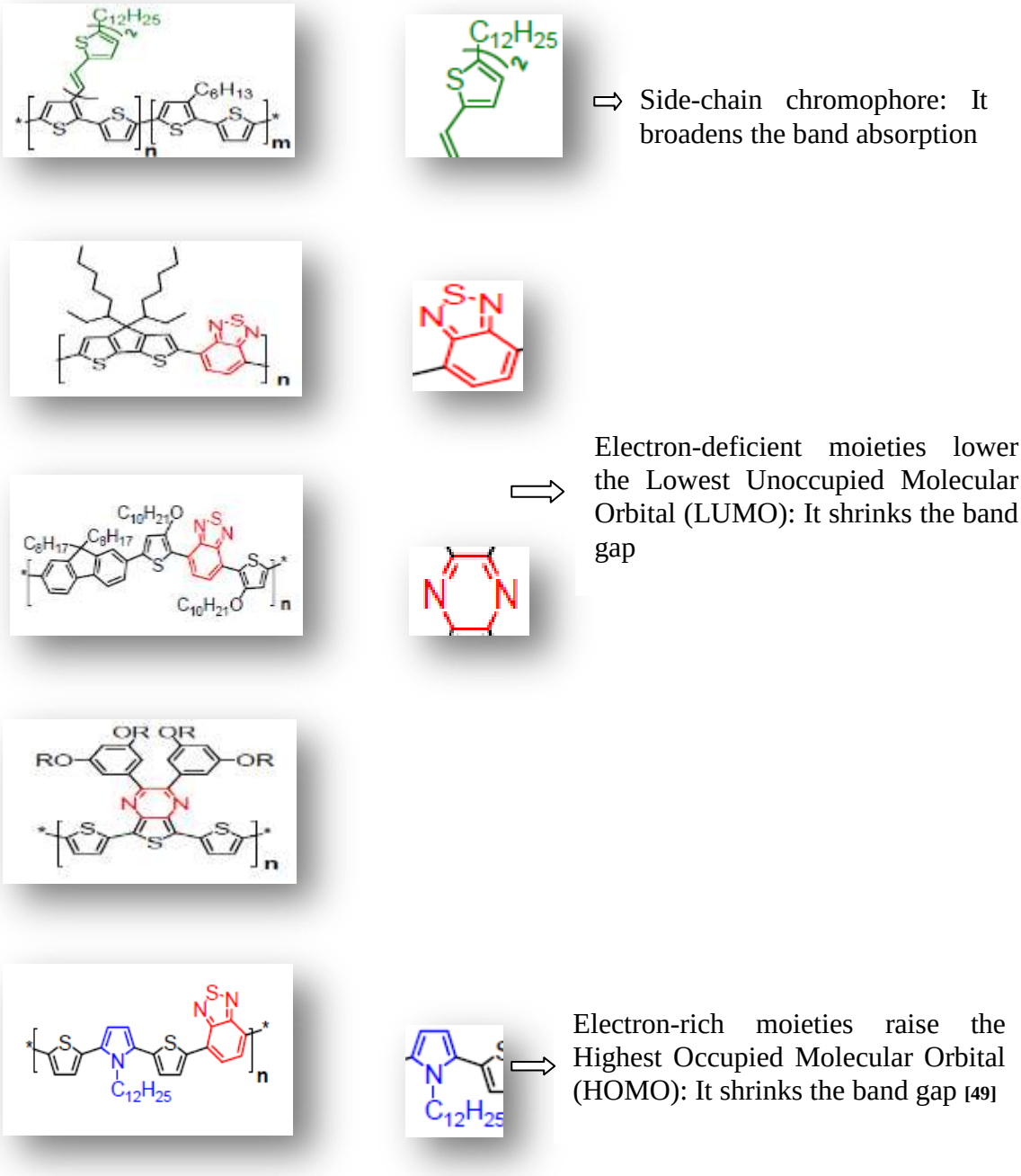

Figure 2.37: Composite materials for active layer blends

2.10. Fabrication of devices

Low cost organic photovoltaic have undergone intensive research for the past ten (10) years. Organic PV has a powerful potential to be a novel optoelectronic device using as renewable energy source, especially, due its promising low-cost manufacture by high volume production methods such as printing, painting and coating on flexible substrate [45].

For example by spin-coating technique, the energy conversion efficiencies of polymer-based bulk heterojunction solar cell poly-3-hexylthiophene (P3HT) as a donor and phenyl-C_{61}-butyric acid methyl ester (PCBM) as an acceptor shown in the Figure 2.38 below, have reached up to 4-5 % under 1.5 AM (10 $mW.cm^{-2}$) illumination [52, 53].

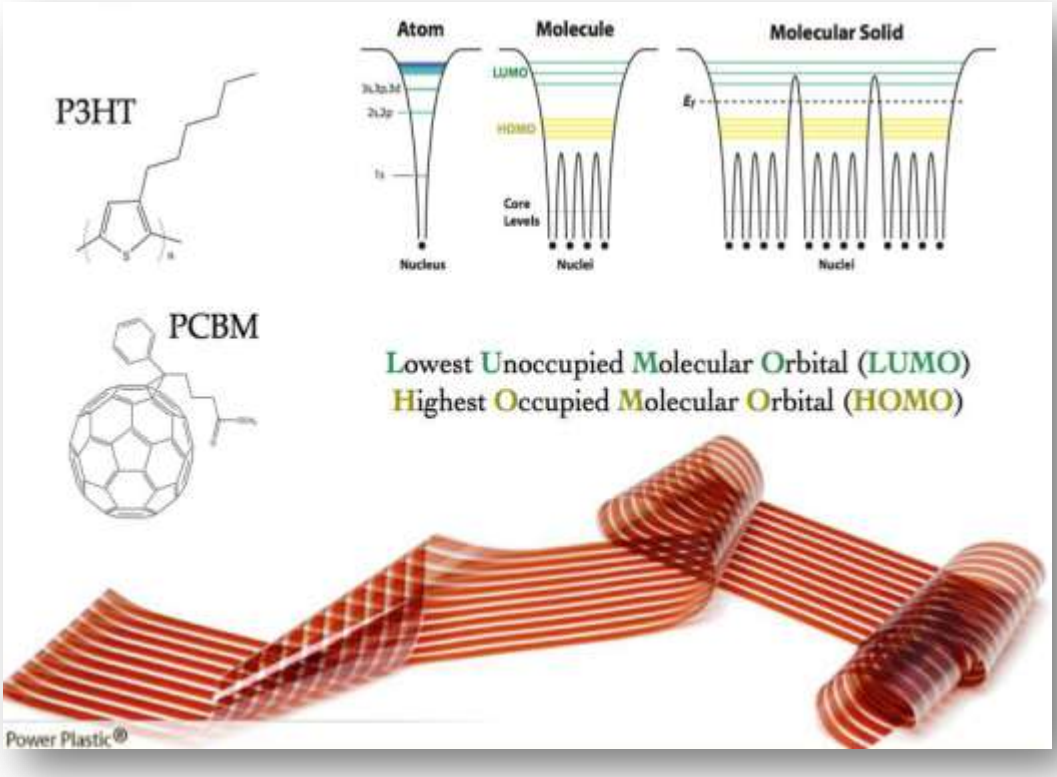

Figure 2.38: Chemical and molecular orbital structures of polymeric P3HT (D) and PCBM (A) [Adapted from Konarka Technology]

So far, several printing and coating methods have been used to process organic PV solar cells. These include: screen printing, pad (gravure offset) printing,

ink-jet printing, aerosol jet printing, spray printing, roll-to-roll (R2R) printing, micro-contacting printing, bush painting, doctor blading, knife-over-edge coating, slot-die coating, spin-coating, and spray coating [45].

This section presents a brief review of methods that are being explored for the fabrication of OPVs. Figure 2.39 shows the main steps in the processing of organic (bulk heterojunction) solar cells.

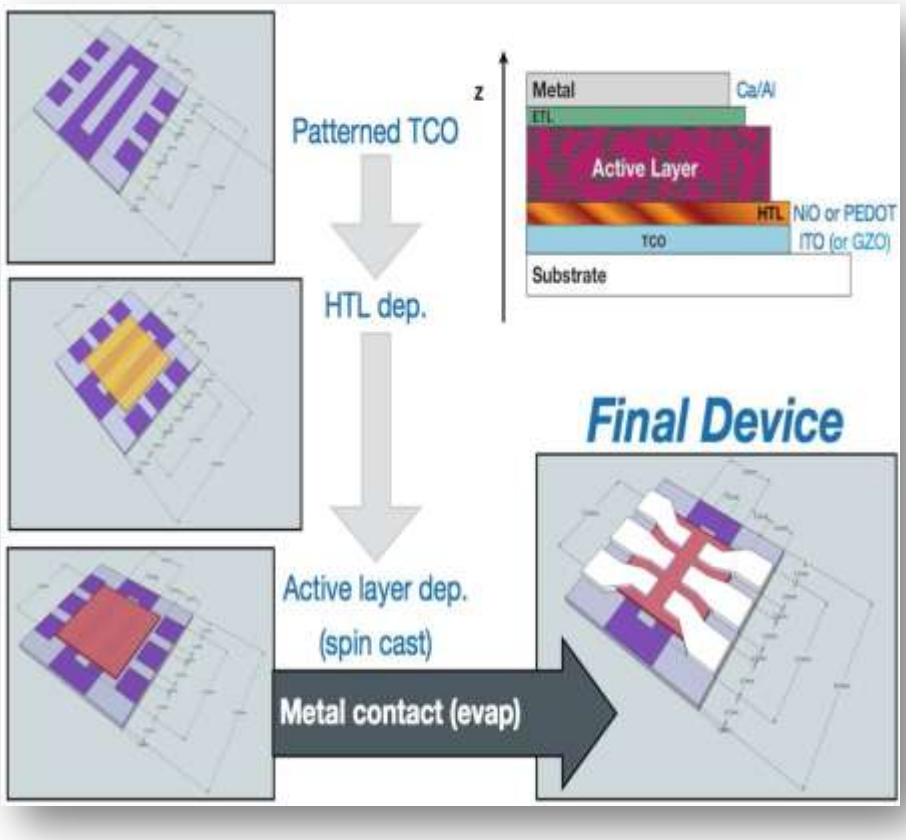

Figure 2.39: Steps in organic PV device preparation. [Adapted from NREL]

For mass production, an attractive solution from cost standpoint, R2R manufacturing methods are utilized to produce organic solar cells. The main benefit of organic solar cells produced with R2R manufacturing methods is that it requires less capital investment, in comparison to Si-based devices [54].

To achieve higher voltage, single organic solar cells can be prepared in series to form a module Figure 2.40. Also, to improve the reliability of a solar module [55], parallel connections can be used. The advantage of parallel connections is that when one cell fails, the module still works.

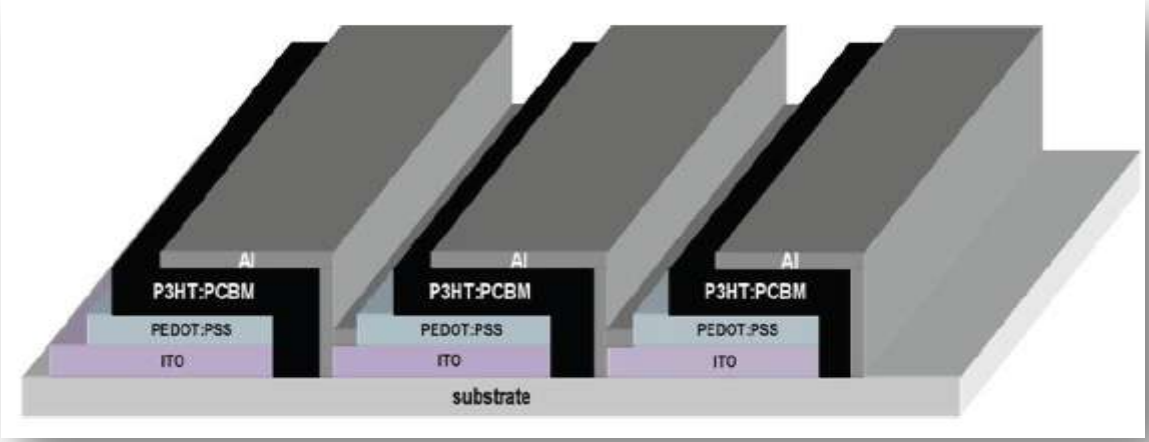

Figure 2.40: Series connection preparation of solar cells on one substrate [56]

The potential steps that are involved in the roll to roll (R2R) fabrication of organic solar cells are illustrated in Figure 2.41. This shows the various layers from substrate to the adhesives through cathode and their methods of deposition and other techniques.

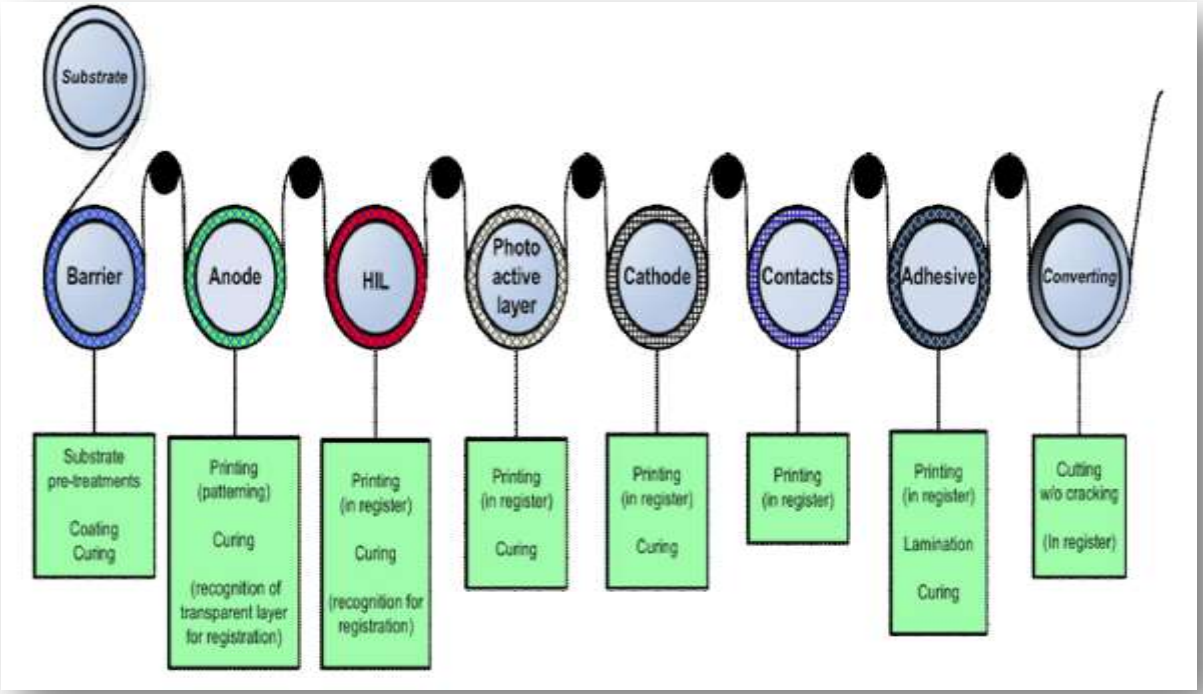

Figure 2.41: Process steps of organic PV component manufacturing [55]

2.11. Lamination

Lamination is the process of joining two layered materials together. It could be done through application of pressure, heat, a combination of both or through an adhesive layer. Laminated devices have comparable and in some cases, better performance than other devices made by other methods. This is because it helps to delay degradation of organic solar cells, while promoting improved contact lengths. It also helps to avoid the use of harmful chemicals and high intensity light sources. The uses of lamination include:

- Lamination of glass for use in windshields
- Encapsulation of devices

The organic PV has to be protected against oxygen and moisture in order to maximize and stabilize the organic solar cell lifetime. Upon exposure to these gases, the cathode and active materials can be easily destroyed or oxidized. Hence, backside encapsulation is done by applying some adhesive onto the organic PV solar cell and then laminating the organic solar cell with a plastic film containing a barrier layer. A tape-like film can also be used as barrier film. The adhesive attaches the organic solar cell to the barrier film. It also acts as a sealant. These adhesive deposition and lamination process are always done under inert conditions. The adhesive should also be solvent free, and fast-curing, and have low curing temperature, to avoid damage to the organic solar cells [57, 58].

In our study the pressure based lamination is employed. It is often done by rolling, such that uniform pressure is exerted on the sample surface, as shown in figure 2.42a below.

Many types of encapsulant resins have been examined up for use in PV modules. When PV panels were first developed in the 1960s and 1970s, the dominant encapsulants were based on poly-di-methyl-siloxane (PDMS) [59, 60]. This was chosen because of its exceptional natural stability against thermal- and ultraviolet light-induced stress. In today's organic PV cells, PDMS is often chosen above Epotek for use in packaging by encapsulation / lamination. A laminated structure of BHJ organic solar cells is shown in Figure 2.42b. The PDMS is a flexible and chemical-resistant barrier that limits the penetration of oxygen and water vapor. Hence,

lamination / encapsulation with PDMS package can protect organic solar cells and light emitting devices from oxygen and water vapour.

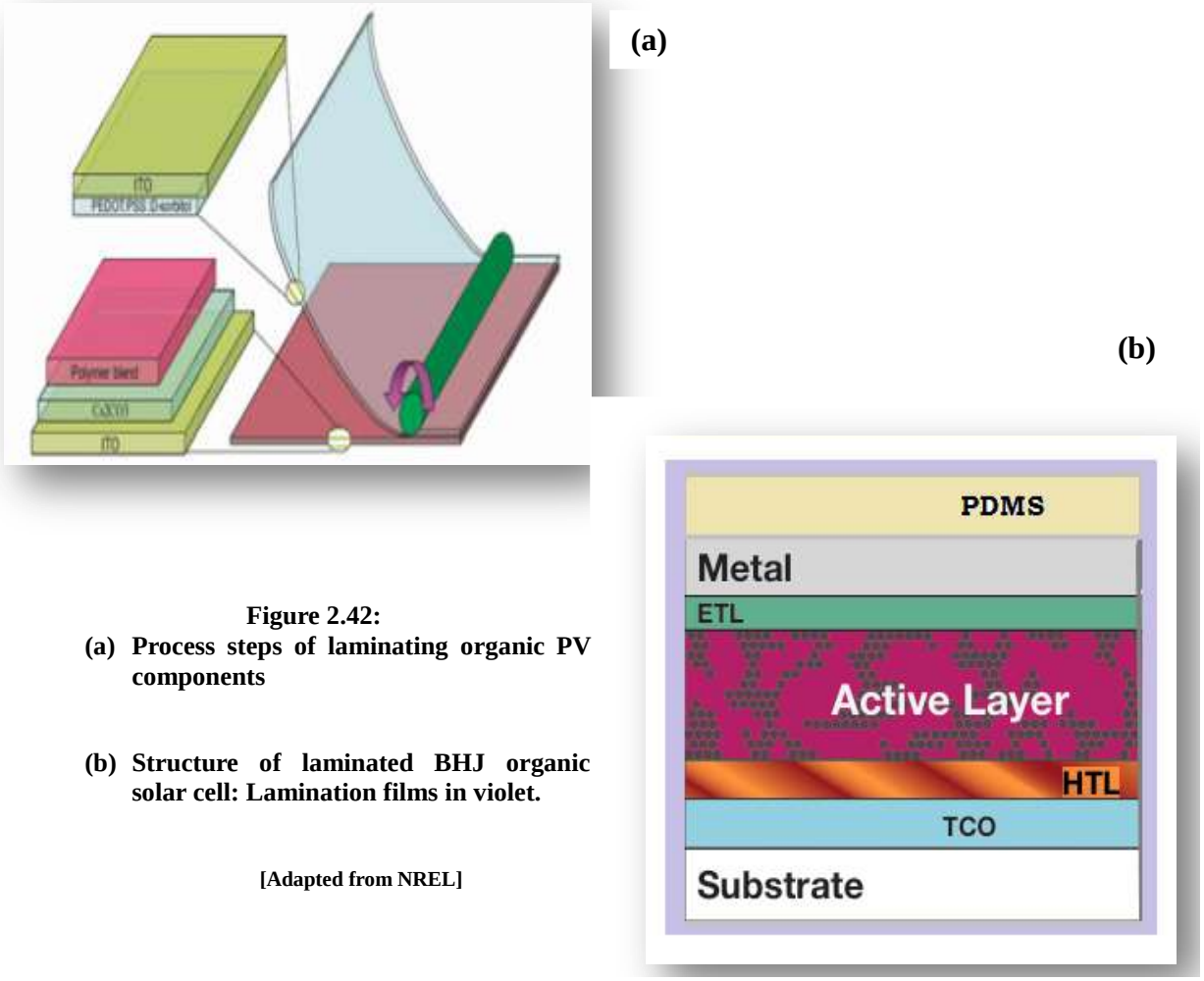

Figure 2.42:
(a) Process steps of laminating organic PV components

(b) Structure of laminated BHJ organic solar cell: Lamination films in violet.

[Adapted from NREL]

2.12. Modeling of organic PV

Diodes based circuits have been used in the modeling organic photovoltaic solar cell. These include: the single diode-model and the two-diode model that are described in this section for the purposes of this thesis work and the time frame.

- **Single-diode model:**

Below is the I-V characteristic curve for a solar cell in the dark (blue curve) and in the presence of light (red and green curves).

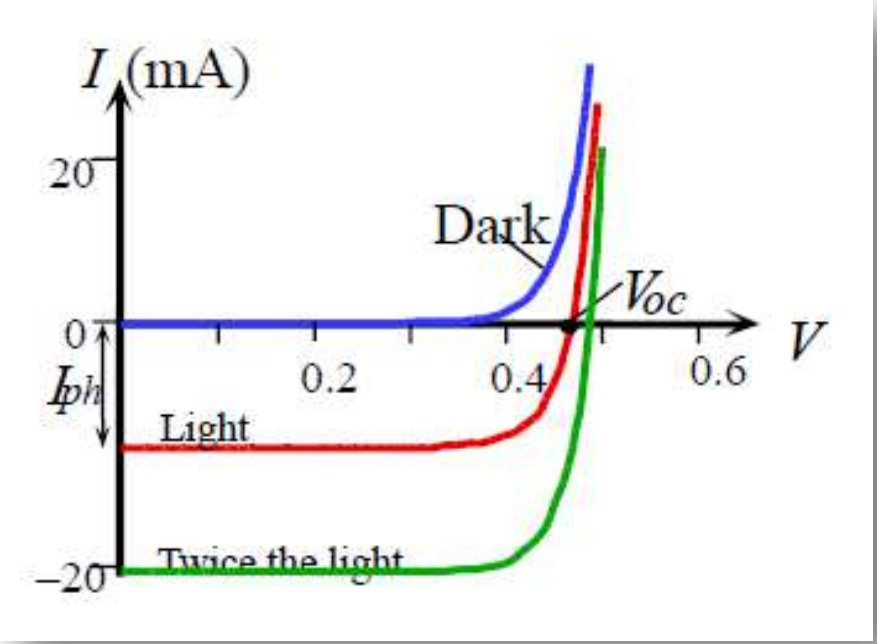

Figure 2.43: I-V characteristics load lines

Under illumination (in the presence of light), the solar cell (organic) can be represented with a simplified equivalent circuit, based on a single-diode model. This is shown in the Figure 2.44. This circuit is described as a current source in parallel with junction as portrayed in equation [61]:

$$\boldsymbol{I\left(1+\frac{R_s}{R_{sh}}\right)-\frac{V}{R_{sh}}+I_L=I_s(\exp(\frac{e}{nkT}(V-IR_s)-1)} \qquad \textbf{[3.1]}$$

Where $\boldsymbol{R_s}$ and $\boldsymbol{R_{sh}}$ are the respective series resistance and shunt resistance; $\boldsymbol{I_L}$ originates from the charge generated by illumination; $\boldsymbol{I_s}$ is the saturation current under reverse bias; $\boldsymbol{R_L}$ is the external circuit resistance; $\boldsymbol{n}$ is the ideality factor.

For a given PV solar cell series resistance depends on the resistivities of the semiconductor bulk, the metal/semiconductor interface and the metal electrodes. Similarly, the series resistance depends on the resistivities of the organic materials, the metal/organic interface and the metal electrodes, in an organic solar cell [61].

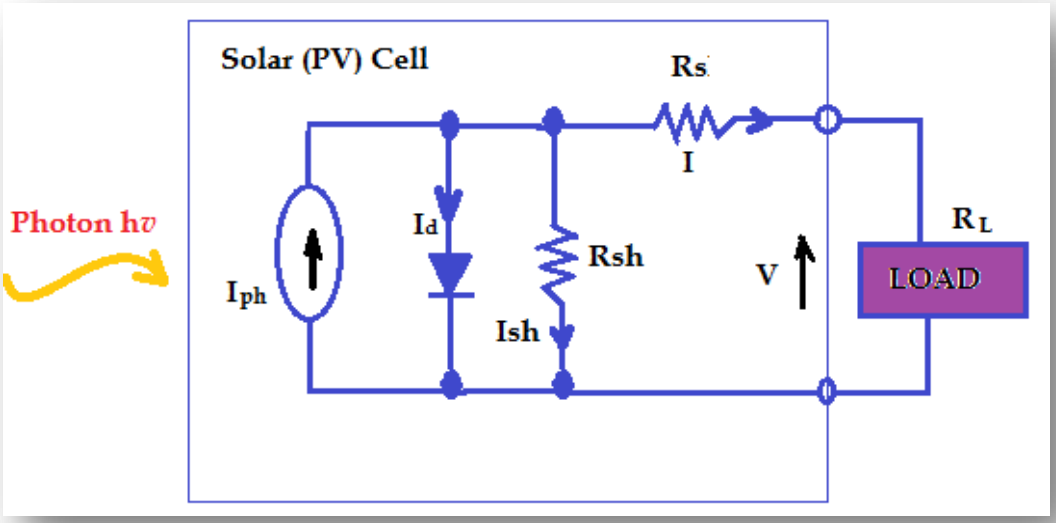

Figure 2.44: Equivalent circuit for a real PV solar cell under illumination (Single-diode model)

The series and shunt resistances are linked by the equation below:

$$I_{sc} = I_L - \frac{R_s I_{sc}}{R_{sh}} \quad [3.2]$$

Building on this approach, Jain and Kapoor, in order to modelize an organic solar cell, reported a new single-diode based approach using Lambert W-function [62]. The model is presented in the Figure 2.45 below:

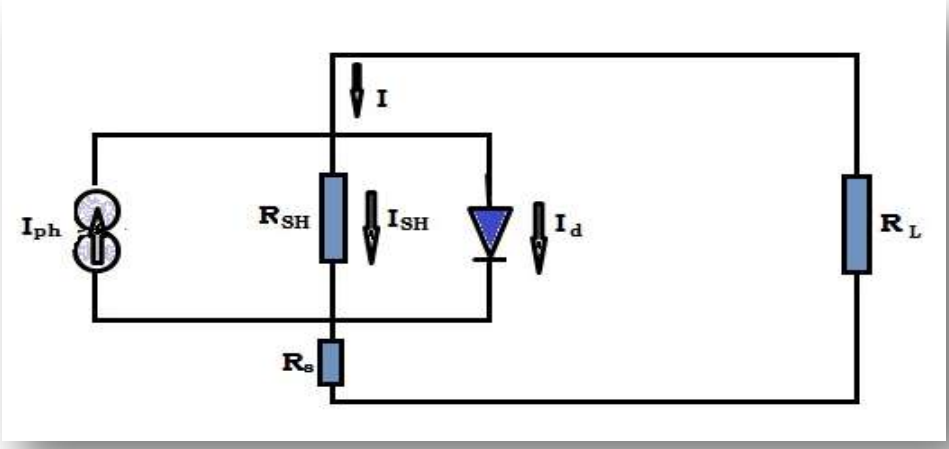

Figure 2.45: Equivalent circuit for an organic PV solar cell (Lambert W-function approach) [62]

- **Two-diode model:**

A new simplified equivalent circuit of a two diode model solar cell is presented in Figure 2.46. This may be described by the lumped parameter equivalent circuit [63]. For this kind of arrangement and for a given incident light intensity, the implicit I-V characteristic relationship, at a given temperature, is given by [63]:

$$\boldsymbol{I = I_{ph} - \frac{V+IR_S}{R_{SH}} - I_{01}[\exp\{B_1(V+IR_s)\} - 1] - I_{02}[\exp\{B_2(V+IR_s)\} - 1]} \quad \textbf{[3.3]}$$

Where $B_1 = {}^{q}/_{K_B T}$ and $B_2 = {}^{B_1}/_{n}$; I_{ph} is the photocurrent; K_B is the Boltzmann's constant; q is the electronic charge; T is the temperature; R_s is the series resistance; R_{SH} is the Shunt resistance and n is the ideality factor.

I_{01} represents the electronic conduction phenomena in the quasi neutral region of the junction, such as diffusion recombination and the drift effect [63] and I_{02} denotes the carrier recombination via deep levels in the space-charge region of the junction [64].

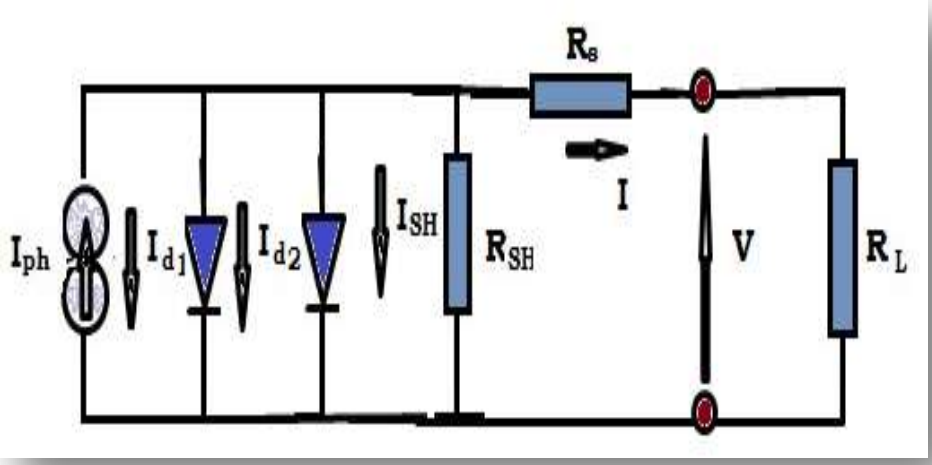

Figure 2.46: Equivalent circuit of a two-diode model solar cell

I_{02}, the reverse saturation current, is generally 3 to 7 orders of magnitude larger than I_{01}; the diode quality factor n equals 2 for the approximation corresponding to the Shockley-Read-Hall recombination current in the space-charge region [65]; n is also a fit parameter that is more than 2.

Chapter three:

Analytical modeling of contact with/without adhesion between layers

3.1. Analytical Modeling Contact and Adhesion

3.1.1. Analytical Modeling of Contact in Organic Solar Cells

Now consider the problem of pressure-assisted lamination-induced contact around a particle (dust). This is analogous to a cantilever deflection on a rigid particle. The deflection is given by:

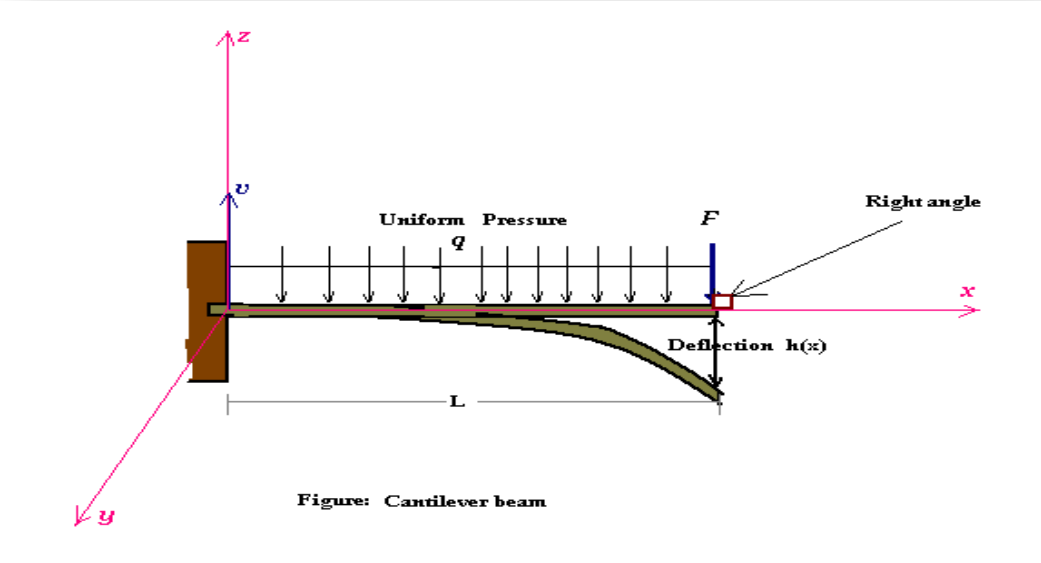

Figure 3.1: Undeformed and deformed cantilever beam under bending force F

L: Length of beam

h(x): Deflection

F: Applied force (or pressure)

v: Shear force

The maximum deflection experience by a cantilever beam under uniform pressure resulting from the applied force is given by (details of calculation in appendix A1):

$$h_{max} = -\frac{FL^3}{3EI} \quad [3.1]$$

3.1.2. Modelling of Contact

3.1.2.1. Analogy

The contact at the interfaces of the layers and the defect (dust particle, Void ...) are treated similar to the cantilever beam approach under the following assumptions:

- The defect/particle is rigid enough to cause bending under uniform pressure
- There is no sink in of the particle

Under these assumptions, the system looks like an elastic wrapping of the layer 1 (as in the case of the beam) around the defect/particle under pressure lamination in two ways as shown in the figures below.

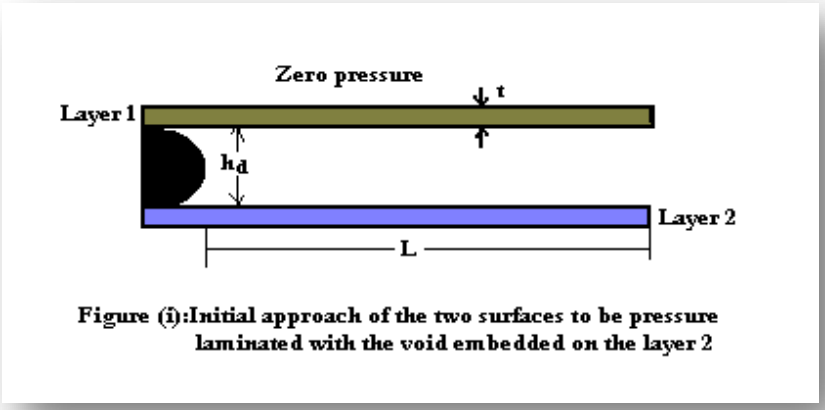

Figure (i):Initial approach of the two surfaces to be pressure laminated with the void embedded on the layer 2

Figure 3.2: (i) Modeled interfaces contact without pressure

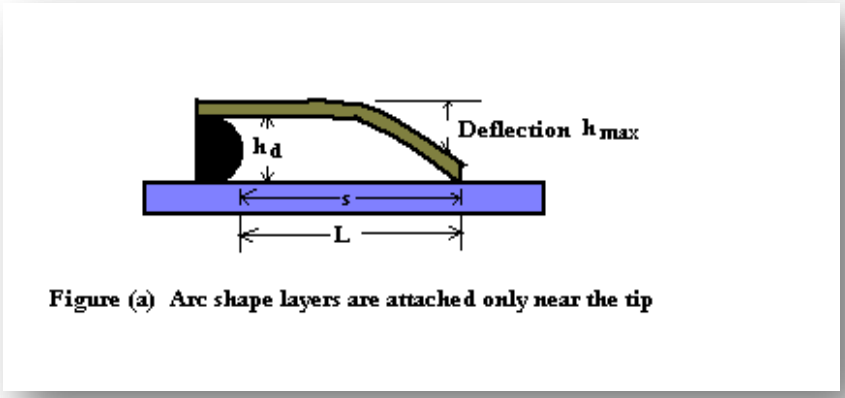

Figure (a) Arc shape layers are attached only near the tip

Figure 3.2: (ii) Arc-shape under pressure lamination

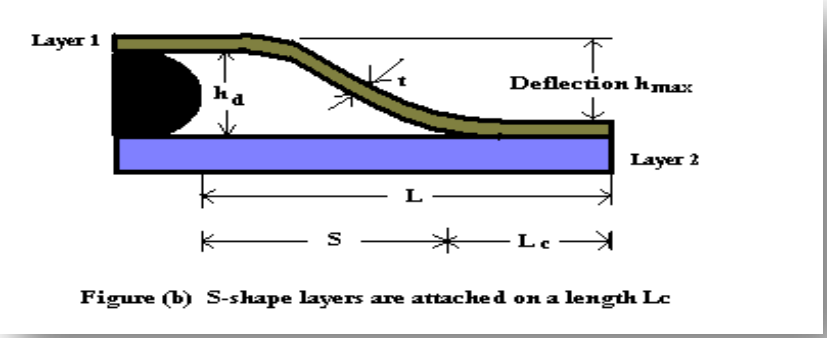

Figure 3.2: (ii) S-shape under pressure lamination

From careful and mathematical concept one can map $\boldsymbol{h_{max}}$ to $\boldsymbol{h_d}$, the height of the particle and also the length of the beam $\boldsymbol{L}$ to $\boldsymbol{s}$, the separation shown in figure 3.2 (ii)a.

In that case

$$\boldsymbol{h_d = -\frac{FL^3}{3EI}} \quad \textbf{[3.2]}$$

But $L=s$ and substituting we now have:

$$\boldsymbol{h_d = -\frac{Fs^3}{3EI}} \quad \textbf{[3.3]}$$

3.1.2.2. Elastic (Strain) energy

- Case 1: The Arc-shape

The strain/elastic energy stored in the layer due to bending is given by:

$$\boldsymbol{dU_e = \frac{1}{2}Md\emptyset} \quad \textbf{[3.4]}$$

But from the figure shown below, it is known that $\boldsymbol{ds = Rd\emptyset}$ i.e. $\boldsymbol{d\emptyset = \frac{ds}{R}}$

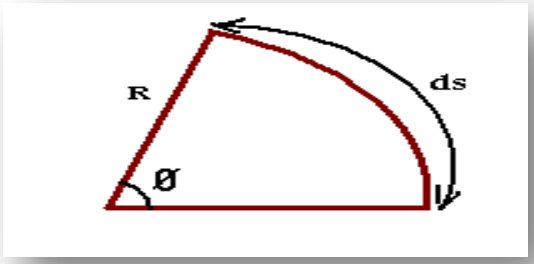

Figure 3.3: Relation between angle and radius

Substituting $d\emptyset$ in the equation [3.4] above, we then get:

$$dU_e = \frac{1}{2R} M ds \quad [3.5]$$

Also $\frac{M}{I} = \frac{E}{R}$ meaning that $R = \frac{EI}{M}$; putting it back into the equation [3.5] we now obtain:

$$dU_e = \frac{M^2}{2EI} ds \quad [3.6]$$

For a small displacement $ds = dx$

$$dU_e = \frac{M^2}{2EI} dx \quad [3.7]$$

Integrating both sides yields:

$$\int dU_e = \int_0^s \frac{M^2}{2EI} dx \quad [3.8]$$

But $M = F(s - x)$ and so it follows that:

$$U_{e\,Arc-shape} = \frac{F^2}{2EI} \int_0^s (s - x)^2 dx \quad [3.9]$$

Expanding the term at the RHS of the equality we have:

$$U_{e\,Arc-shape} = \frac{F^2 s^2}{2EI} \int_0^s dx - \frac{2sF^2}{2EI} \int_0^s x dx + \frac{F^2}{2EI} \int_0^s x^2 dx \quad [3.10]$$

Finishing the integration we get:

$$U_{e_{Arc-shape}} = \frac{F^2 s^3}{2EI} - \frac{F^2 s^3}{2EI} + \frac{F^2 s^3}{6EI} \quad [3.11]$$

Finally the elastic/strain energy is given by:

$$U_{e_{Arc-shape}} = \frac{F^2 s^3}{6EI} \quad [3.12]$$

From equation [3.3], F is given by:

$$F = \frac{3EI}{s^3} h_d \quad [3.13]$$

Putting the value of F into equation [3.12] we obtain:

$$U_{e_{Arc-shape}} = \frac{(\frac{3EI}{s^3} h_d)^2 s^3}{6EI} = \frac{9E^2 I^2 s^3 h_d^2}{6EIs^6} \quad [3.14]$$

Therefore the elastic energy can be written as:

$$U_{e_{Arc-shape}} = \frac{3}{2}\frac{EI}{s^3} h_d^2 \quad [3.15]$$

- Case 2: The S-shape

From Zong et al. (2006), the total energy of the system as shown in the Figure 3.2 (ii)b is the sum of the elastic energy U_e stored in the beam due to the bending (S-shape) and the interfacial adhesion energies, U_s. This gives [66]:

$$U_T = U_{e_{s-shape}} + U_s \quad [3.16]$$

where

$$U_{e_{s-shape}} = \frac{6EI}{s^3} h_d^2 \quad [3.17]$$

and

$$U_s = \gamma b L_c \quad [3.18]$$

3.1.2.3. Contact length

Considering layers of length (L) and void length (s) as shown in figure in figure 3.3,

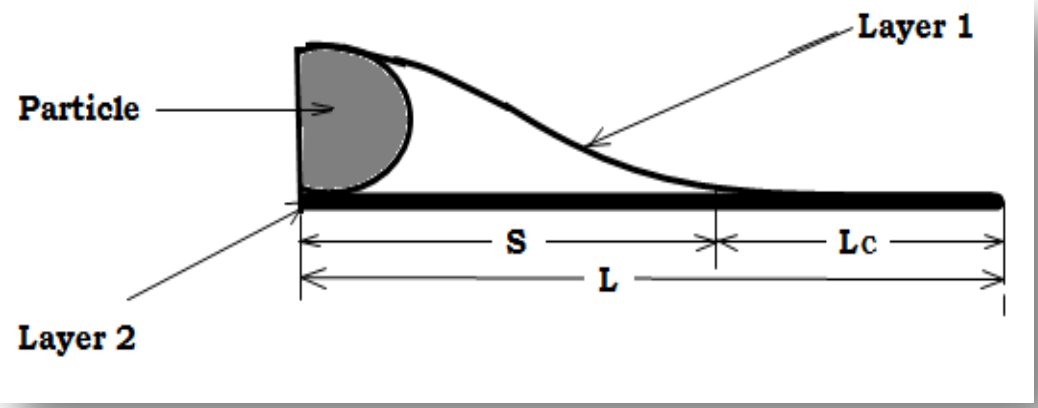

Figure 3.4: Contact length

the contact length (L_c) is given by:

$$\boldsymbol{L_c = L - s} \qquad \textbf{[3.19]}$$

where $\boldsymbol{s}$ is the length between the particle and the point of contact of the bended layer 1 and the layer 2. To know the real contact length one would have to determine the real value of $\boldsymbol{s}$.

This can be done, considering the total derivative of the energy of the system with respect to $\boldsymbol{s}$ at equilibrium.

The energy of the system is given by:

$$\boldsymbol{U_T = U_e + U_s} \qquad \textbf{[3.20]}$$

We have in our previous section already determined the elastic (or strain energy) $\boldsymbol{U_e}$, and this for the two types of shapes. The surface energy $\boldsymbol{U_s}$, and how it is obtained will be discussed in details in the next section.

3.1.2.4. Getting void length *s*

- **Case 1: Arc-shape ($s_{Arc-shape}$)**

Consider the diagram below:

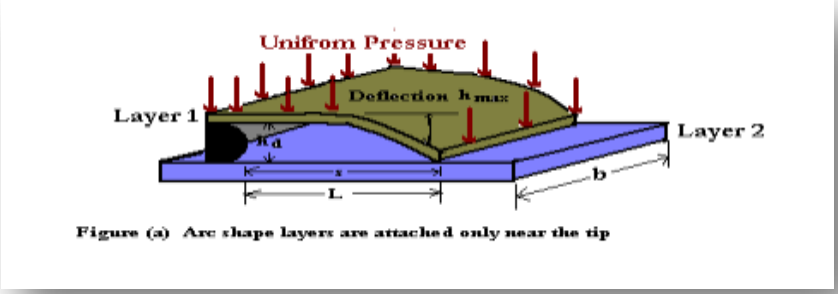

Figure (a) Arc shape layers are attached only near the tip

Figure 3.5: **3-D Arc shape**

Considering a system of two layers with breadth $\boldsymbol{b}$, the total energy as stated in one of the previous section is given by:

$$\boldsymbol{U_T = U_{e_{Arc-shape}} + U_s} \quad \textbf{[3.21]}$$

But

$$\boldsymbol{U_s = \gamma b L_c} \quad \textbf{[3.22]}$$

So we have:

$$\boldsymbol{U_T = U_{e_{Arc-shape}} + \gamma b L_c} \quad \textbf{[3.23]}$$

Fixing equation [3.19] into [3.23] above yields:

$$\boldsymbol{U_T = U_{e_{Arc-shape}} + \gamma b(L - s)} \quad \textbf{[3.24]}$$

Doing the same for equation [3.15] we finally get:

$$\boldsymbol{U_T(s) = \frac{3}{2}\frac{EI}{s^3}h_d^2 + \gamma b(L - s)} \quad \textbf{[3.24]}$$

This total energy $\boldsymbol{U_T(s)}$ of the system (to be plotted in section 3.1.3) has a single minimum corresponding to the equilibrium $\boldsymbol{s}$. This is found by setting the derivative of the total energy with respect to s to zero.

$$\frac{dU_T(s)}{ds} = \mathbf{0} \qquad \textbf{[3.25]}$$

Let us find:

$$\frac{dU_T(s)}{ds} = \frac{d}{ds}\left[\frac{3}{2}\frac{EI}{s^3}h_d^2 + \gamma b(L-s)\right]$$

$$\frac{dU_T(s)}{ds} = \frac{3}{2}EIh_d^2\left(\frac{-3s^2}{s^6}\right) - \gamma b(-1)$$

$$\frac{dU_T(s)}{ds} = -\frac{9}{2}\frac{EIh_d^2}{s^4} + \gamma b \qquad \textbf{[3.26]}$$

Then we carry on the equality:

$$\frac{dU_T(s)}{ds} = \mathbf{0}$$

$$-\frac{9}{2}\frac{EIh_d^2}{s^4} + \gamma b = \mathbf{0} \qquad \textbf{[3.27]}$$

After rearranging the terms on both sides in successive steps we get:

$$\frac{EIh_d^2}{s^4} = \frac{2}{9}\gamma b$$

$$S_{Arc-shape}^{-4} = \frac{\frac{2}{9}\gamma b}{EIh_d^2}$$

$$S_{Arc-shape}^{4} = \frac{9EIh_d^2}{2\gamma b} \qquad \textbf{[3.28]}$$

But we know that:

$$I = \frac{bt^3}{12} \qquad \textbf{[3.29]}$$

Substituting $\boldsymbol{I}$ into equation [3.28] yields:

$$S^4_{Arc-shape} = \frac{9}{24}\frac{Ebt^3h_d^2}{\gamma b}$$

$$S^4_{Arc-shape} = \frac{3}{8}\frac{Et^3h_d^2}{\gamma} \quad [3.30]$$

So finally the value of s is given by:

$$s_{Arc-shape} = \left(\frac{3}{8}\frac{Et^3}{\gamma}h_d^2\right)^{1/4} \quad [3.31]$$

➢ **Case 2: S-shape ($s_{S-shape}$)**

Consider the diagram below:

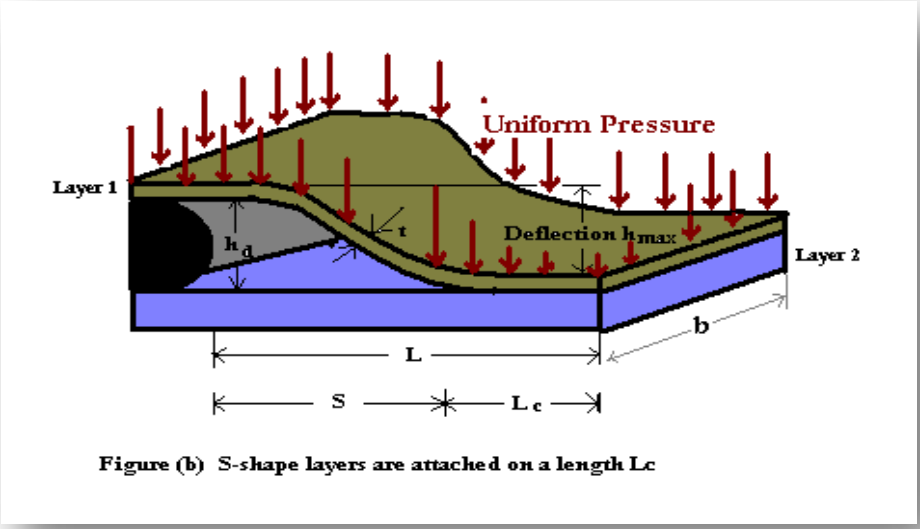

Figure (b) S-shape layers are attached on a length Lc

Figure 3.6: 3-D s-shape

Considering a system of two layers with breadth b, the total energy as stated in one of the previous section is given by:

$$U_T = U_{eS-shape} + U_s \quad [3.32]$$

But

$$U_s = \gamma b L_c \quad [3.33]$$

So we have:

$$\boldsymbol{U_T = U_{e_{S-shape}} + \gamma b L_c} \quad \textbf{[3.34]}$$

Fixing equation [3.19] into [3.34] above yields:

$$\boldsymbol{U_T = U_{e_{S-shape}} + \gamma b (L - s)} \quad \textbf{[3.35]}$$

Doing the same for equation [3.17] we finally get:

$$\boldsymbol{U_T(s) = \frac{6EI}{s^3} h_d^2 + \gamma b (L - s)} \quad \textbf{[3.36]}$$

Similarly taking the derivative we have:

$$\boldsymbol{\frac{dU_T(s)}{ds} = 0} \quad \textbf{[3.37]}$$

Finding the derivative:

$$\boldsymbol{\frac{dU_T(s)}{ds} = \frac{d}{ds}\left[\frac{6EI}{s^3} h_d^2 + \gamma b (L - s)\right]}$$

$$\boldsymbol{\frac{dU_T(s)}{ds} = 6EIh_d^2 \left(\frac{-3s^2}{s^6}\right) - \gamma b(-1)}$$

$$\boldsymbol{\frac{dU_T(s)}{ds} = -18\frac{EIh_d^2}{s^4} + \gamma b} \quad \textbf{[3.38]}$$

Then we carry on the equality:

$$\boldsymbol{\frac{dU_T(s)}{ds} = 0}$$

$$\boldsymbol{-18\frac{EIh_d^2}{s^4} + \gamma b = 0} \quad \textbf{[3.39]}$$

Rearranging the terms on both sides we get:

$$\boldsymbol{\frac{EIh_d^2}{s^4} = \frac{1}{18}\gamma b}$$

$$\boldsymbol{S_{S-shape}^{-4} = \frac{\frac{1}{18}\gamma b}{EIh_d^2}}$$

$$S_{S-shape}^4 = \frac{18EIh_d^2}{\gamma b} \quad [3.40]$$

But

$$I = \frac{bt^3}{12} \quad [3.41]$$

Substituting it into equation [3.40] yields:

$$S_{S-shape}^4 = \frac{18}{12}\frac{Ebt^3h_d^2}{\gamma b}$$

$$S_{S-shape}^4 = \frac{3}{2}\frac{Et^3h_d^2}{\gamma} \quad [3.42]$$

So finally the value of s is given by:

$$s_{S-shape} = \left(\frac{3}{2}\frac{Et^3}{\gamma}h_d^2\right)^{1/4} \quad [3.43]$$

In summary, the expression for the void length s is:

$$s_{S-shape} = \left(\frac{3}{2}\frac{Et^3}{\gamma}h_d^2\right)^{1/4}$$

and

$$s_{Arc-shape} = \left(\frac{3}{8}\frac{Et^3}{\gamma}h_d^2\right)^{1/4} \quad [3.44]$$

3.1.3. The energy of the system

In our study we distinguished two ways of bending and adhesion contacts between the layers. This was suggested by the analogy with beam structures. This adhesion of suspended beam structures, had been already proposed by Mastrangelo and Hsuin [67, 68] literature in which they reported two adhesion configurations, the S-shaped and arc-shaped adhesions.

As we have seen in the previous section, the total energy of the system is the sum of the elastic energy stored in the beam due to the bending, plus the interfacial adhesion energies of the contact area. This is given by equation (3.45):

$$\boldsymbol{U_T = U_e + U_s} \qquad \textbf{[3.45]}$$

A typical plot of the energies is shown in Figure (3.6), while that obtained by the simulation (using Matlab) is shown in the next chapter on results in Figure (4.17).

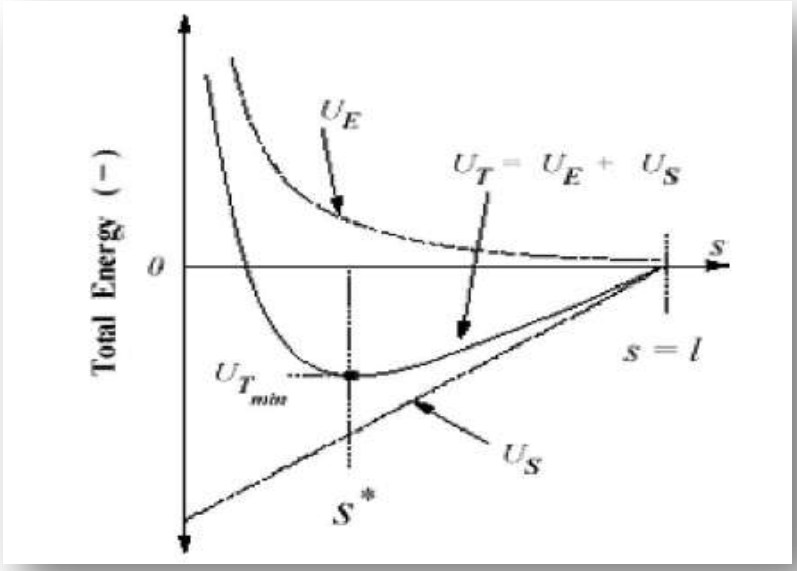

Figure 3.7: Typical energy curves [69]

Meanwhile in our two cases, we established the following given by Equations (3.24) and (3.36) for the arc shape and the s-shape, respectively:

$$\boldsymbol{U_T(s) = \frac{3}{2}\frac{EI}{s^3}h_d^2 + \gamma b(L - s)}$$

$$\boldsymbol{U_T(s) = \frac{6EI}{s^3}h_d^2 + \gamma b(L - s)}$$

where E is the Young's modulus of the layer; γ is the adhesion energy; and I is the second moment of area.

In the previous section we explained into details how the elastic energies are derived, but in this section, our focus is to explain briefly how the surface energy given by equation (3.33) is obtained; i.e.

$$\boldsymbol{U_s = \gamma b L_c = \gamma b (L - s)}$$

This has also been an area of intensive research work. Measuring the surface energy is strongly dependent on the adhesion due surface contact at the nanoscale.

This was obtained using AFM measurements [70] and adhesion theories [70]. Maugis-Dugdale (MD theory-1992) [70] provides analytical solutions describing the contact between two adhesive elastic spheres that falls in the intermediate case between the Johnson-Kandall-Roberts (JKR-1971) [71] and the Derjagin-Muller-Toropov (DMT–1975) [72] models. While the JKR model (shown in Figure 3.8a) applies to surfaces of soft materials with strong adhesive forces, the DMT models [72] applies to stiff materials with weak adhesive forces (Figure 3.8b).

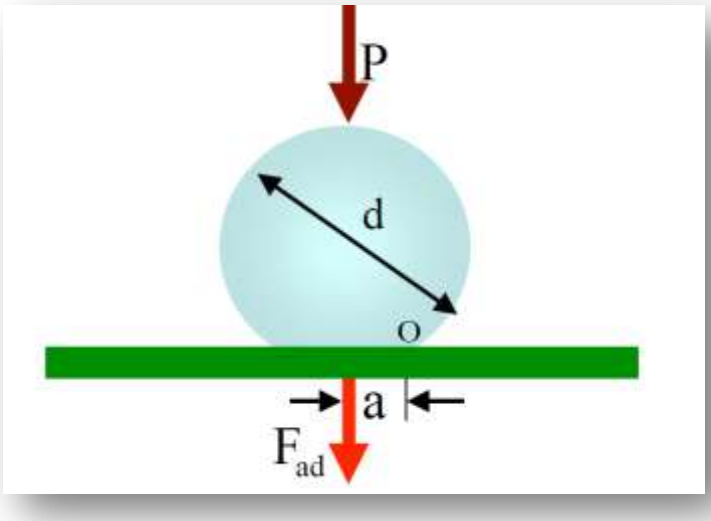

Figure 3.8: JKR model [73]

The actual situation which is a transitional mode between the JKR and the DMT models is developed by the use of the MD theory (Figure 3.8c). Moreover, in the transition region, a

qualitatively new phenomenon – **adhesion** arises. It originates from the short-range molecular forces. The character of adhesion affects the force curve parts "fitting". The fitting function is called the **adhesion interaction**. The plots in Figures 3.8 a-c illustrate the three models:

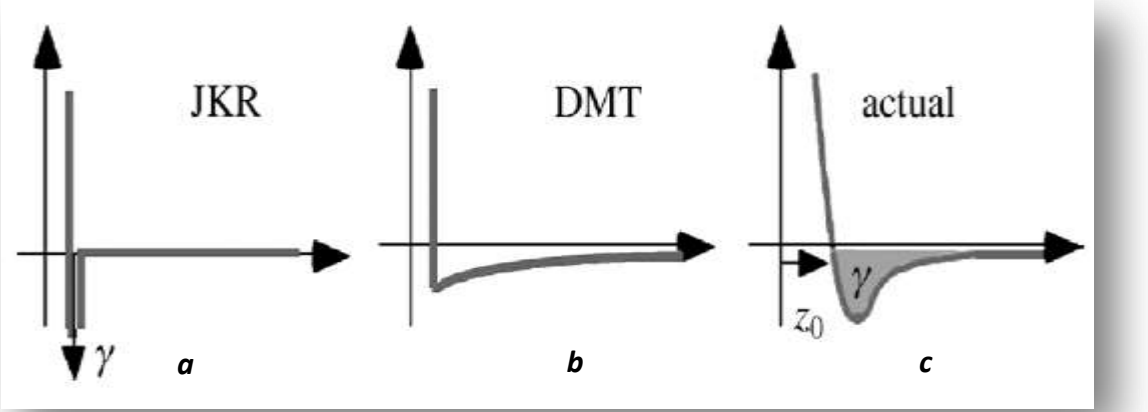

Figure 3.9: A plot of the three models [72]

The most common experimental measurement technique used in present days is the AFM (Atomic Force Microscopy). To use the AFM as a quantitative tool to investigate interfacial adhesion, cantilever calibration procedures and contact mechanics modeling need to be applied consistently. Adhesion data taken with the AFM can vary significantly due to subtle changes in the environmental conditions, AFM tip material and/or geometry, and surface contamination and/or modification. To ensure that calculated values for work of adhesion are intrinsic to the interface tested; rigorous characterization techniques of the tip and surface materials must be performed.

The MD model defines a non-dimensional [74] parameter,$\boldsymbol{\lambda}$, that is given by:

$$\boldsymbol{\lambda = 2\sigma_0 \left(\frac{R}{\pi K^2 \gamma}\right)^{1/3}} \qquad \textbf{[3.46]}$$

where $\boldsymbol{\sigma_0}$ is a constant attractive force that exists between the two adhered layers; $\boldsymbol{\gamma}$ is adhesion energy to be established soon and $\boldsymbol{R}$ is the reduced radius and is calculated as:

$$\boldsymbol{R = \left(\frac{1}{R_{rms}} - \frac{1}{R_{tip}}\right)^{-1}} \quad \textbf{[3.47]}$$

with R_{rms}: root- mean squared roughness of layer obtained from AFM tip; R_{tip}: radius of the coated AFM tip; K is the reduced elastic modulus of tip and sample and is given by:

$$\boldsymbol{K = \frac{3}{4}\left[\frac{(1-\nu_1^2)}{E_1} + \frac{(1-\nu_2^2)}{E_2}\right]^{-1}} \quad \textbf{[3.48]}$$

with E_i is Young's modulus of the tip of the layer and ν is the Poisson ratio of the material. In the transition region, the non-dimensional parameter $\bar{F}$ is related to the pull-off force F through the following relation [74]:

$$\boldsymbol{\bar{F} = \frac{F}{\pi\gamma R}} \quad \textbf{[3.49]}$$

The interfacial or adhesion energy, $\boldsymbol{\gamma}$, can be obtained rearranging equation (3.49):

$$\boldsymbol{\gamma = \frac{F_{ad}}{\pi R \bar{F}_{ad}}} \quad \textbf{[3.50]}$$

with $\boldsymbol{F_{ad}}$ is the pull-off force measured in AFM experiment . $\bar{F}_{ad}$ is given by the empirical equation of Pietrement and Troyon [75]:

$$\boldsymbol{\bar{F}_{ad}(\alpha) = 0.267\alpha^2 - 0.767\alpha + 2} \quad \textbf{[3.51]}$$

where $\boldsymbol{\alpha}$ is another non-dimensional parameter. It is equal to ***1*** for the JKR and ***0*** for the DMT models, respectively. For the intermediate case it is between 0.07 and 0.98. Since we are in the intermediate case, $\boldsymbol{\bar{F}_{ad}}$ reduces to **2**. So finally, the adhesion energy is given by:

$$\boldsymbol{\gamma = \frac{F_{ad}}{2\pi R}} \quad \textbf{[3.52]}$$

which is also predicted and given exactly by the DMT theory.

Chapter Four:

Results, Analysis and Discussion

4.1. Introduction

This present chapter presents the results and their analysis. Results obtained from the modeling in chapter three are presented in graphical form for better appreciation. All graphs showed are obtained and plotted through codes written (shown in appendix) with the software Matrix Laboratory (the language of technical computing) popularly known as MATLAB (Version R2007b, MathWorks Inc., Natick, Massachusetts, USA). The results are presented in the following order: Void lengths, Contact Lengths and System Energies.

The results are then commented and explained. This is followed by its implications and a summary on the chapter.

4.2. Void lengths

4.2.1. Plot void length (s) as a function of adhesion Energy for S- and arc-shape

For the s-shape the void length is given by: $$\boldsymbol{s_{S-shape}} = \left(\frac{3}{2}\frac{\boldsymbol{Et^3}}{\boldsymbol{\gamma}}\boldsymbol{h_d^2}\right)^{1/4}$$ and

For the s-shape the void length is given by: $$\boldsymbol{s_{Arc-shape}} = \left(\frac{3}{8}\frac{\boldsymbol{Et^3}}{\boldsymbol{\gamma}}\boldsymbol{h_d^2}\right)^{1/4}$$

In all the graphs as shown in Figures 4.1, 4.2 and 4.3, we observe under this section, there is a decrease in the curves: it is a kind of hyperbolic decrease behaviour for all curves of the void length, $\boldsymbol{s}$, as a function of the adhesion energy, $\boldsymbol{\gamma}$, for the different Young's modulus considered.

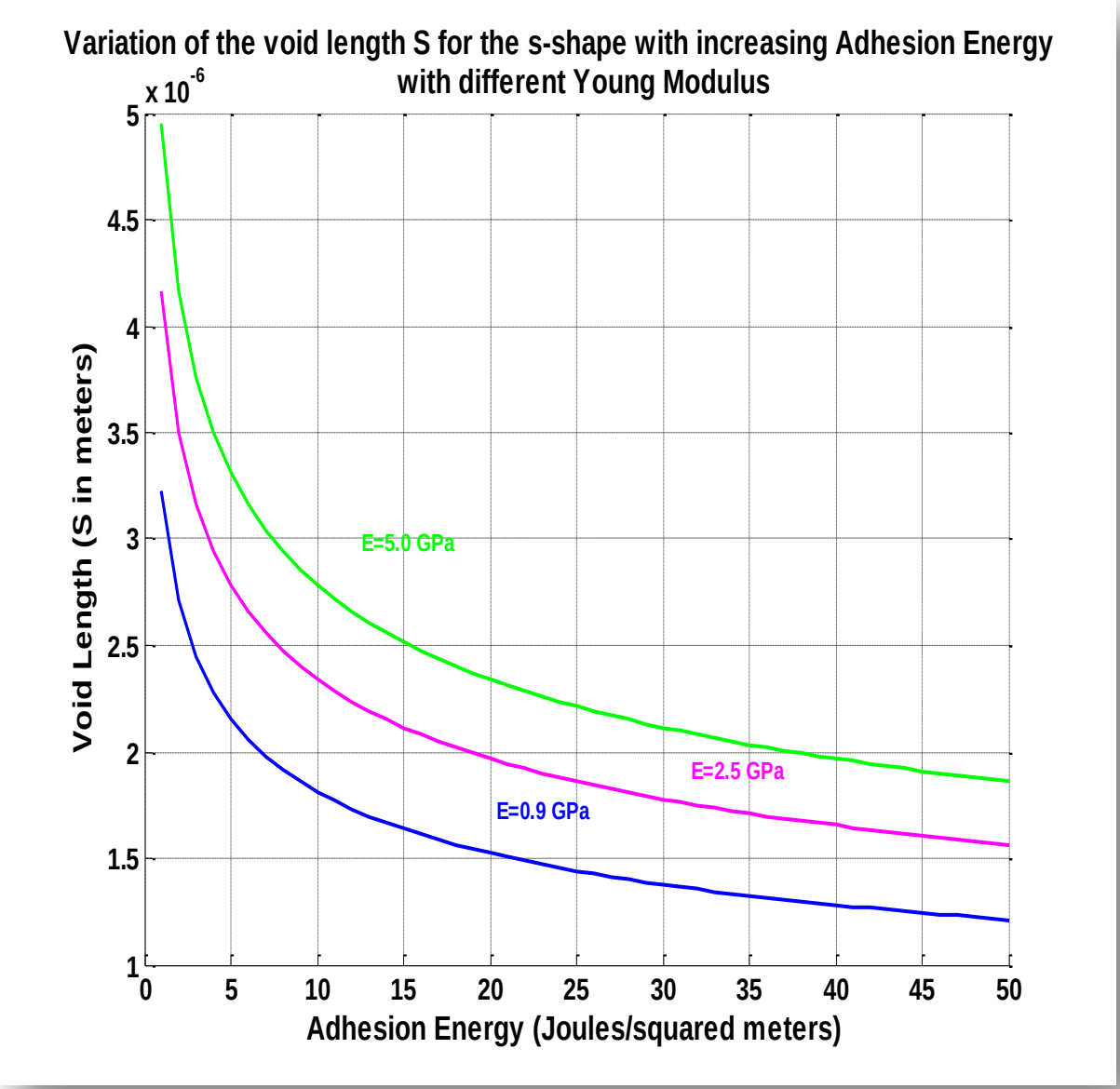

Figure 4.1: Plot of void length (s) for s-shape

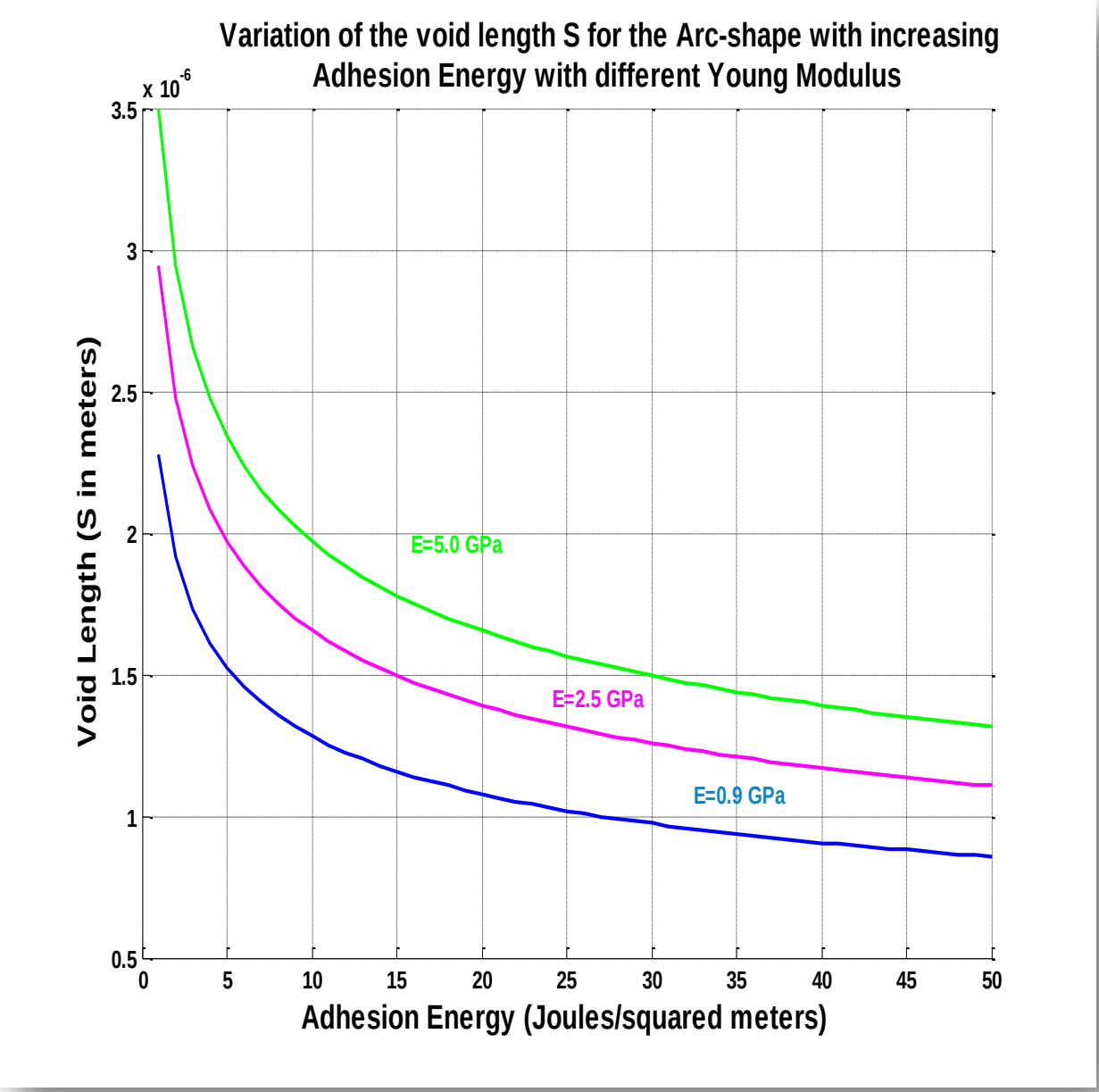

Figure 4.2: Plot of void length (s) for Arc-shape

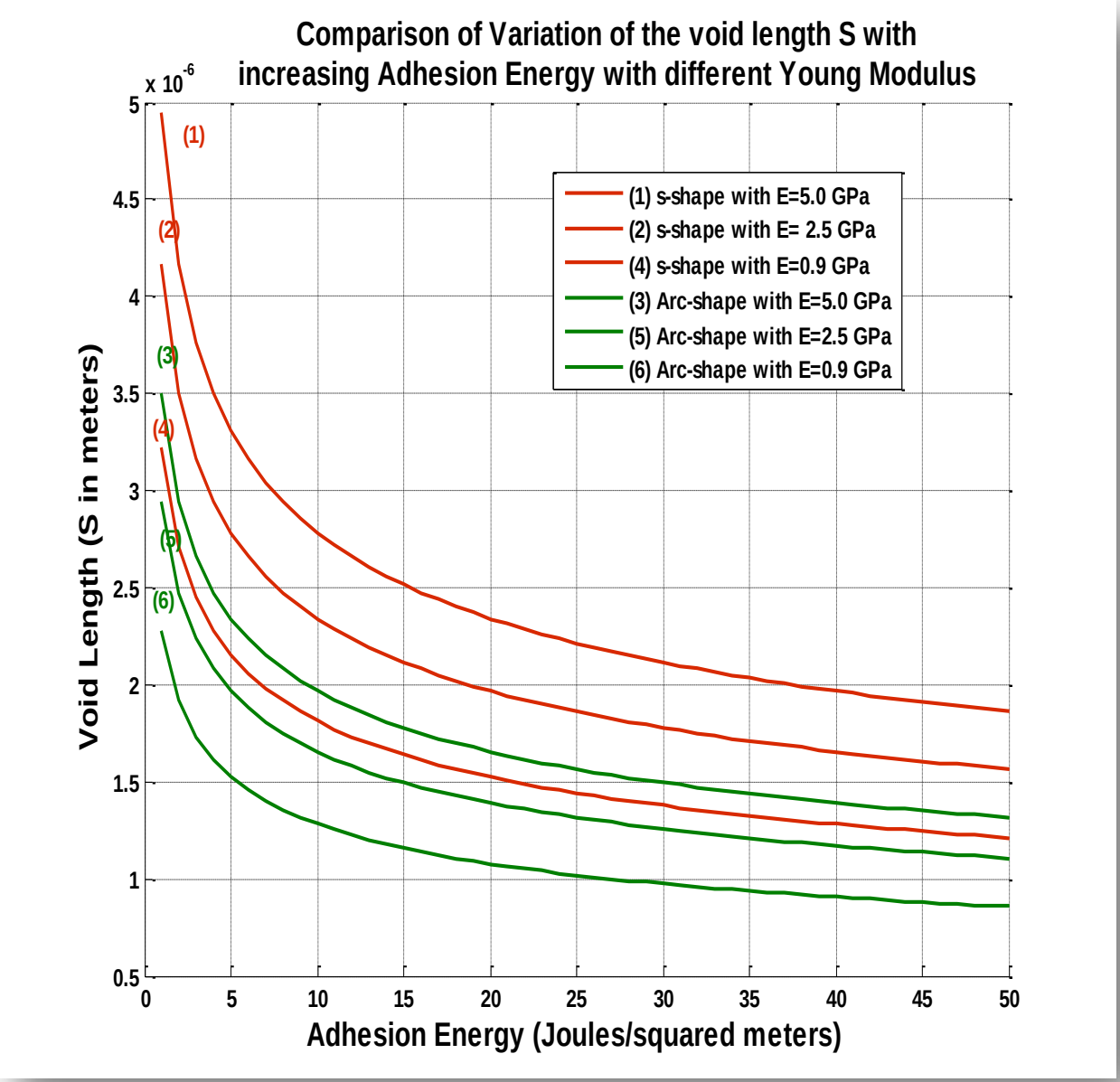

Figure 4.3: Plot of void length (s) for Arc-shape and S-shapes

4.2.2. Plot of the difference in the S- and Arc-shapes

The two shapes modeled gave rise all to void length, but of different dimensions. The comparison here is to find what is different in length about these two shapes. So we define Δs to be the difference in the two (2) void lengths, then we have:

$$\Delta s = \left(\frac{3}{2}\frac{Et^3}{\gamma}h_d^2\right)^{1/4} - \left(\frac{3}{8}\frac{Et^3}{\gamma}h_d^2\right)^{1/4} = \left(\frac{9}{8}\frac{Et^3}{\gamma}h_d^2\right)^{1/4} = constant \times \left(\frac{1}{\gamma}\right)^{1/4}$$

The hyperbolic behaviour of the curve prevails since the difference in the shapes is not qualitative but rather quantitative. The difference is in their multiplicative coefficient (a constant). The s-shape has a longer void length than the arc-shape.

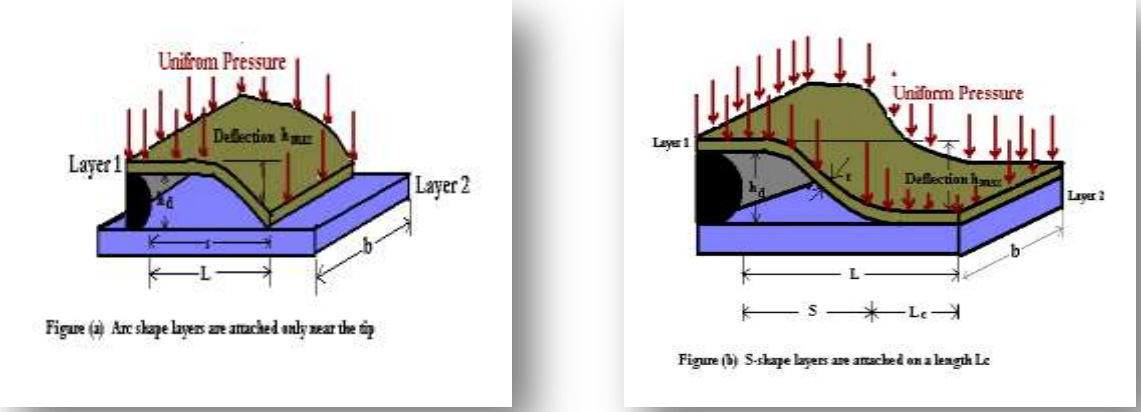

Figure 4.4: The two shapes Arc and S-shapes

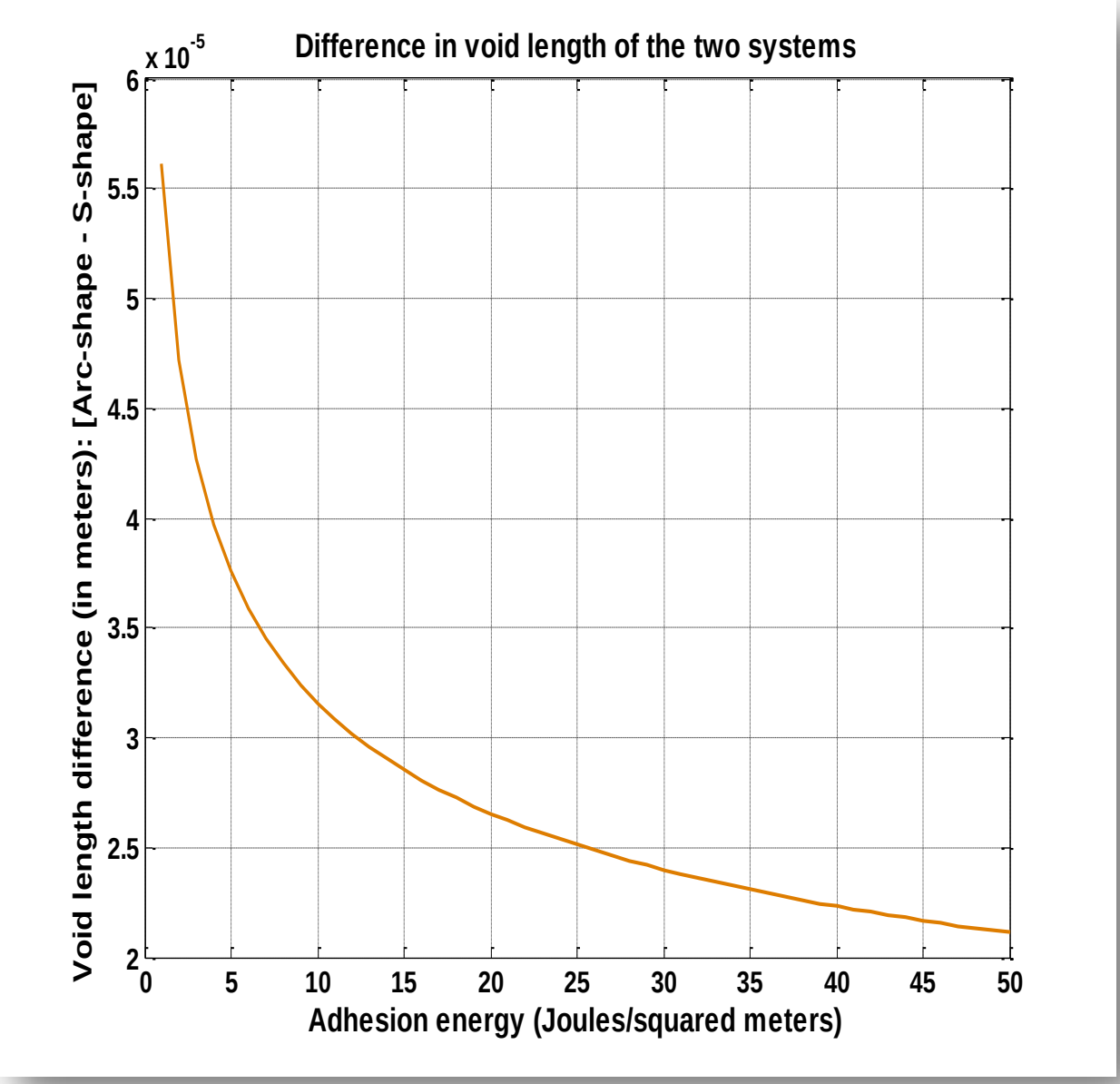

Figure 4.5: Plot of difference in void lengths (s)

4.2.3. Plot of the void length as a function of Young's modulus and pressure

This graph shows how the void length is affected by the Young's modulus of the layers. Typical polymers used in OPV solar cells have moduli between 0 – 5 GPa.

One can observe that there is an increase in shape of curve as the modulus increases.

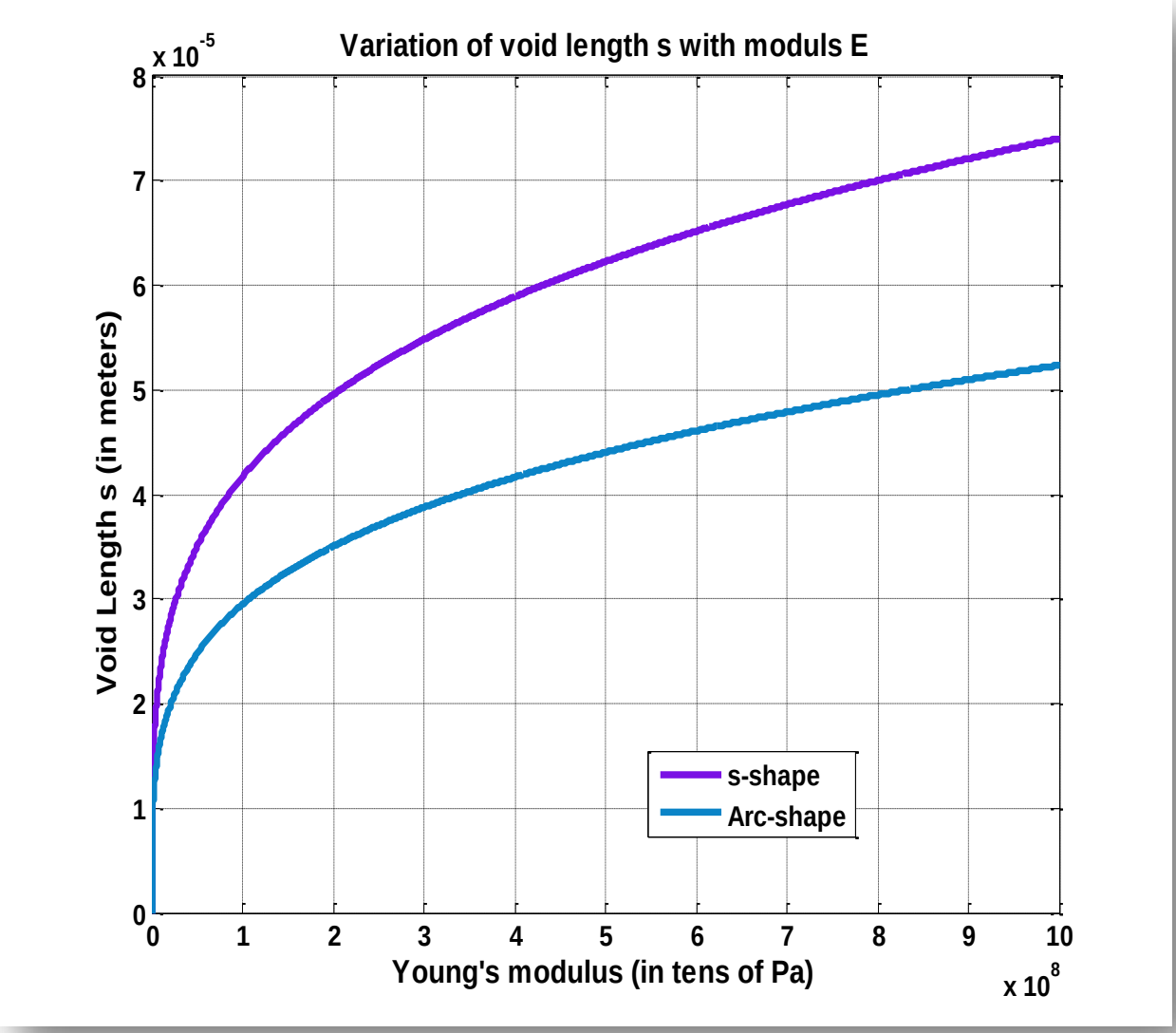

Figure 4.6: Plots of the variation of void length with Young's modulus

The graph below shows how the void length is affected by the pressure due lamination. The curves present a hyperbolic decrease behavior as the pressure increases. This is given by the following expressions:

For the s-shape, we have $S_{s-shape} = \left(\frac{1}{24}\frac{Et^3}{L^2}\right)^{1/2} \times \frac{1}{P}$ and

For the arc-shape, we have $S_{Arc-shape} = \left(\frac{1}{6}\frac{Et^3}{L^2}\right)^{1/2} \times \frac{1}{P}$

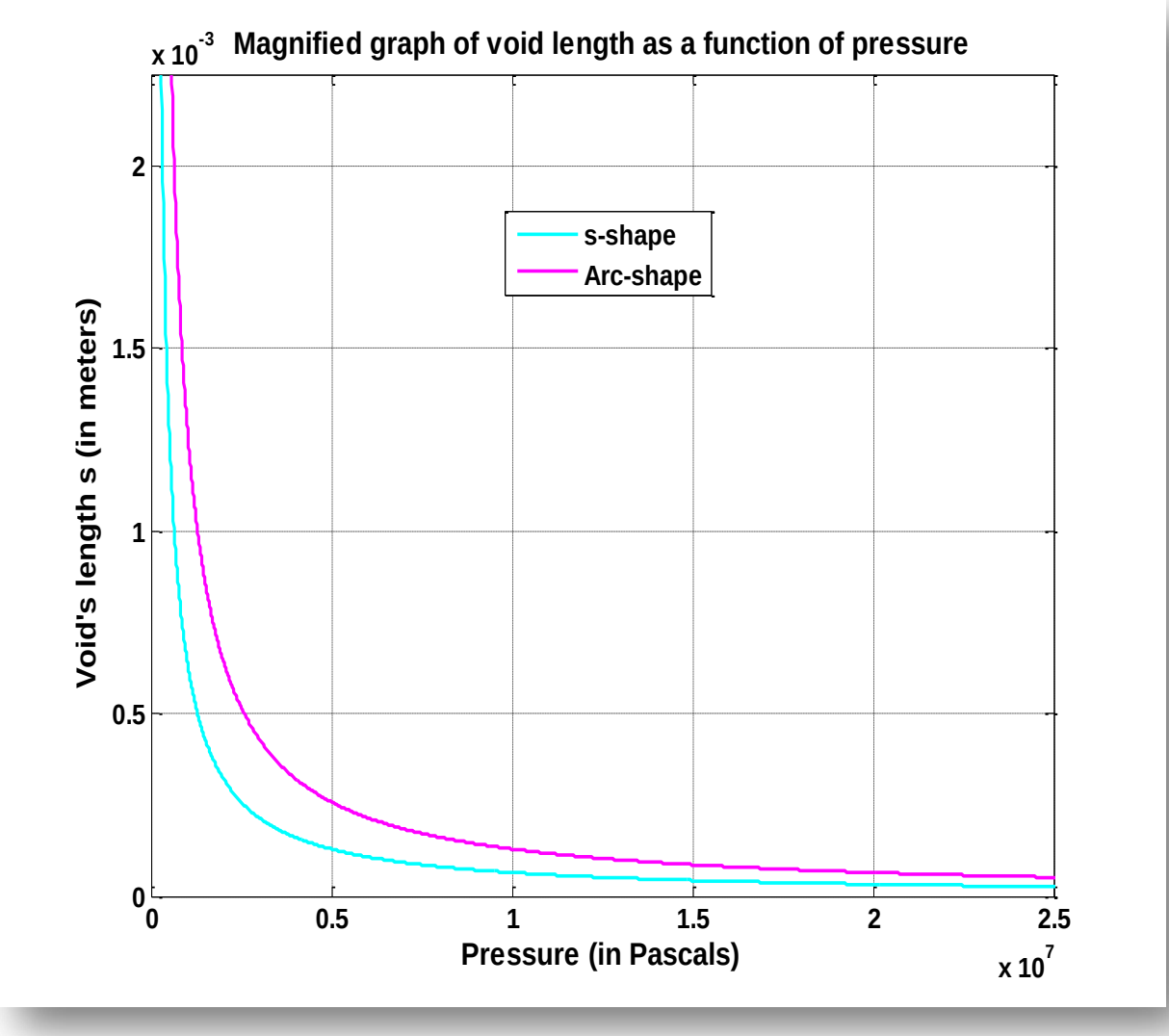

Figure 4.7: Plots of the variation of void length with pressure

4.3. Contact lengths

4.3.1. Plot of the ratio of contact length to length of layer Lc/L

As depicted in the Figure 4.8 below, the contact length is given by the following relations. For the arc shape $\boldsymbol{L_c = L - s = L - \left(\frac{3}{8}\frac{Et^3}{\gamma}h_d^2\right)^{1/4}}$ and so $\boldsymbol{\frac{L_c}{L} = 1 - \frac{s}{L}}$, and for the s-shape we have: $\boldsymbol{L_c = L - s = L - \left(\frac{3}{2}\frac{Et^3}{\gamma}h_d^2\right)^{1/4}}$.

Contrary to the void length, the contact length increases as the adhesion energy increases resulting in the increase of the curves of the ratio Lc/L as observed on the following graphs.

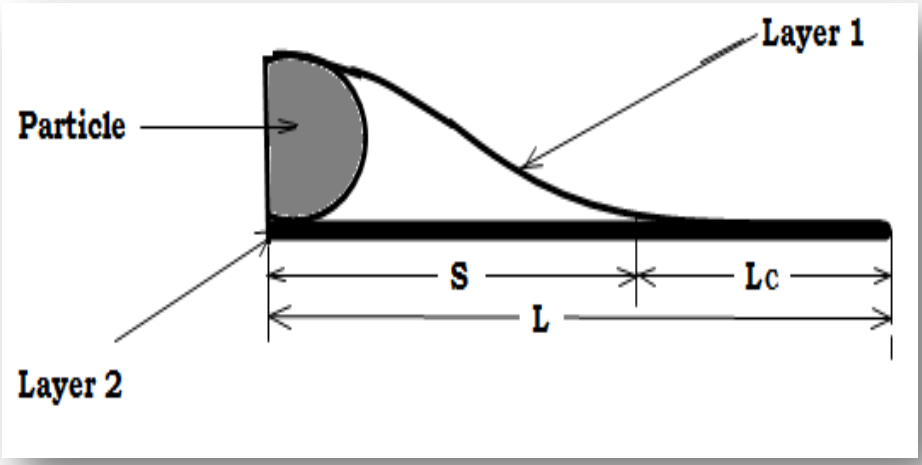

Figure 4.8: Contact lengths

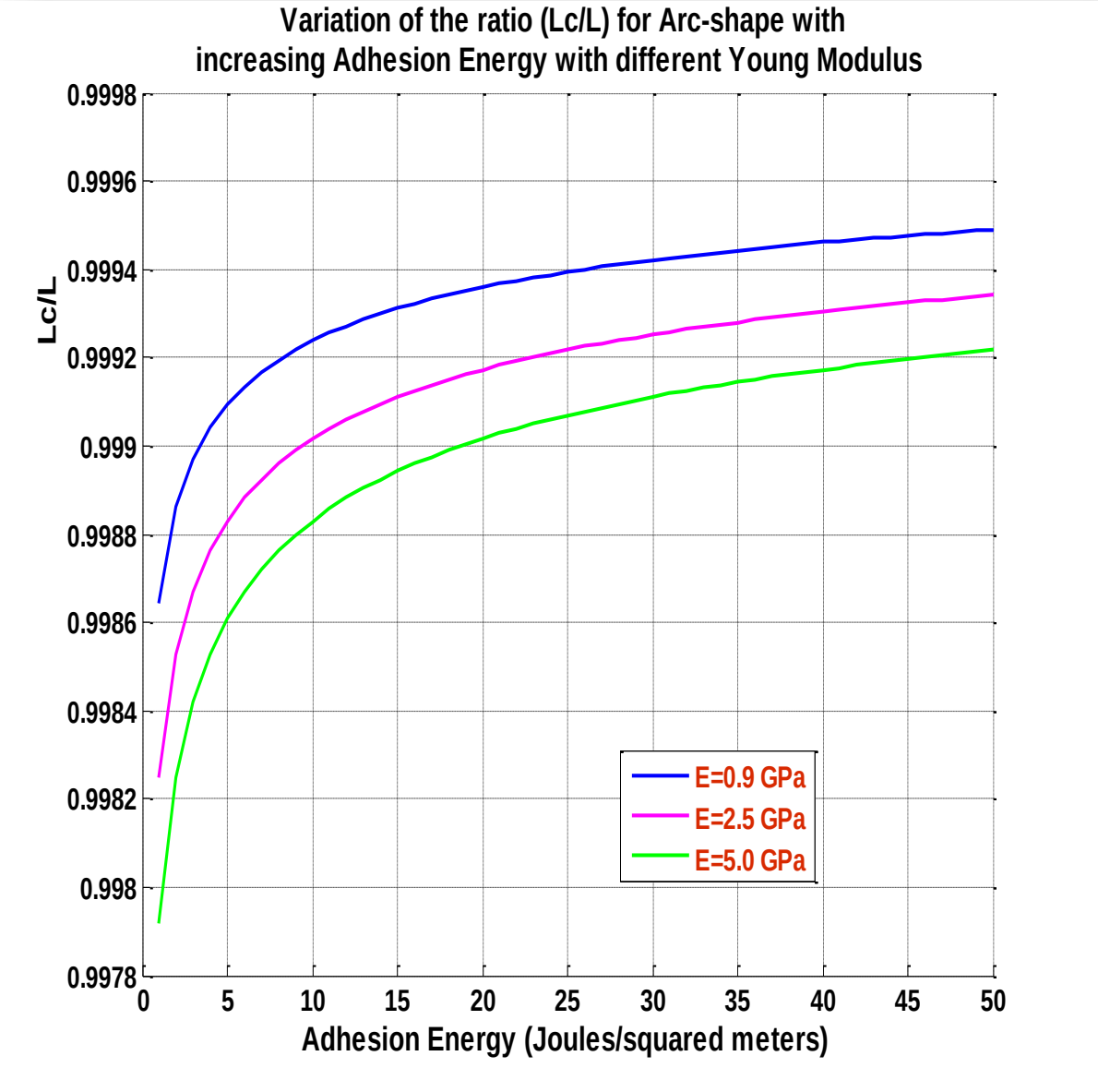

Figure 4.9: Plot of the ratio Lc/L for Arc-shape

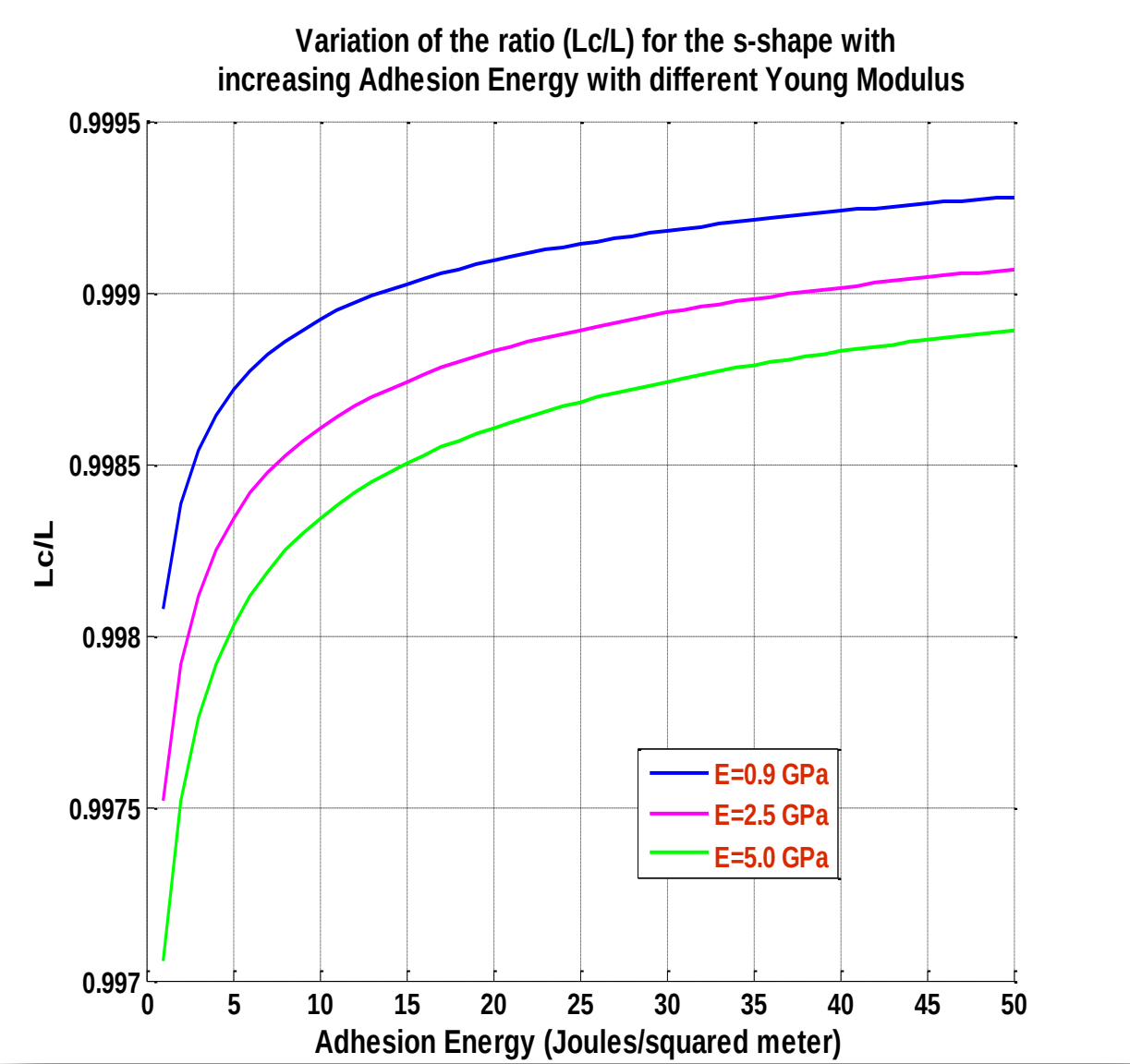

Figure 4.10: **Plot of the ratio Lc/L for S-shape**

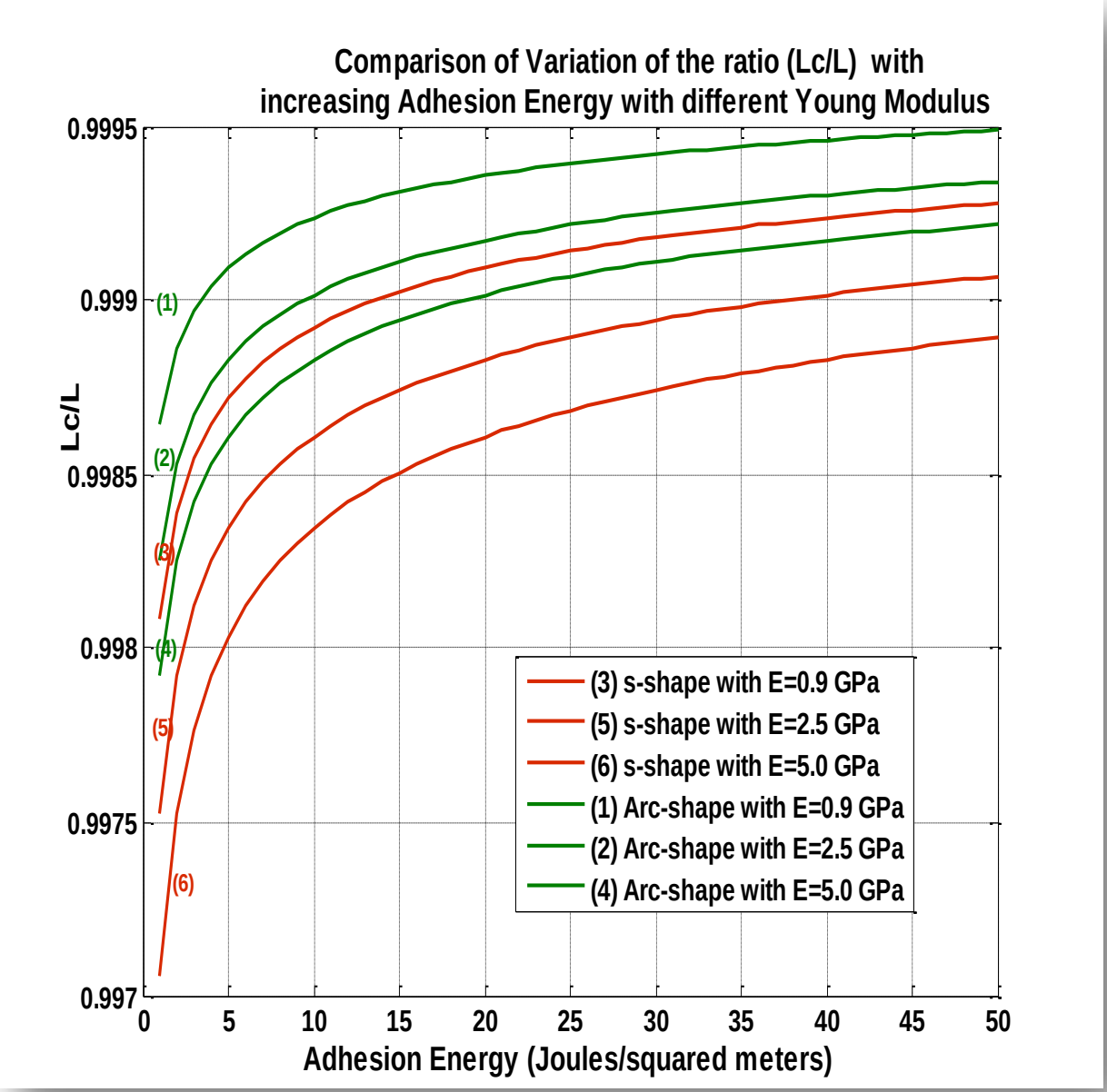

Figure 4.11: Plots of the ratio Lc/L for S-shape and Arc-shape

4.3.2. Plot of the ratio Lc/L as a function of Young's modulus and pressure

This graph shows how the ratio of lengths is affected by the Young's modulus of the layers and also how the ratio of lengths is affected by the pressure due to the lamination of the layers in the process of PDMS encapsulation in contrast to experimental results obtained by Cao et al. (2005) [75] . This ratio decreases exponentially as the modulus increases but it does rather increases to a saturation point of unity with increasing pressure as shown by the empirical results in Figures 4.12 and 4.15.

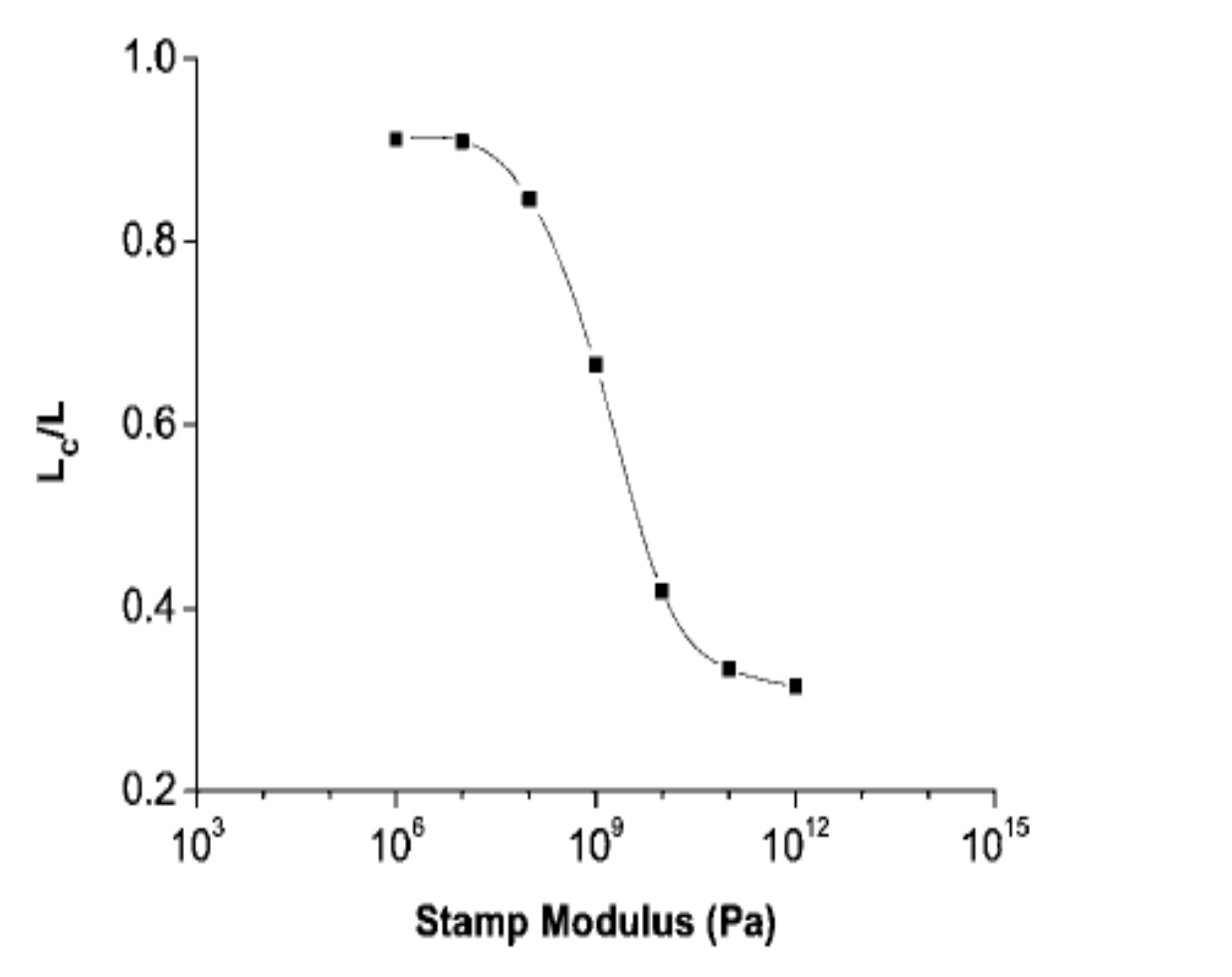

Figure 4.12: experimental result of ratio Lc/L with Young's modulus

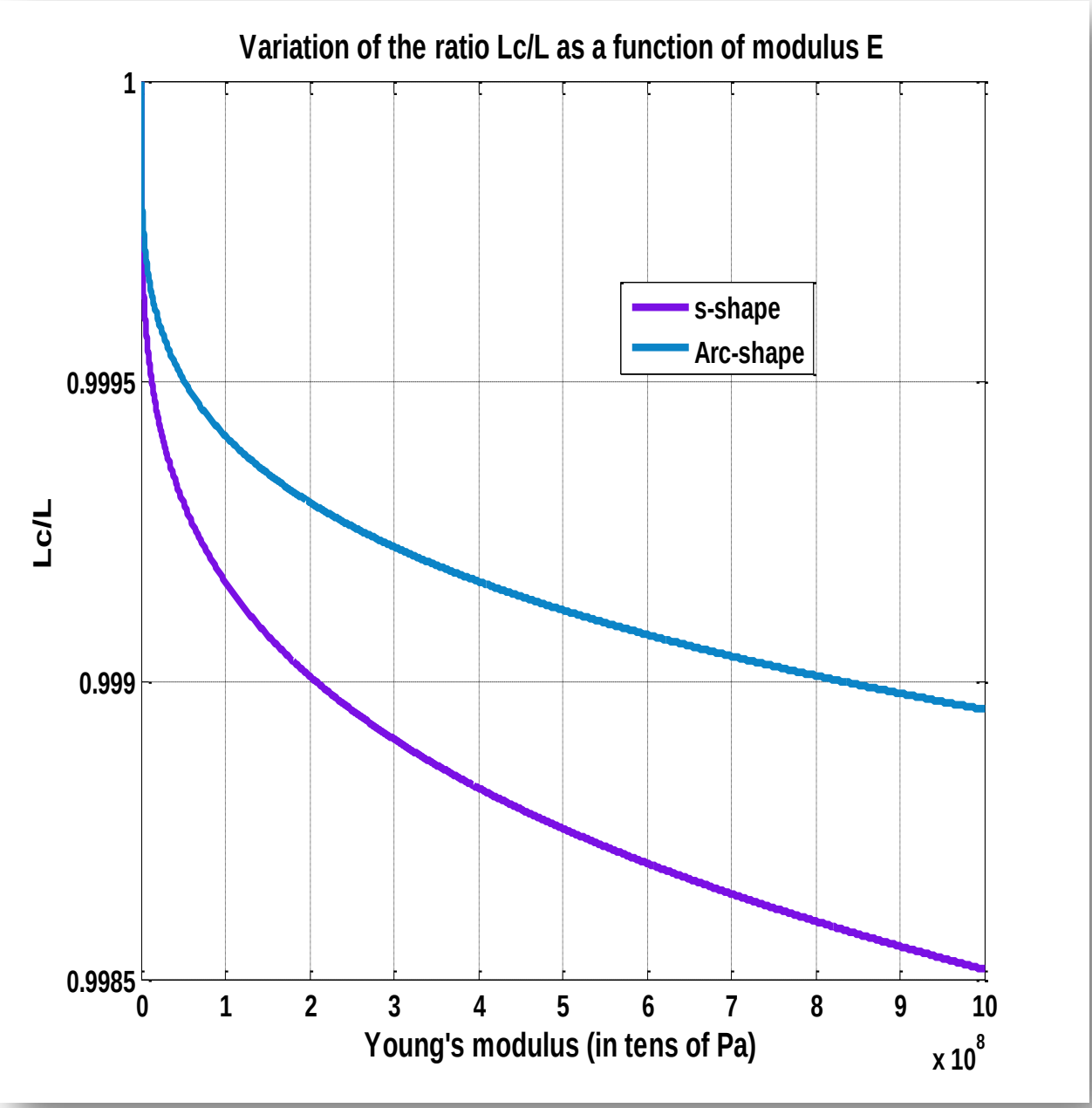

Figure 4.13: Plots of the variation of ratio Lc/L with Young's modulus

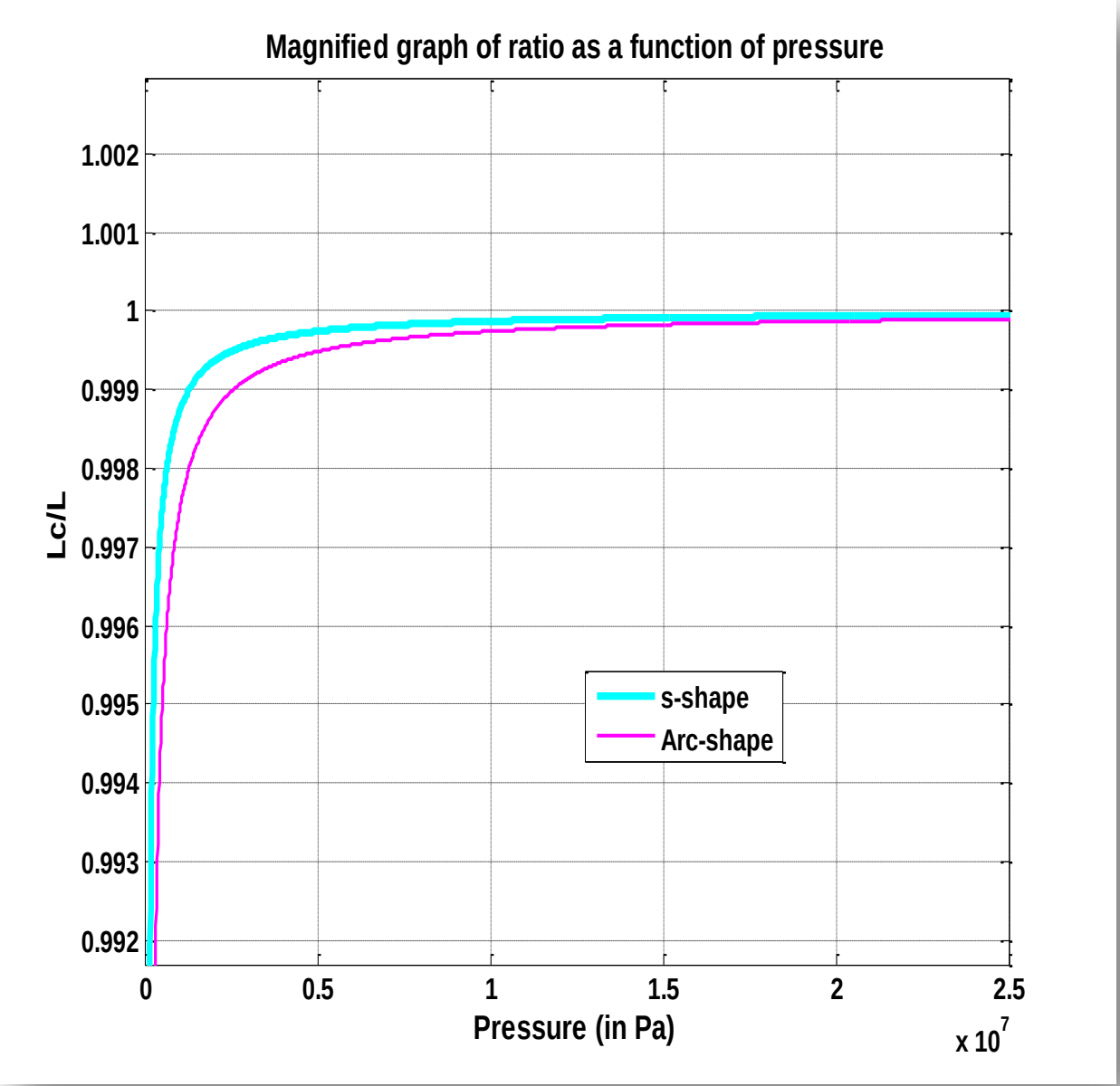

Figure 4.14: Plots of the variation of ratio Lc/L with pressure

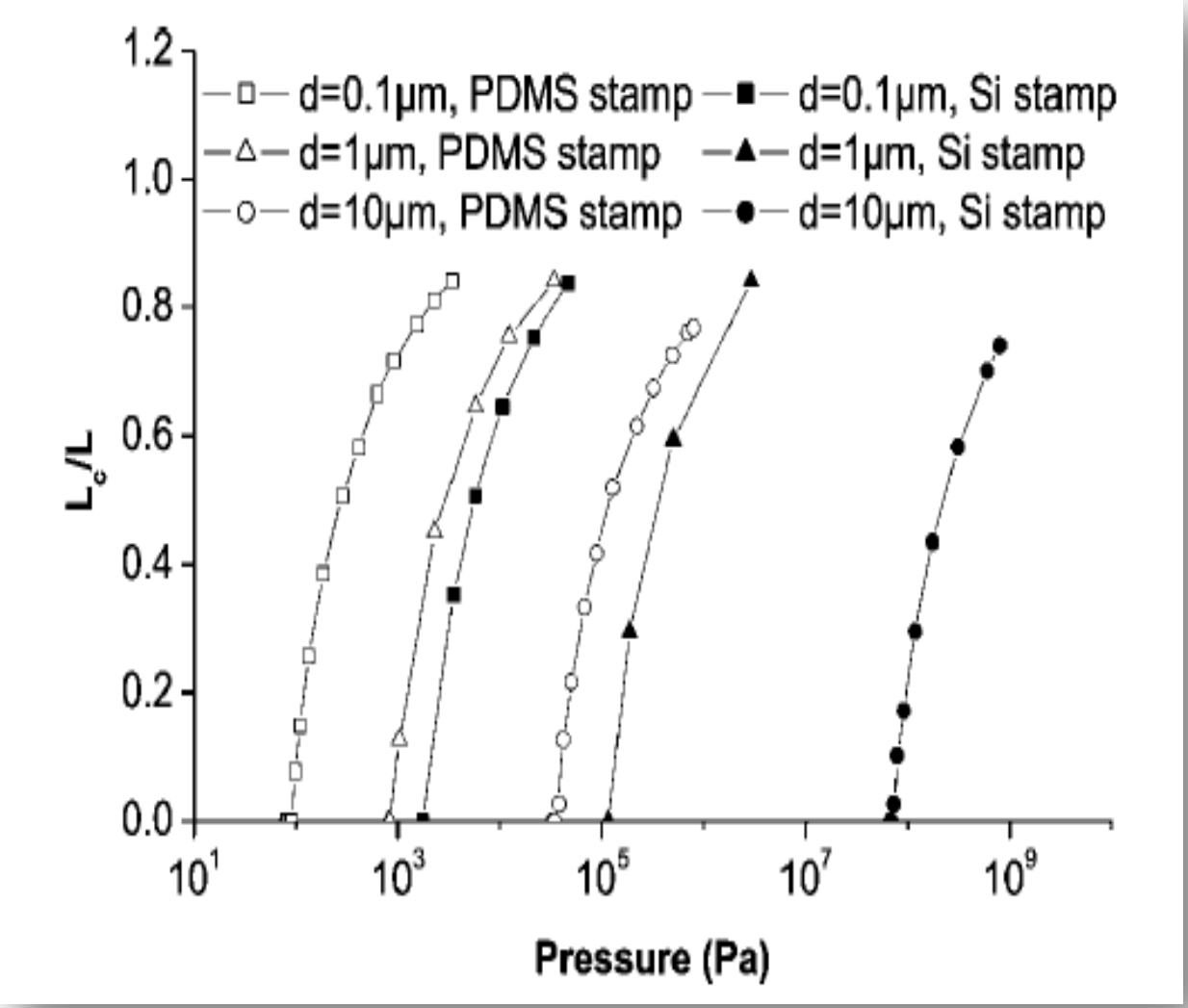

Figure 4.15: experimental results of ratio Lc/L with pressure

4.4. System Energies

This plot of energies is conducted to check that the constructed system responds well to elastic and surface energies behavior. This is shown on the graph below (Figure 4.16) obtained from literature in Mastrangelo, C. H. (1999) **[69]**.

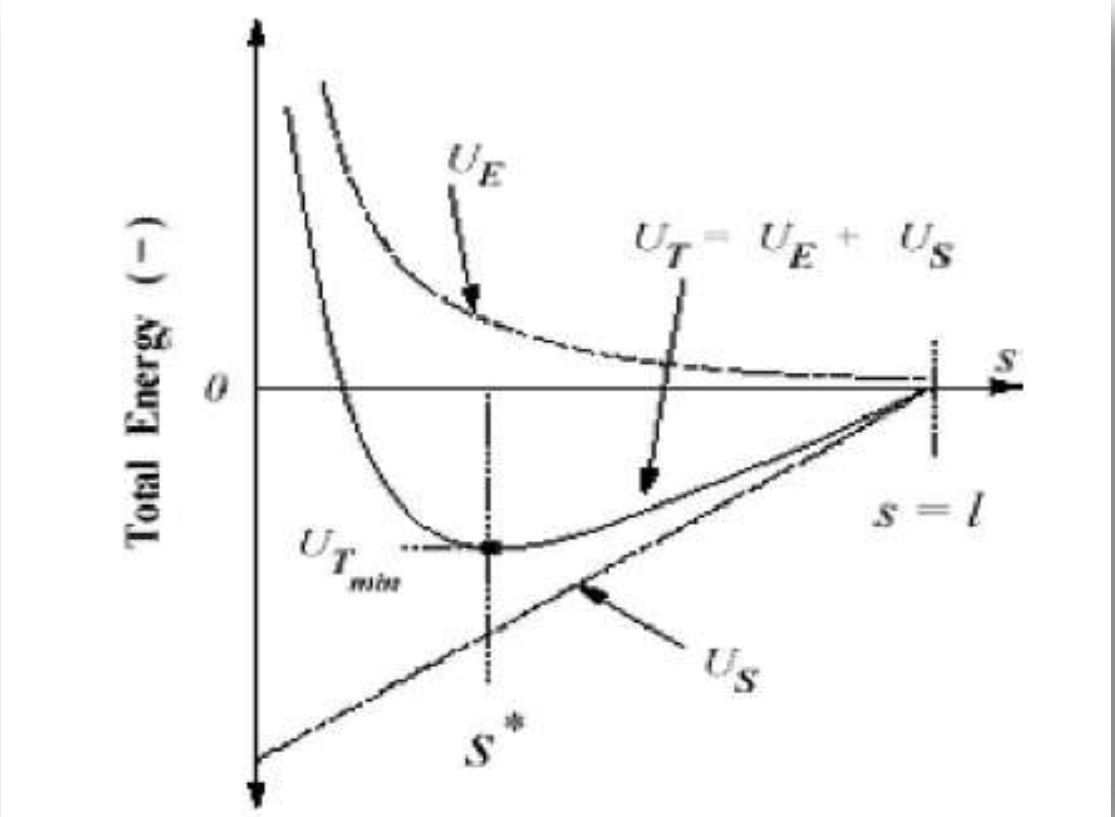

Figure 4.16: Plot of total, elastic and surface energies

But for our system the total energy is given by the sum of the various energies, such as elastic energy due to bending of the layer and the surface energy due to adhesion:

For the Arc-shape, we have $\boldsymbol{U_T(s) = \frac{3}{2}\frac{EI}{s^3}h_d^2 + \gamma b(L - s)}$

For the s-shape, we have $$U_T(s) = \frac{6EI}{s^3} h_d^2 + \gamma b(L - s)$$

And this gives us systems described by the graph below, which responded exactly as the pre-established system shown above.

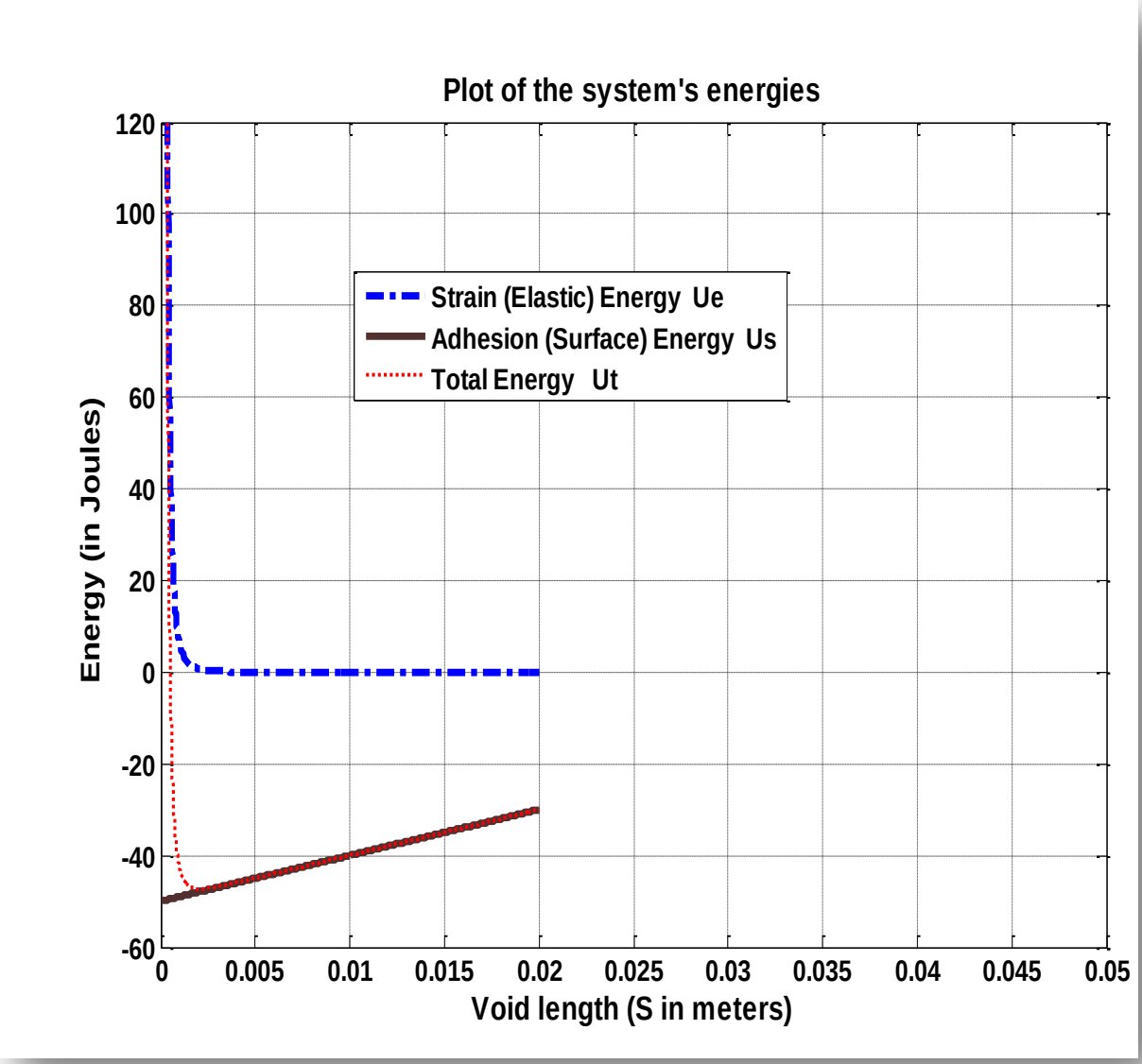

Figure 4.17: Plot of total, elastic and surface energies: result obtained through Matlab

Considering ΔU_e to be the difference in the energies of the two (2) systems, then we have: $\Delta U_e = \frac{6EI}{s^3} h_d^2 - \frac{3}{2}\frac{EI}{s^3} h_d^2 = \frac{9}{2}\frac{EI}{s^3} h_d^2 = Constant \times \frac{1}{s^3}$ which corresponds exactly to the elastic energy contribution of the system. This decreases as the void length decreases. This explains the hyperbolic shape of the curve.

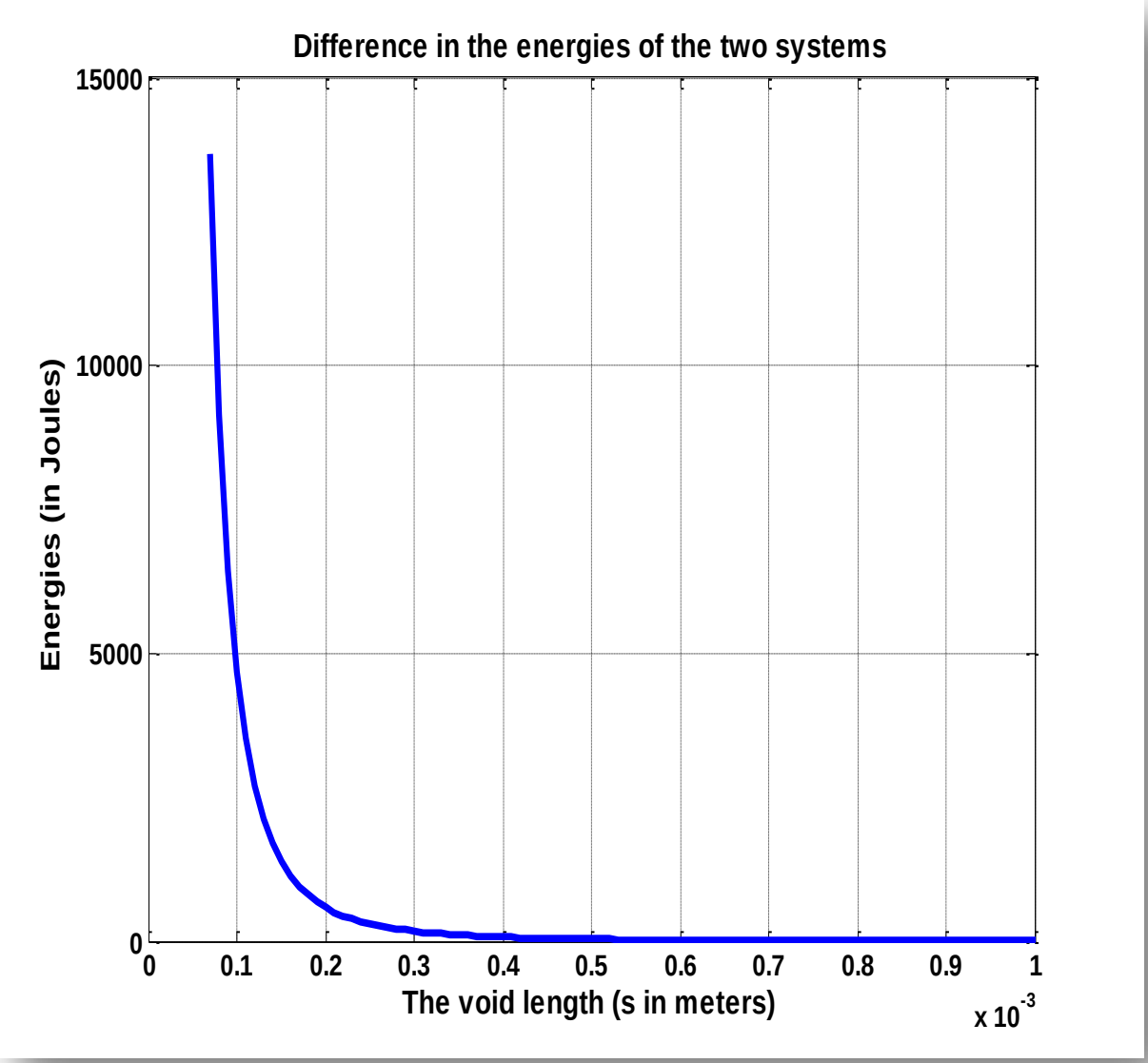

Figure 4.18: Plot of difference in total energies for the two shapes

4.5. Implications

The results obtained in the previous sections, particularly revealed in section 4.4, that the energy of the system actually responds to truly elastic and a surface adhesion behavior. This is well observed when compared to what was obtained as plot of energies by C. H. Mastrangelo (1999). And this establishes a solid ground for our discussion.

In section 4.2.1, that the void length, ***s***, for both systems (s-shape and arc-shape), decreases as the adhesion energy increases. Adhesion energies in the range of 0 to 50 Joules per meter squared have been chosen. This is in accordance with the experimental works carried on "Adhesion in organic electronic structures" by Tong et al. (2009) shown in Figure 4.19 below [76]:

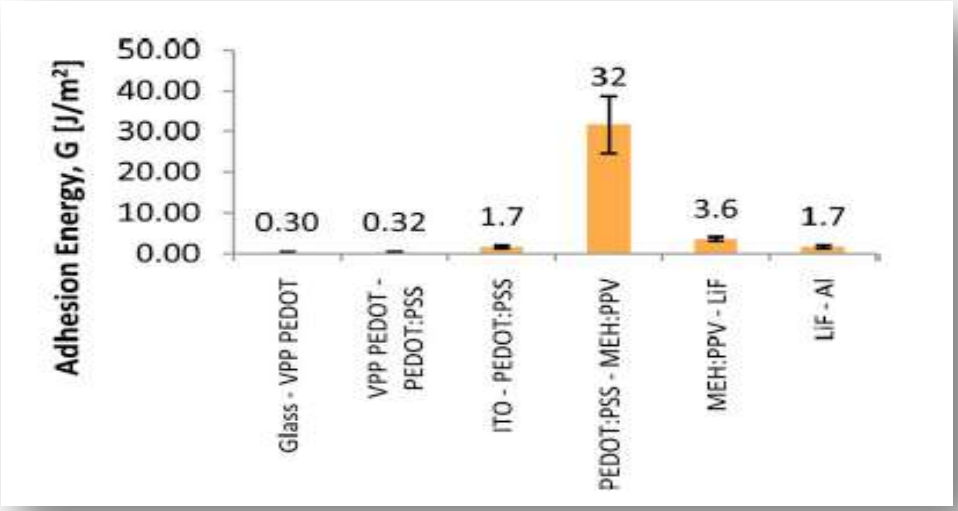

Figure 4.19: Comparison of adhesion energies

It revealed in general, that variation in the void length, ***s***, is different for different Young's modulus (***E***): ***s*** becomes bigger at higher modulus, ***E***.

Also the ratio of the contact length L_c to the length ***L***, namely L_c/L, increases as the adhesion energy, γ, increases. The void length, ***s***, increases as the modulus, ***E***, increases. The contact length, L_c, increases as the pressure, ***P***, due to lamination increases.

Based on these results it can be deduced that, if high moderate and appropriate adhesive forces are applied (so that the sink-in effect is avoided – sink-in could actually damage the cell) then high contact length, $\boldsymbol{L_c}$, could be achieved to enhance device efficiency and performance. This is confirmed by the fact that the ratio L_c/L increases as the adhesion energy increases.

If the void length, ***s***, enlarges with increasing modulus, ***E***; in other words if L_c decreases with increasing modulus, then this would suggest that materials with high modulus are not be advisable/recommended for organic photovoltaic structures, in particular BHJ solar cell layers. It can then be asserted that a material with a lesser modulus, ***E***, but same output should be preferable to a material with a higher modulus.

In the Figure 4.20 below, the TiO*x* layer functions as a scavenging layer to block the permeation of oxygen and moisture into the polymer active layer [77].

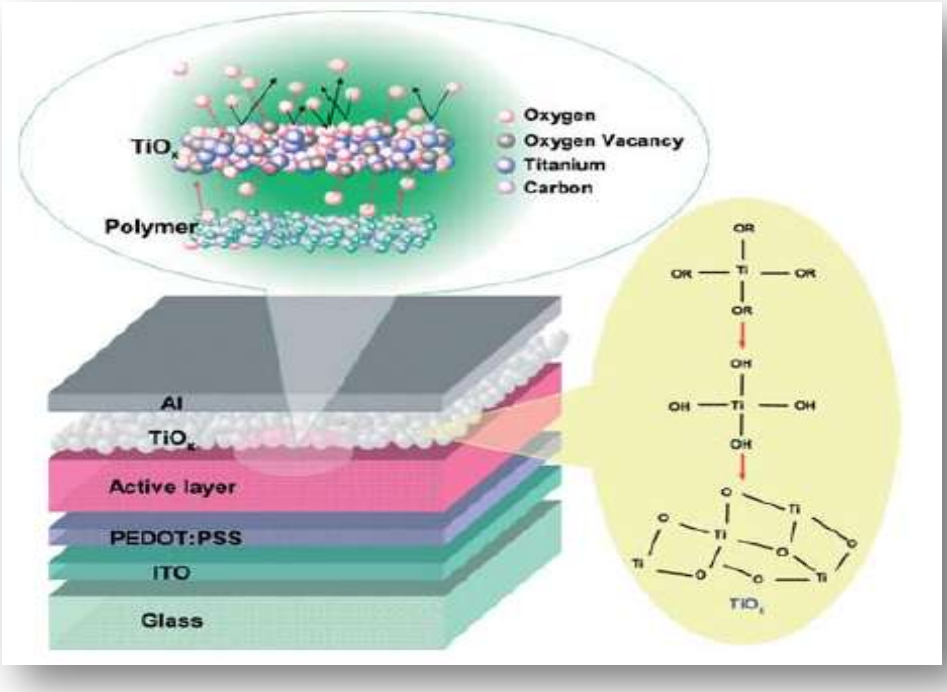

Figure 4.20: An OPV structure with the TiOx layer, as ITO/PEDOT:PSS/active layer/TiOx/Al [78]

But the results obtained in sections 4.2.1 and 4.2.3 showed that, not only would the controlled pressured lamination encapsulation protect the device against the effect of

moisture and oxygen and increase its life time but also it would promote better and longer contact length, L_c, to enhance device efficiency and performance.

4.6. Summary

In the previous sections we presented the results from our modeling of contact and adhesion in BHJ solar cells. We observed from the various graphs the effect of adhesion energy, the Young's modulus and the pressure due to lamination on the void lengths and the contact lengths of the two systems. These observations helped us think out of the box, to infer the possible implications on the device's lifetime, structure and efficiency. They also help us draw conclusions that are presented in the next chapter.

Chapter Five:

Conclusions and Suggestions for Future Work

5.1. Conclusions

i. Upon completing this research work it is found that the systems respond correctly to the energy balance equation known from literature. More adhesion at the interface reduces the void length (***s***), hence, contact length, $\boldsymbol{L_c}$, increases. A material with greater Young's modulus will promote longer void's length, ***s***, making it undesirable for BHJ solar cell applications.

ii. The controlled pressure assisted lamination method used for encapsulation would be of advantage to achieving adhesion and longer surface contact length, $\boldsymbol{L_c}$. It is to be noted that all these results and observations could be applied to most of organic electronic structures, especially Organic Light Emitting Diodes (OLEDs).

iii. In addition, all results obtained are in agreement with previously obtained experimental results. This reinforces the scientific understanding one is getting on the organic photovoltaic structures. This helps a lot in the quest of improving upon these structures.

5.2. Suggestions for Future Work

i. Within the time frame of this research, this is how far we have gone. Nevertheless, we expect to conduct a numerical simulation with finite elements based software to crosscheck our analytical modeling and experimental results obtained elsewhere

ii. But future research work in the domain, we would recommend that an experimental work should be done on ground, in this direction for a total assessment of all results obtained.

iii. Then the effect of these interesting results on charge transport and the current-voltage characteristics (Figure 5.1 below) can also be worked on. The final stage could be, to infer how these results could also affect the device efficiency.

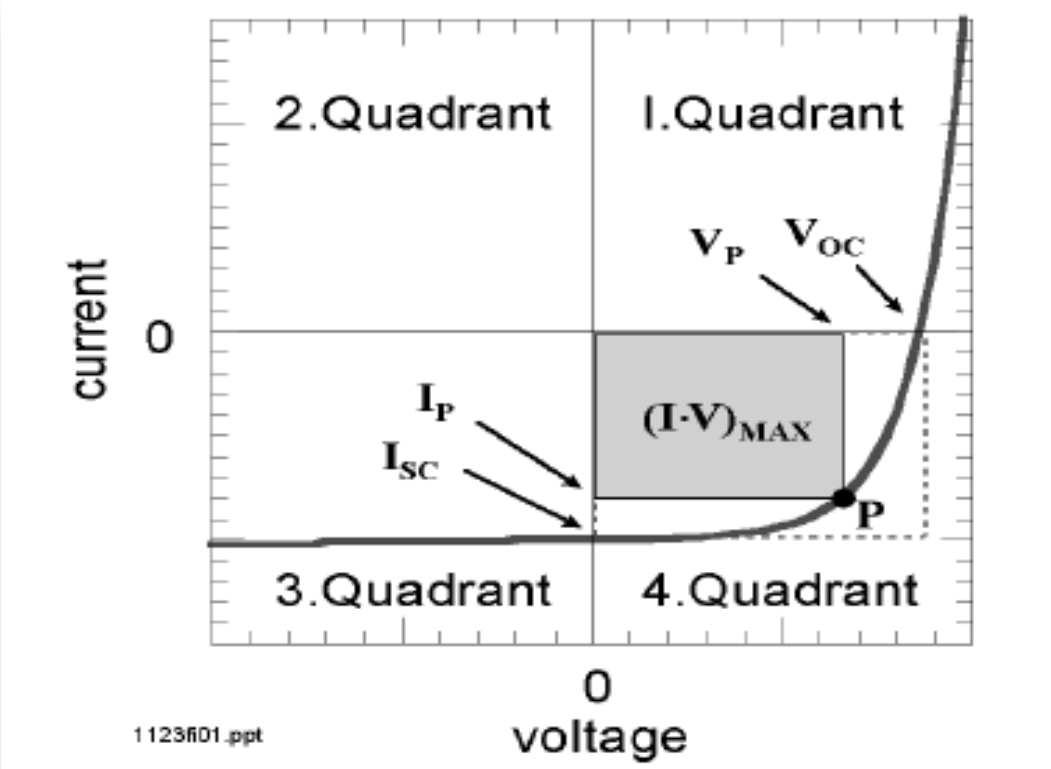

Figure 5.1: I-V characteristics of a PV solar showing all four quadrants [38]

➢ A1. Derivation of the maximum deflection of a cantilever beam

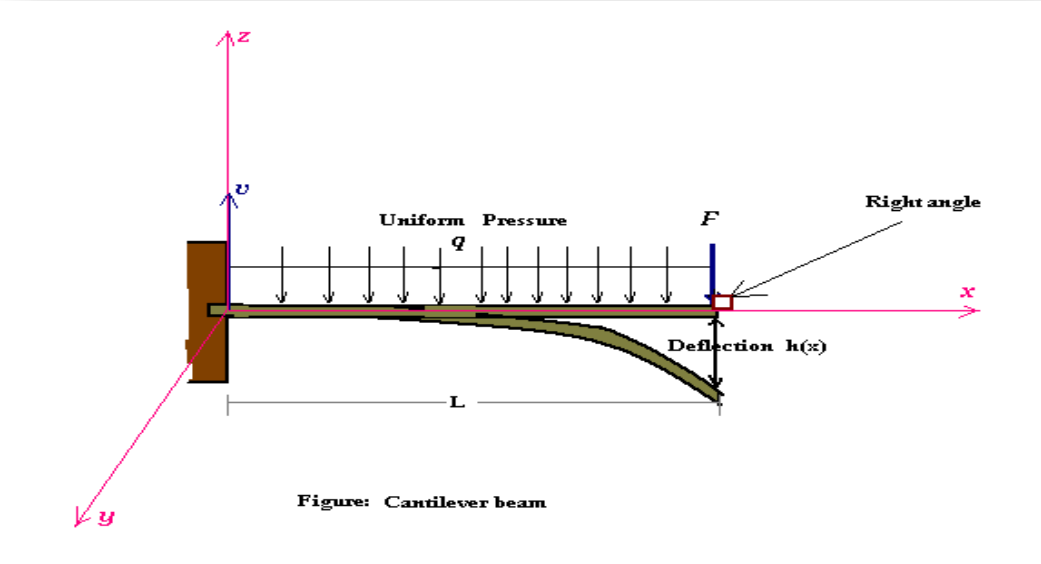

Figure A1: Undeformed and deformed cantilever beam under bending force F

L: Length of beam

h(x): Deflection

F: Applied force (or pressure)

v: Shear force

In moving through a ***virtual displacement h(x)***, the ***virtual work*** δW_{ext} done by the applied external forces is given by:

$$\delta W_{ext} = \int_0^L qh(x)dx + Fh(L) \quad [1]$$

The work done by the internal forces over a volume of contour ***R*** is as follows:

$$\delta W_{int} = \int \delta U dV \quad [2]$$

Taking ***dV=dAdx*** and substituting it into [2] we have:

$$\delta W_{int} = \int_0^L dx \int \delta\left(\frac{1}{2}\sigma_{ij}\varepsilon_{ij}\right) dA \quad [3]$$

Rearranging the equation [3.3] yields:

$$\delta W_{int} = \int_0^L dx \int (\sigma_{ij}\delta\varepsilon_{ij}) dA \quad [4]$$

From beam theory, the displacement field at a point through length of the beam is given by:

$$u = -z\frac{dh}{dx} \quad ; \quad v = 0 \quad ; \quad h = h(x) \quad [5]$$

Neglecting Poisson's effects, the strains are obtained as follows:

$$\varepsilon_{xx} = \frac{\partial u}{\partial x} = -z\frac{\partial^2 h}{\partial x^2} = -z\frac{d^2 h}{dx^2} \quad ; \quad \varepsilon_{yy} = 0 \quad ; \quad \varepsilon_{zz} = 0 \quad [6]$$

and the corresponding stresses are:

$$\sigma_{xx} = E\varepsilon_{xx} = E\frac{\partial u}{\partial x} = -Ez\frac{\partial^2 h}{\partial x^2} = -Ez\frac{d^2 h}{dx^2} \quad ; \quad \sigma_{yy} = 0 \quad ; \quad \sigma_{zz} = 0 \quad [7]$$

If also Shear strains and stresses are neglected, we then get the internal work to be:

$$\delta W_{int} = \int_0^L dx \int (\sigma_{xx}\delta\varepsilon_{xx}) dA \quad [8]$$

Substituting for $\sigma_{xx} = E\varepsilon_{xx}$ in the above equation we have:

$$\delta W_{int} = \int_0^L dx \int (E\varepsilon_{xx}\,\delta\varepsilon_{xx}) dA \quad [9]$$

Again substituting for the various values of the parameters in the above equation one would obtain:

$$\delta W_{int} = \int_0^L E\frac{d^2 h}{dx^2}\frac{d^2(\delta h)}{dx^2} dx \times \left(\int z^2 dA\right) \quad [10]$$

$$\delta W_{int} = \int_0^L EI\frac{d^2 h}{dx^2}\frac{d^2(\delta h)}{dx^2} dx \quad [11]$$

Therefore, from the principle of virtual work we have:

$$\delta W = \int_0^L \left(EI\frac{d^2 h}{dx^2}\frac{d^2(\delta h)}{dx^2} + q\delta h\right) + F\delta h(L) = 0 \quad [12]$$

Carrying step by step integration by parts we then get:

$$\int_0^L [\frac{d^2}{dx^2}\left(EI\frac{d^2h}{dx^2}\right) + q + F\delta(L-x)]\delta h dx + \left[\left(EI\frac{d^2h}{dx^2}\right)\delta\left(\frac{dh}{dx}\right) + \frac{d}{dx}\left(EI\frac{d^2h}{dx^2}\right)\delta h\right]_0^L = 0 \quad [13]$$

where $\delta(L-x)$ is the Dirac Delta function

$$\int_{-\infty}^{+\infty} \delta(L-x)f(x)dx = f(L) \quad [14]$$

The Euler equation for the beam is then obtained to be:

$$\frac{d^2}{dx^2}\left(EI\frac{d^2h}{dx^2}\right) + q + F\delta(L-x) = 0 \quad [15]$$

The boundary conditions are the following:

1. $EI\frac{d^2h}{dx^2}(L) = 0$
2. $\frac{d}{dx}\left(EI\frac{d^2h}{dx^2}\right)]_{x=L} = 0$ [16]

Applying the boundary conditions to the Euler equation for the beam above, we would therefore have:

$$\frac{d^2}{dx^2}\left(EI\frac{d^2h}{dx^2}\right) + F\delta(L-x) = 0 \quad [17]$$

Some important facts from this result stipulate that:

- h is the deflection (No derivative of h with respect to x)
- The first derivative of h with respect to x:

  $$\epsilon = \frac{dh}{dx} \quad [18]$$

  is the slope of the beam
- The negative of the product of the second derivative of h with respect to x and EI:

  $$M = -EI\frac{d^2h}{dx^2} \quad [19]$$

  is the ***bending moment*** with I being the ***second moment of area***

- The derivative of the bending moment ***M:***

$$\boldsymbol{v = \frac{d}{dx}M = -\frac{d}{dx}\left(EI\frac{d^2h}{dx^2}\right)} \quad \textbf{[20]}$$

is the ***Shear force*** in the beam

From literature, it can be recalled that the moment M of a force about any point is given by the cross product of the applied force and the displacement:

$$\boldsymbol{M = \vec{F} \times \vec{y}} \quad \textbf{[21]}$$

where in our case $\boldsymbol{\vec{y} = y\hat{\imath} = (L - x)\hat{\imath}}$ and $\boldsymbol{\vec{F} = F\hat{\jmath}}$

Making the appropriate substitutions we now get:

$$\boldsymbol{M = Fy \sin \emptyset} \quad \textbf{[22]}$$

where $\emptyset$ is the angle formed by the unit vectors $\boldsymbol{\hat{\imath}}$ **and** $\hat{\jmath}$.

From our figure it is observed that $\emptyset = 90^o$. Finally the moment is given by after substituting $\emptyset$,

$$\boldsymbol{M = F(L - x)} \quad \textbf{[23]}$$

Equating equations [3.] and [3.] we have:

$$\boldsymbol{M = -EI\frac{d^2h}{dx^2} = F(L - x)} \quad \textbf{[24]}$$

Rearranging the terms and dividing through – $\boldsymbol{EI}$ yields:

$$\boldsymbol{\frac{d^2h}{dx^2} = -\frac{F}{EI}(L - x)} \quad \textbf{[25]}$$

Integrating the ***LHS*** twice with respect to $\boldsymbol{x}$ yields ***h(x).***

Integrating the RHS once with respect to $\boldsymbol{x}$ yields:

$$\boldsymbol{-\frac{F}{EI}\left(Lx - \frac{1}{2}x^2\right) + K_1 = \frac{dh}{dx}} \quad \textbf{[26]}$$

But $\frac{dh}{dx} = 0$ at $x = 0$ i.e $K_1 = 0$; in other words

$$-\frac{F}{EI}\left(Lx - \frac{1}{2}x^2\right) = \frac{dh}{dx} \quad [27]$$

A second integration with respect to x gives:

$$-\frac{F}{EI}\left(\frac{1}{2}Lx^2 - \frac{1}{6}x^3\right) + K_2 = h \quad [28]$$

But **also** $h = 0$ at $x = 0$ i.e $K_2 = 0$; in other words

$$h(x) = -\frac{F}{EI}\left(\frac{1}{2}Lx^2 - \frac{1}{6}x^3\right) \quad [29]$$

At maximum deflection we have:

$$h_{max} = \left[-\frac{F}{EI}\left(\frac{1}{2}Lx^2 - \frac{1}{6}x^3\right)\right]_0^L$$

$$h_{max} = -\frac{F}{EI}\left(\frac{1}{2}L^3 - \frac{1}{6}L^3\right)$$

$$h_{max} = -\frac{F}{EI}\left(\frac{3L^3 - L^3}{6}\right) \quad [30]$$

Finally rearranging the terms, the maximum deflection is given by:

$$h_{max} = -\frac{FL^3}{3EI} \quad [31]$$

A2. Codes for Void's lengths and ratios

```
clear all
close all
%%%%%%%%%%%%%%%%%%%%%%%%%%%%%%%%%%%%%%%%%%%%%%%%%%%%%%%%%%%%%%%%%%%%%%%
%%% Void length for S-shape and Arc-shape %%%%% N. Y.DOUMON %%%%%%%%%%%
%%%%%%%%%%%%%%%%%%%%%%%%%%%%%%%%%%%%%%%%%%%%%%%%%%%%%%%%%%%%%%%%%%%%%%%

        E2=5.0*10^9;         % Young's modulus 2
        E1=2.5*10^9;         % Young's modulus 1
        t=1.00*10^-4;        % Thickness
        w=5*10^-2;           % Breadth
        I=(w*t^3)/12;        % Second moment of area
        h=1*10^-6;           % Void's height
        E=0.9*10^9;          % Young's modulus
        l=10^-1;             % Length
        b=((3/2)*E*t^3*h^2);       % Constant for s-shape
        b1=((3/2)*E1*t^3*h^2);     % Constant for s-shape 1
        b2=((3/2)*E2*t^3*h^2);     % Constant for s-shape 2
        b3=((3/8)*E*t^3*h^2);      % Constant for Arc-shape
        b4=((3/8)*E1*t^3*h^2);     % Constant for Arc-shape 1
        b5=((3/8)*E2*t^3*h^2);     % Constant for Arc-shape 1
        j=0:1:50;                  % Adhesion energy variation
        k=50;                      % Adhesion energy as a constant
        s=zeros(1,size(j,2));
        s1=zeros(1,size(j,2));
        s2=zeros(1,size(j,2));
        s3=zeros(1,size(j,2));
        s4=zeros(1,size(j,2));
        s5=zeros(1,size(j,2));
        for n=1:size(j,2);
          s(n)=[b*j(n)^-1]^(1/4);      % Void's length for s-shape
          s1(n)=[b1*j(n)^-1]^(1/4);    % Void's length for s-shape 1
          s2(n)=[b2*j(n)^-1]^(1/4);    % Void's length for s-shape 2
          s3(n)=[b3*j(n)^-1]^(1/4);    % Void's length for Arc-shape
          s4(n)=[b4*j(n)^-1]^(1/4);    % Void's length for Arc-shape 1
          s5(n)=[b5*j(n)^-1]^(1/4);    % Void's length for Arc-shape 2
        end
        lc=l-s;      % Contact length for s-shape
        lc1=l-s1;    % Contact length for s-shape 1
        lc2=l-s2;    % Contact length for s-shape 2
        lc3=l-s3;    % Contact length for Arc-shape
        lc4=l-s4;    % Contact length for Arc-shape 1
        lc5=l-s5;    % Contact length for Arc-shape 2
        z=lc/l;      % Ratio of lc/l  for s-shape
        z1=lc1/l;    % Ratio of lc/l  for s-shape 1
        z2=lc2/l;    % Ratio of lc/l  for s-shape 2
        z3=lc3/l;    % Ratio of lc/l  for Arc-shape
        z4=lc4/l;    % Ratio of lc/l  for Arc-shape 1
        z5=lc5/l;    % Ratio of lc/l  for Arc-shape 2
        d=s-s3;      % Difference in void's lengths
        plot(j,s,'b-'); hold on
        plot(j,s1,'r-'); hold on
```

```
%plot(j,s2,'b-'); hold on
%plot(j,s3,'m-'); hold on
%plot(j,s4,'m-'); hold on
%plot(j,s5,'m-'); hold on
%plot(j,z,'b-'); hold on
plot(j,z1,'b-'); hold on
plot(j,z2,'-'); hold on
%plot(j,z3,'m-'); hold on
%plot(j,z4,'m-'); hold on
%plot(j,z5,'m-'); hold on
plot(j,d,'r-'); hold on
```

➢ A3. Codes for energies

```
clear all; close all; clc
%%%%%%%%%%%%%%%%%%%%%%%%%%%%%%%%%%%%%%%%%%%%%%%%%%%%%%%%%%%%%%%%%%%%%%%%%%%%%%%
%%%%%%% Codes for the energies of the system %%%  N. Y. DOUMON %%%%%%%%
%%%%%%%%%%%%%%%%%%%%%%%%%%%%%%%%%%%%%%%%%%%%%%%%%%%%%%%%%%%%%%%%%%%%%%%%%%%%%%%
t=1.00*10^-3;    % Thickness of layer
b=1*10^-2;       % Breadth of layer
I=(b*t^3)/12;    % Second moment of area
h=1*10^-3;       % Height of the particle
k=100000;        % Adhesion energy
E=5.0*10^9;      % Young's modulus
l=5*10^-2;       % Length of solar cell's layer
s=7*10^-5:10^-5:2*10^-2;     % Void's length
u=zeros(1,size(s,2));
u1=zeros(1,size(s,2));
for n=1:size(s,2);
u(n)=(3/2)*E*I*h^2*s(n)^-3;     % Elastic energy for s-shape
u1(n)=(3/8)*E*I*h^2*s(n)^-3;    % Elastic energy for Arc-shape
end
lc=l-s;                         % Contact length
u3=-k*b*lc;                     % Surface energy for s-shape
U=u+u3;                         % Total energy for s-shape
w=u-u1;                         % Difference in energies
plot(s,u,'b-'); hold on
%plot(s,u3,'m-'); hold on
%plot(s,U,'r-'); hold on
plot(s,w,'b-')
```

➢ A4. Codes for Void's length versus modulus

```
clear all; close all
%%%%%%%%%%%%%%%%%%%%%%%%%%%%%%%%%%%%%%%%%%%%%%%%%%%%%%%%%%%%%%%%%%%%%%%%%%%%%%%%
%%%%%%%%%%%%%%% Codes for modulus variation %%%% N. Y. DOUMON %%%%%%%%%
%%%%%%%%%%%%%%%%%%%%%%%%%%%%%%%%%%%%%%%%%%%%%%%%%%%%%%%%%%%%%%%%%%%%%%%%%%%%%%%%
        t=1.00*10^-4;           % Thickness of layer
        h=1*10^-6;              % Height of the particle
        j= 50;                  % Adhesion energy
        l=5*10^-2;              % Length of solar cell's layer
        b=((3/2)*t^3*h^2);      % Constant for s-shape
        b1=((3/8)*t^3*h^2);     % Constant for Arc-shape
        e=0:1000:10^9;          % Young's modulus
        s=zeros(1,size(e,2));
        s1=zeros(1,size(e,2));
        for n=1:size(e,2);
            s(n)=[b*e(n)*j^-1]^(1/4);     % Void's length for s-shape
            s1(n)=[b1*e(n)*j^-1]^(1/4);   % Void's length for Arc-shape
        end
        lc=l-s;     % Contact length for s-shape
        lc1=l-s1;   % Contact length for s-shape
        z=lc/l;             %Length ratio for s-shape
        z1=lc1/l;           %Length ratio for Arc-shape
        %plot(e,s,'b-'); hold on
        %plot(e,s1,'r-'); hold on
        plot(e,z,'b-'); hold on
        plot(e,z1,'r-'); hold on
```

➢ A5. Codes for pressure

```
clear all; close all
%%%%%%%%%%%%%%%%%%%%%%%%%%%%%%%%%%%%%%%%%%%%%%%%%%%%%%%%%%%%%%%%%%%%%%%%%%%%%%%%
%%%%%%%%%%%%%%% Codes for the pressures %%%%% N. Y. DOUMON  %%%%%%%%%%
%%%%%%%%%%%%%%%%%%%%%%%%%%%%%%%%%%%%%%%%%%%%%%%%%%%%%%%%%%%%%%%%%%%%%%%%%%%%%%%%

        t=1.00*10^-1;         % Thickness of layer
        l=5*10^-1;            % Length of solar cell's layer
        E=2.5*10^9;           % Young's modulus
        b=[((1/24)*t^3*E)/l^2]^(1/2);     % Constant for s-shape
        b1=[((1/6)*t^3*E)/l^2]^(1/2);     % Constant for Arc-shape
        p=10^5:10000:10^8;                % Pressures
        s=zeros(1,size(p,2));
        s1=zeros(1,size(p,2));
        for n=1:size(p,2);
            s(n)=b*(1/p(n));            % Void's length for s-shape
            s1(n)=b1*(1/p(n));          % Void's length for Arc-shape
        end
        lc=l-s;                         % Contact length for s-shape
        lc1=l-s1;                       % Contact length for Arc-shape
        z=lc/l;                         % Lengths ratio for s-shape
        z1=lc1/l;                       % Lengths ratio for Arc-shape
        plot(p,s,'b-'); hold on
        plot(p,s1,'r-'); hold on
        %plot(p,z,'b-'); hold on
        %plot(p,z1,'r-'); hold on
```

References:

1. **Allen, R.** (2003), "The Penguin English Dictionary" – Penguin books

2. **Wilk, S. R.** (2009), " The yellow sun paradox" Optics and Photonics News 12-13

3. **Amuzu, J. K. A.** (1998), "First world, third world: A collection of essays on science, energy and the nuclear threat in the third world" - Ghana University Press, Accra –

4. **Country energy information: Togo** (2006), "Sixth framework programme priority 3" - Underpinning the economic potential and cohesion of a larger and more integrated - www.energyrecipes.org -

5. **FAO-IAEA-DESA-UNEP-UNIDO** (2006), "UN-Energy demonstration study- Assessing policy option for increasing the use of renewable energy for sustainable development: Modelling energy scenarios for Ghana" - CSD-14 UN-Headquarters, NY, USA

6. **VRA & ECG** (2007), "Special press briefing on the electrical energy situation in Ghana" - Joint statement by the Chief Executive of VRA and Managing Director of ECG at the ministry of information - Conference Hall, Accra – www.energyrecipes.org

7. **Beuve-Méry, H. & Izraelewicz E**. (2011), " Le Monde: Le nucléaire hors contrôle au Japon : A la centrale de Fukushima Daiichi, six reacteurs en crise aigue" – 67^{e} année – N^{o} 20573 – www.lemonde.fr

8. **Okoye, J. K.** (2007), "Background study on water and energy issues in Nigeria to inform the national consultative conference on dams and development"

9. **Sørensen, B.** (2004), "Renewable energy: Its physics, engineering, use, environmental impacts, economy and planning aspects" – Elsevier Science – Ch. 4

10. **Markvart, T. et al** (1994), "Solar electricity" - John Wiley & Sons -

11. www.solarbuzz.com/Technologies.htm

12. **Dennler, G. et al** (2005), "Flexible, conjugated polymer-fullerene-based bulk-heterojunction solar cells: Basics, encapsulation, and integration" - J. Mater. Res., Vol. 20, No. 12

13. **Green, M. A. et al** (2009), "Programme on photovoltaic" - Res. Appl. 17 p85

14. **Koster, C. J. A. et al** (2006), Appl. Phys. Lett. 88, 2006, 693511

15. **Aldous, S.** (2005), "How Solar Cells Work" How Stuff Works http://science.howstuffworks.com/solar-cell1.htm

16. **Preuss, P.** (2002), "An unexpected discovery could yield a full spectrum solar cell" Research News – Berkeley Lab. http://www.lbl.gov/Science-Articles/Archive/MSD-full-spectrum-solar-cell.html

17. **Sanders, B.** (2002), "Cheap, Plastic Solar Cells May Be On The Horizon" UC Berkeley Campus News - http://www.berkeley.edu/news/media/releases/2002/03/28_solar.html

18. **National Science Foundation** (2001), "Societal Implications of Nanoscience and Nanotechnology" - http://www.wtec.org/loyoa/nano/societalimpact/nanosi.pdf

19. **Engineer Magazine** (2005), "Power Plastic" http://www.konarkatech.com/news_and_events/konarka_articles/2005/3_march/the_engineer/power_plastics_mar8.php

20. **Choi, C.** (2004), "Nanotech Improving Energy Options" Space Daily New York: http://www.spacedaily.com/news/nanotech-04zj.html

21. **Senturia, S. D. & Wedlock, B. D.** (1975), "Electronic Circuits and Applications" – John Wiley & Sons – Pp 169 – 172 Ch. 6

22. **Chapple, M.** (2003), "Schaum's A – Z Physics" – McGraw Hill – Pp 218-219

23. **Poole, C. P. J. & Owens, F. J.** (2003), "Introduction to Nanotechnology" – John Wiley & Sons Inc. Publication – ch. 5 Pp20 -22 ; 125-132

24. **Fonash, S. J.** (2010), " Solar cell device physics" Pp 67-75

25. **Markvart, T. & Castafier, L.** (2006), "Solar Cells- Materials, Manufacture and Operation"- Elsevier Ltd.-

26. **Wager, J. F. et al.** (2008), "Transparent electronics" - Springer – Pp 91-111

27. **Sze, S. M. & Ng, K. K.** (2007), "Physics of semiconductor devices" - 3rd edition, Wiley, New York

28. **Kröger, F. A.** (1974), "The chemistry of imperfect crystals" - 2nd edition, North-Holland, Amsterdam

29. **Kuo Y** (2004), "Thin film transistors"- Volume 2: polycrystalline silicon Kluwer, Boston

30. **Persson, C. & Zunger A.** (2003), "Anomalous grain boundary physics in polycrystalline CuInSe2: the existence of a hole barrier" - Phys Rev Lett 91:266401/1-266401/4

31. **Wager, J. F.** (2007), "Transparent electronics: Schottky barrier and heterojunction considerations" - Thin Solid Films - Elsevier

32. **Yu, G. & Heeger, A. J.** (1995), "Charge Separation and Photovoltaic Conversion in Polymer Composites with Internal Donor-Acceptor Heterojunctions" - Appl. Phys. Vol. 78(7) - Pp 4510-4515

33. **Yu, G. et al.** (1995), "Polymer Photovoltaic Cells - Enhanced Efficiencies Via a Network of Internal Donor-Acceptor Heterojunctions" - Science, Vol. 270(5243) - Pp 1789-1791

34. **Salafsky, J. S.** (1999), "Exciton dissociation, charge transport, and recombination in ultrathin, conjugated polymer-TiO2 nanocrystal intermixed composites" – Physical Review B, Vol. 59(16) - Pp 10885-10894

35. **Petritsch, K. et al.** (2000), "Dye-based donor/acceptor solar cells" - Solar Energy Materials and Solar Cells, Vol. 61 (1) - Pp 63-72

36. **Hagfeldt, A. & Gratzel, M.** (2000), "Molecular photovoltaics" - Accounts of Chemical Research, Vol. 33 (5) - Pp 269-2 77

37. **Luque, A. & Hegedus S.** (2003), "Handbook of photovoltaic science and engineering"– Ch. 3 – Physics of solar cell – John Wiley & Sons

38. **Klaus, P.** (2000), "Organic Solar Cell Architectures" – Doctoral Dissertation - Technisch-Naturwissenschaftliche Fakult¨at der Technischen Universit¨at Graz (Austria)

39. **Lewerenz, H. J. and Jungblut, H.** (1995), "Photovoltaic - Grundlagen und Anwendungen" Springer, Berlin, Heidelberg, New York

40. **Green, M. A.** (1995), "Silicon Solar Cells: Advanced Principles and Practice"- University of New South Wales, Sydney

41. **Britney Spears**' guide to semiconductor physics http://britneyspears.ac/lasers.htm

42. **Sze, S. M.** (2001), "Semiconductor devices, Physics and Technology" – John Wiley & Sons – New York – 2nd Edition

43. **Van Roosbroeck, W.** (1950), Bell Syst. Tech. J. 29, Pp 560-607.

44. **Lundstrom, M. & Schulke, R**. (1983), IEEE Trans. Electron Devices 30, Pp 1151-1159.

45. **Yatap-dong, Bundang-gu, Seongnam-si, Gyeonggi-do** (2010), "Next-Generation Organic Solar Cell Technology and Market Forecast" - Korea 463-828 – Display bank Co., Ltd.

46. **Mordel, D. L. Et al**. (1978), Applied Physics Letters 32, Pp 495-497

47. **Gosh, A. K. & Feng T.** (1978), Journal of Applied Physics 49, Pp 5982-5989

48. **Sze, S. M.** (1981), "Physics of semiconductor devices" – John Wiley & Sons – New York

49. **Perepichka, D.** (2010), "Lectures on Organic Materials for Solar Cells" - Department of Chemistry McGill University

50. **Tang, C. W.** (1986), Applied Physics Letters 48, Pp 183-185

51. **Yu, G. et al** (1995), "Polymer PV cells: Enhanced efficiencies via a network of internal donor-acceptor heterojunctions" – Science, 270, 1789

52. **Li, G. et al.** (2005), "High-efficiency solution processable polymer PV cells by self-organization of polymer blends" – Nature Materials 4, Pp 864-868

53. **Kim, Y. et al.** (2006), "A strong regioregularity effect in self-organizing conjugated polymer films and high-efficiency polythiophene: Fullerene solar cells" - Nature Materials 5, Pp 197-203

54. **Wong, W. S et al.** (2009), "Flexible electronics: Materials & Applications" – Springer Science – Business Media – Ch. 12

55. **Hakola, E. & Kopola, P.** (2010), "Manufacturing and production equipment and systems for polymer and printed electronics" – Research Report (PRODI WP1 Organic solar cell (OSC) manufacturing requirements) - VTT-PRODI-WP1-D1.2

56. **Lungenschmied, C. et al.** (2007), "Flexible long-live, large area, organic solar cells" – 91, Pp 379-384

57. **Tuomikoski, M. et al.** (2006), "Manufacturing of polymer light-emitting device structures" - Proceedings SPIE. Vol. 6192 Organic Optoelectronics and Photonics II. SPIE, 9

58. **Zimmermann, B.** (2008), "Inversion of the layer sequence in organic solar cells - physical and technological aspects" - Doctoral Dissertation, Fraunhofer-Institut, Freiburg, Germany. 202

59. **Dow Corning Corp.** (1979), "Develop Silicone Encapsulation Systems for Terrestrial Silicon Solar Arrays" DOE/JPL/954995-80/6.

60. **Green, M. A.** (2005), " Silicon photovoltaic modules: A brief history of the first 50 years"- Progress in Photovoltaics - Vol. 13, Pp 447-455

61. **Nunzi, J. M.** (2002), "Organic Materials and Devices for Photovoltaic Applications" - ERT Cellules Solaires Photovoltaïques Plastiques- Labo POMA, Angers, France - Pp 197-224

62. **Jain, A. & Kapoor, A.** (2005), "A New Approach to Study Organic Solar Cell Using Lambert W-Function" - Solar Energy Materials & Solar Cells- Vol. 86 - Pp 197-205

63. **Charles, J. P.** (1984), "Caractérisation I-V et Fonctionnement des Photopiles Solaires" - Thèse de Doctorat ès Sciences- Université des Sciences et Techniques du Languedoc

64. **Brabec, C. J. et al.** (2005), "Theme Article – Production Aspects of Organic Photovoltaics and Their Impact on the Commercialization of Devices" - Mrs Bull., Vol. 30 - p 50.

65. **Charles, J. P. et al** (2000), "La Jonction, du Solaire à la Microélectronique" - Rev. Energ. Ren., Vol. 3 - Pp 1-16.

66. **Zong, Z. et al.** (2006), "Nano- and microscale adhesion energy measurement for Au–Au contacts in microswitch structures"- Journal Of Applied Physics 100, 104313

67. **Mastrangelo, C. H. & Hsu, C. H.** (1993), J. Microelectromech. Syst. 2, 33

68. **Mastrangelo, C. H. & Hsu, C. H.** (1993), J. Microelectromech. Syst. 2, 44

69. **Mastrangelo, C. H.** (1999), MRS Meeting, Boston, MA-unpublished-

70. Maugis, D. (1992), J. Colloid Interface Sci. 150, 243

71. Johnson, K. L. et al. (1971), Proc. R. Soc. London, Ser.A 324, 301

72. Grierson, D. S. et al. (2005), "Accounting for the JKR–DMT transition in adhesion and friction measurements with atomic force microscopy"- J. Adhesion Sci. Technol., Vol. 19, No. 3–5 - Pp 291-311

73. Ahmadi, G. (2003), "Particle Adhesion and Detachment Models" -Clarkson University- www.clarkson.edu/projects/crcd/me537/downloads/slides/6_JKR.pdf

74. Pietrement, O. & Troyon, M. (2000), J. Colloid Interface Sci. 226, 166

75. Cao, Y. et al. (2005), "Effects of dust particles and layer properties on organic electronic devices fabricated by stamping" - Journal Of Applied Physics 98, 033713

76. Tong, T. et al. (2009), "Adhesion in organic electronic structures" - Journal Of Applied Physics 106, 083708

77. Li-Min, C. et al. (2010), "Interface investigation and engineering – achieving high performance polymer photovoltaic devices" – Journal Of Materials Chemistry - 20, Pp 2575-2598

78. Lee K. H. et al. (2007), Adv. Mater., 19, 2445.